BIOMIMETIC GELMA-BASED HYDROGELS FOR 3D NEURAL TISSUE ENGINEERING

MEI QUANJING

PhD

The Hong Kong Polytechnic University

2023

The Hong Kong Polytechnic University
Department of Biomedical Engineering

Biomimetic GelMA-based Hydrogels for 3D Neural Tissue Engineering

MEI Quanjing

A thesis submitted in partial fulfilment of the requirements for the degree of Doctor of Philosophy

March 2023

Certificate of Originality

I hereby declare that this thesis is my own work and that, to the best of my knowledge and belief, it reproduces no material previously published or written, nor material that has been accepted for the award of any other degree or diploma, except where due acknowledgement has been made in the text.

_____(Signed)

MEI Quanjing (Name of student)

Abstract

The nervous system is a complex, multi-layered tissue system. The lack of access to live human brain tissue and the inherent limitations of animal research make it difficult to study the functions of the nervous system and the diseases affecting it. It is possible to construct neural tissue mimics (NTMs) *in vitro*. However, these experiments are typically conducted on two-dimensional (2D) substrates and cannot accurately represent the three-dimensional (3D) microstructure of neural tissues. To address this issue, biomimetic gelatin-methacryloyl (GelMA) hydrogels with highly desired biological and physical characteristics similar to the extracellular matrix (ECM) in nature have been developed to investigate neural development, neurogenesis, and electrophysiology in a 3D environment.

In the first part of this study, by varying the polymer compositions of GelMA and long-chain polyethylene glycol diacrylate (PEGDA), biomimetic hydrogels with tensile and compressive moduli of approximately 10 and 0.8 kPa, respectively, were created to simulate the mechanical environment of neural tissues. *In vitro* findings indicated that the GelMA-PEGDA hydrogels were biocompatible to sustain stem cell growth, proliferation, differentiation, and neurite extension. Also, stretching significantly increased neurite extension, axon elongation, and directionally oriented neurites along the direction of stretching. In addition, immunofluorescence staining, and relative gene expression revealed that stretching could facilitate the upregulation of neuronal differentiation-related proteins and genes, such as glial fibrillary acidic protein (GFAP)

and neuron-specific class III beta-tubulin (Tuj-1). In conclusion, the unique mechanical properties of GelMA-PEGDA could not only promote neuronal differentiation toward a particular lineage, but stretching is an intriguing strategy for boosting the efficiency of neural stem cell (NSC) therapies.

In the second part of the study, poly (3,4-ethylenedioxythiophene) polystyrene sulfonate (PEDOT:PSS) was incorporated as an additive improving the conductive properties of GelMA-PEGDA hydrogels. In contrast to non-conductive hydrogel, the conductive hydrogel itself could promote neuronal development. With electrical stimulation (ES), the conductive hydrogel could further induce stem cell differentiation with increased neuronal extension and relative gene expression. Meanwhile, stretching could also induce neuronal differentiation and directional alignment of axon extension, consistent with the previous part. The co-stimulation of mechanical stretching and electrical stimulation had synergetic effects on neuronal development, namely promoted neurite outgrowth, increased filopodia density and neurite branching, upregulated relative expression of neuronal differentiation genes, and higher electrical activity of encapsulated neuronal cells. This study enriched the knowledge about the directed differentiation of NSC within 3D microenvironment through physical cues, offering theoretical basis for the effectiveness and feasibility of NSC therapy.

To further fabricate 3D NTMs with customisable sizes, forms, and functionalities, in this chapter, a novel host-guest hydrogel bio-ink based on GelMA and hyaluronic acid

was developed for bioprinting. The rheological results indicated that host-guest hydrogel had excellent shear-thinning and fast self-healing properties, which endowed hydrogels with outstanding printability to be produced and maintained in diverse structures. Meanwhile, the host-guest interaction could protect cells from high shear force during printing, and cells maintained high viability and proliferation after printing. In addition to mimicking the neural structure, host-guest interaction mimicked the dynamic ECM environment that regulated cell behaviours (cell morphology, spreading, and migration) and function of the neural system (electroactivity and signal transmission), forming a united neural network. With good cell viability and electroactivity, we believe that the NTMs developed using host-guest hydrogels hold great promise in replicating the structure and function of different neural tissues, allowing researchers to investigate the underlying mechanisms of neural communication and information processing, as well as the mechanisms of nerve damage and repair to develop potential treatments for neural regeneration.

Overall, a range of biomimetic GelMA hydrogels were developed for studying neural development, neurogenesis, and electrophysiology. These hydrogels had high biocompatibility for neural cell encapsulation and provided a 3D matrix, which would be more effective in recapitulating neural tissues compared to 2D counterparts. We then fabricated NTMs through bioprinting to mimic the intricate structure of the nervous system. The 3D-printed NTMs had controlled structure and high electrophysiological activity to form interconnected 3D neural networks. Overall, these studies help achieve

the following: (1) enrich the existing literature on the directed differentiation of NSC in a 3D microenvironment induced by physical stimuli; (2) offer a foundation for the efficacy and practicability of NSC treatment; (3) improve translational applicability and present a better model for studying neural regeneration.

List of Publications

Journal Papers

1. **Mei QJ,** Yuen HY, Zhao X. Mechanical stretching of 3D hydrogels for neural stem cell differentiation. Bio-Design and Manufacturing, 2022, 5(4): 714-728.
2. **Mei QJ,** Rao JD, Bei HP., Liu YX, Zhao X. 3D bioprinting photo-crosslinkable hydrogels for bone and cartilage repair. International Journal of Bioprinting, 2021, 7(3).
3. Zhuang QN, Yao KM, Wu MG, Lei ZG, Chen F, Li JY, **Mei QJ**, Zhou YY, Huang QY, Zhao X, Li Y, Yu XG, Zheng ZJ. Wafer-patterned, permeable, and stretchable liquid metal microelectrodes for implantable bioelectronics with chronic biocompatibility, Science Advances, 2023, 9(22): eadg8602.
4. Chen F, Zhuang QN, Ding YC, Zhang C, Song X, Chen ZJ, Zhang YK, **Mei QJ**, Zhao X, Huang QY, Zheng ZJ. Wet-Adaptive Electronic Skin, Advanced Materials, 2305630.
5. **Mei QJ,** Chen TY, Zhao X. The electro-mechanical stimulus on neural differentiation. (In preparation)
6. **Mei QJ,** Mo YY, Bei HP, Zhang HY, Sun YL, Zhao X. Host-guest based self-healing hydrogel for 3D bioprinting neuron mimics. (In preparation)

Acknowledgements

Firstly, I would like to express my sincere thanks to my supervisor, Dr Xin Zhao, for her constant guidance, encouragement, and support during my whole PhD study. Under her careful guidance, I understood how to discover problems and conduct research scientifically. She also taught me how to think deeply and critically. More importantly, her enthusiasm for research, positive attitude toward life, and calmness in facing difficulties have influenced me deeply. I believe these lessons would benefit me throughout my life.

I would like to thank Dr Hongyu Zhang from Tsinghua University. I have studied some synthetic experiments in his laboratory, and I am very grateful for his help and guidance. His rigorous and realistic scientific research attitude also affected my scientific research deeply.

Besides, I would like to thank all the collaborators and friends, including Dr Yuhe Yang, Dr Qiang Zhang, Dr Yu Tian, Dr Aun Raza, Miss Jingdong Rao, Miss Di Suo, Miss Mengna Zhao, Mr Tianpeng Xu, Mr Shang lv, Mr Huaqian Liu, Mr Yuen Andy, Mr Ho Pan Bei, Mr Chun Hei Lam, Mr Bo Liang, Miss Xiaoxiao Xu, Miss Tianyu Chen, Mr Shuai Zhao. All of them helped me a lot during my PhD research and gave me constructive suggestions and valuable assistance to make things better. It is my great honour to work in such a team. At the same time, I also would like to thank Dr Yulong Sun, Dr Weiwei ZHAO, Dr Mingrui He, Miss Yiwei Zheng, and Miss Ying Han from

Dr Hongyu Zhang's Lab for their kind help and suggestions to my host-guest hydrogel project.

I would like to express my thanks to Ms Dawn Li and Ms Jenny Chau in the General office of the Department of Biomedical Engineering for their kind help.

Lastly and most importantly, I would like to express my gratitude to my family for their unconditional love, unlimited support, and encouragement throughout my life.

Table of Contents

List of Abbreviations

Ad	Adamantane
Ad-gelatin	Amantadine modified gelatin
Ad-GelMA	Amantadine-modified GelMA
ASC	Adipose stromal cells
BDNF	Brain-derived neurotrophic factor
bFGF	Basic fibroblast growth factor
BrdU	Bromodeoxyuridine
BSA	Bovine serum albumin
CD	β-cyclodextrin
CDC	Charge delivery capacity
CDHA	HA modified with β-cyclodextrin
CDMeHA	HA modified with both methacrylate and β-cyclodextrin moieties
CNS	Central nervous system
CNTs	Carbon nanotubes
CREB	Cyclic adenosine response element-binding protein
CSPGs	Chondroitin sulfate proteoglycans
CV	Cyclic voltammetry
DMEM	Dulbecco's Modified Eagle Medium
DS	Degree of substitution
ECM	Extracellular matrix
EDC	1-(3-Dimethylaminopropyl)-3-ethylcarbodiimide hydrochloride

EDS	X-ray spectroscopy
EIS	Electrochemical impedance spectroscopy
EMFs	Electromagnetic fields
EPSP	Excitatory postsynaptic potential
ES	Electrical stimulation
ESCs	Embryonic stem cells
FBS	Fetal bovine serum
FGFs	Fibroblast growth factors
FTIR	Fourier transform infrared
GelMA	Gelatin-methacryloyl
HA	Hyaluronic acid
HBSS	Hanks' Balanced Salt Solution
hMSCs	Human MSCs
iPSCs	Induced pluripotent stem cells
KCl	Potassium chloride
MA	Methacrylate anhydride
MAC	Methacrylamide chitosan
MEA	Microelectrode array
MeHA	Methacrylated HA
MSCs	Mesenchymal stem cells
N2a	Neuro2a
NaCl	Sodium chloride
NGF	Nerve growth factor

NHS	N-Hydroxysuccinimide
NSC	Neural stem cell
NSPCs	Neural stem/progenitor cells
NTM	Neural tissue mimics
PANi	Polyaniline
PBS	phosphate buffer solution
PCL	Poly(caprolactone)
PDMS	Polydimethylsiloxane
PEDOT: PSS	Poly(3,4-ethylenedioxythiophene) polystyrene sulfonate
PEG	Poly (ethylene glycol)
PEGDA	Polyethylene glycol diacrylate
pHEMA	Poly (2-hydroxyethyl methacrylate)
PNNs	Generating perineuronal nets
PNS	peripheral nervous system
PPy	Polypyrrole
RA	Retinoic acid
RGD	Arginine-glycine-aspartic acid
RT-qPCR	Reverse transcription quantitative polymerase chain reaction
SEM	Scanning electron microscopy
VEGFs	Vascular endothelial growth factors

Chapter 1 Introduction

1.1 The neural cell microenvironment

Cells are situated in a cell microenvironment, a complex, diverse, and continuously changing collection of biochemical and biophysical stimuli that regulate cell behaviour [1]. Consequently, the microenvironment plays a significant role in highly specialised nervous system structures. Although the microenvironments of cells are varied considerably, the cellular microenvironments of animals have a lot common features in terms of compositions and functions [2]. The cellular microenvironment encompasses a heterogeneous milieu of cellular constituents, bioactive soluble factors, ECM components, and biophysical stimuli; these determine cell behaviours and activities, including proliferation, migration, self-renewal, differentiation, and death [3].

1.1.1 Cells of the nervous system

Multiple cell types are responsible for the proper functions of the nervous system. Typically, neurons have dendrites or specialised nerve terminals, which transmit electrical impulses to the cell body via axons (nerve fibres). Glial cells perform a range of tasks, including blood-brain barrier development and axon protection. Neural stem cell (NSC), which are mostly undifferentiated, can generate offspring cells that grow and develop into neurons and glial cells. Cells communicate with a diverse of cell types, both similar and dissimilar to their own [4].

1.1.1.1 Neurons

Neurons epitomize a heterogeneous cohort of extensively specialized cells that comprise the intricate framework of the nervous system, orchestrating a myriad of neurophysiological functions. **Schematic 1.1** depicts the normal structure of a neuron, which includes the cell body, axon, and dendrites [5]. Neurons have the ability to sense stimuli, integrate information and convey nerve impulses and thus carry out the functions of the neurological system. Generally, neurons receive signals through dendrites and emit signals along their axons. The signal then travels from the axon of one neuron to the dendrite of another neuron. In general, neurons are generated from NSC during brain development in childhood. Neurogenesis in most regions of the brain essentially ceases in adulthood. Since neurons do not undergo mitosis, dead neurons cannot be replaced, which makes neural regeneration challenging.

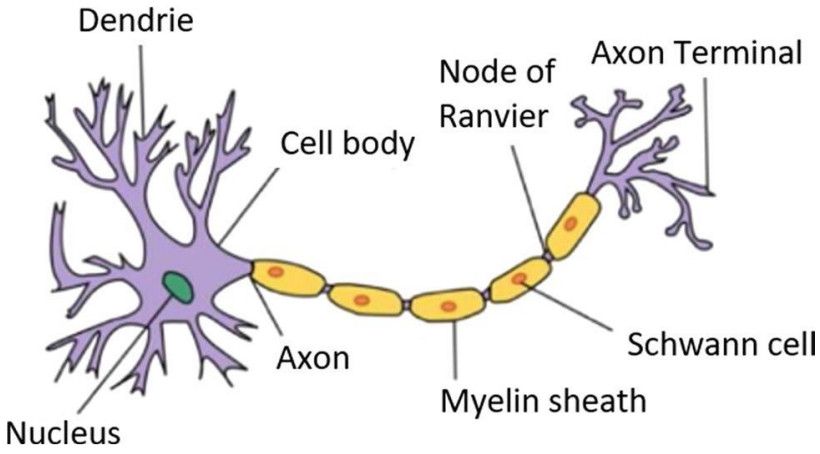

Schematic 1.1 Structure of a typical neuron [6].

1.1.1.2 Glial cells

Glial cells are a distinct population of non-neuronal cells devoid of the capacity to generate electrical impulses. Compared with neurons, glial cells possess greater

diversity and functions. Primary glial cell types include oligodendrocytes, astrocytes, and microglial cells (**Schematic 1.2**). Glial cells are important in several neurological functions: (1) producing myelin sheaths that surround the axons throughout maturity to support and provide nutrients to neurons; (2) controlling neuronal ion and neurotransmitter levels; (3) regulating synapses, which are basic functional unit of the nervous system [7].

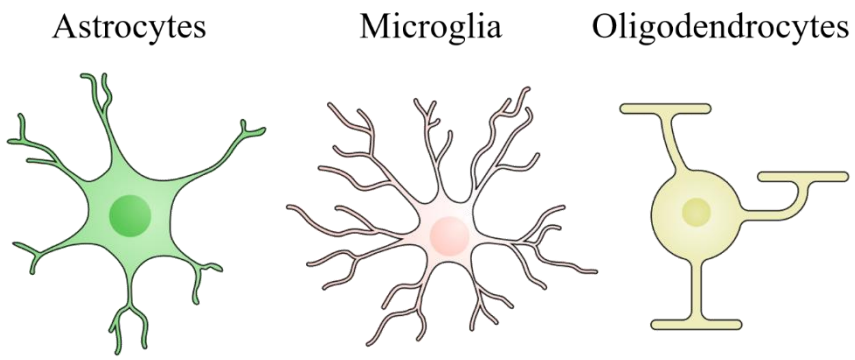

Schematic 1.2 Different glial cells [8].

1.1.1.3 Neural stem cell (NSC)

NSC are multipotent cells that exist in the central nervous system (CNS) and can develop into neurons and glial cells (**Schematic 1.3**). Like other stem cells, NSC could proliferate indefinitely. NSC is essential in embryonic development and are persist in stem cell niches of adults' organisms [9]. The ventricular-subventricular zone is a niche for adult NSC, which can differentiate into olfactory neurons [10]. The hippocampus is a hotspot for NSC, which generate new cognition neurons [11]. NSC has the potential to replace or repair dysfunctional cells in the nervous system, thereby providing new possibilities for neural regeneration [12].

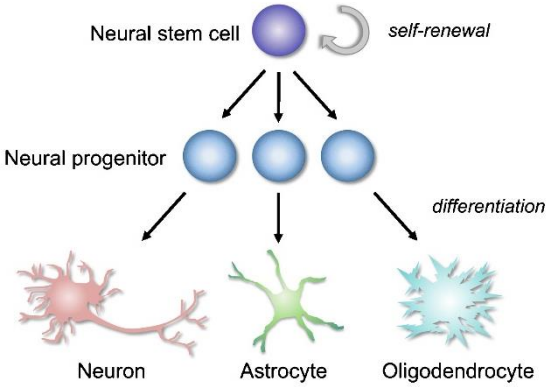

Schematic 1.3 The self-renewal and multipotency of NSC [13].

1.1.1.4 Engineered stem cells

Despite the promise of NSC in neural regeneration, it still suffers from the scarcity of sources, high heterogeneity of NSC characterisation and the difference between *in vitro* and *in vivo* cultivation [14]. Advances in cell culture technology and modern materials (bioactive hydrogels) offer a framework for simulating complex, physiological microenvironments; however, direct culturing NSC for *in vitro* investigation and *in vivo* regeneration remain challenging [15]. Engineered stem cells including induced pluripotent stem cells (iPSCs) and neuronal cell lines provide a reliable and sustainable supply of cells for neural research and therapy.

iPSCs

iPSCs are pluripotent stem cells derived from mature adult somatic cells (e.g., patient tissues) *via* gene expression reprogramming, which eliminates the risk of immune rejection when transplanted into the body. Meanwhile, iPSCs are also feasible to differentiate into neurons and glia cells, which makes them a valuable cell source for

neural tissue engineering. iPSCs have been used to develop *in vitro* neural disease models to provide insights into neural disease processes and improve *in vitro* drug testing efficiency. The transplantation of iPSCs has shown promise in preventing neuronal degeneration in the CNS of animal models. Despite these promises, the controlled differentiation and potential clinical application of iPSCs can be a lengthy process. Scientists and physicians must combine their expertise to transform these technologies into practical application [16].

Neuronal cell lines

Neuronal cell line is also an invaluable tool for study of neuroscience and neural regeneration. Although many cell lines are derived from tumour tissues, numerous studies have found little proof suggesting that the original cells are superior to human cell line models [17, 18]. Meanwhile, there are a number of advantages for neuronal cell lines in neural tissue engineering: Firstly, neuronal cell lines provide a nearly endless supply of homogenous cells for research applications. Secondly, they are easy to culture and can be stored in liquid nitrogen for a long time; Additionally, they could be easily induced to differentiate into various types of neurons during defined periods. Cell lines are also highly reproducible, making it easier to compare results across different studies.

Neuro2a cells

Owing to its neuronal and amoeboid stem cell characteristics, the mouse-derived

Neuro2a (N2a) cell line can develop into various cell types containing neurofilaments [19]. N2a cells generate many microtubules and are, therefore, sensitive to viruses, which may affect their cell shapes and functions. N2a cells are used to study a variety of neurological disorders and pathogens, including neurite outgrowth, neurotoxicity, Alzheimer's disease, asymmetric cell division, adenoviral transduction, and rabies [19].

SH-SY5Y

SH-SY5Y is a clone that can be obtained from the bone marrow biopsy of a human with neuroblastoma [20]. It is often used *in vitro* as a model of neurological function and differentiation. Owing to their adrenergic phenotype and dopaminergic marker expression, they have been used to study Parkinson's disease and neurogenesis.

PC12 cell line

PC12 is a cell line obtained from a pheochromocytoma of the adrenal medulla of a rat, with embryonic origins from the neural crest, which contains neuroblastic and eosinophilic cells [21]. PC12 cell lines have yielded an abundance of knowledge about the role of proteins in vesicle fusion. This cell line has been used to determine synaptotagmin functions in vesicle-cell membrane fusion. Although they are not considered adult neurons, their embryological origins in neuroblastic cells allow them to develop into neuron-like cells and release neurotransmitters through vesicles. When treated with nerve growth factor or dexamethasone, PC12 cells cease to proliferate and differentiate terminally [22]. Therefore, PC12 cells may serve as a model for neuronal

differentiation and neurosecretion.

1.1.2 Extracellular matrix

The ECM is a complex and dynamic network of macromolecules that can affect cellular activity, hence playing a crucial role in development [23, 24]. Formerly regarded as an inert scaffold, the vital significance of the ECM in crucial areas of cell biology has recently become more evident. Based on the number and arrangement of ECM components, the molecular scaffold of each tissue represents cell-specific activities. The physical, biochemical, and biomechanical features of the ECM are well-characterised by the structural, biochemical, and functional variety of its components [25]. Since these qualities and attributes are interconnected, they may impact one another, and these dynamic ECM alterations may influence cell function [26].

1.1.2.1 Compositions

Cellular processes in different tissues are represented by different molecular scaffolds that vary in terms of the size and composition of the ECM [26]. The neural ECM is rich in hyaluronic acid (HA) and proteoglycans. Lecticans - including aggrecan, versican, brevican and neurocan - are the most important family of chondroitin sulfate proteoglycans (CSPGs) in neural tissues. They congregate at somatic and dendritic synapses during the late stages of neural development, generating perineuronal nets (PNNs), which are similar to cartilage. Synaptic plasticity and maintenance require

PNN maturation. The enzymatic digestion of CSPGs promotes this by preventing long-term potentiation/depression and simplifying the activity of neuronal networks into more basic patterns. At the causative and modulatory levels, disturbances to the homeostasis of the neuronal microenvironment have been linked to pathological events in various neurological illnesses. In addition, numerous studies have revealed a connection between ECM modifications and brain trauma or Alzheimer's disease [27].

1.1.2.2 Biochemical cues

The ECM offers biochemical signals that govern cell-mediated repair or breakdown in adult organisms [28]. In brain tissues, natural biochemical signals are provided according to a specific spatial distribution and temporal sequence [29]. Focal adhesions and hemidesmosomes are formed when ECM ligands attach to cell surface receptors [25]. Such cells-ECM adhesions play critical roles in cell growth, proliferation, migration, and differentiation, and are essential in the transmission of microenvironmental signals generated or mediated by the ECM [30]. During brain development, gradients of biochemicals are closely localised and influence neuronal growth and differentiation [31]. For example, external gradients guide axonal growth and trajectories via long-range diffusion and short-range contact cues [32]. However, when the brain tissue is wounded or afflicted, its control of biochemical signals may be disturbed, resulting in cell death and the formation of regeneration obstacles [33].

The ECM acts as a reservoir for soluble molecules and controls their localisation, and

bioactivity [34]. The regulation is mediated by non-covalent interactions, such as electrostatic and hydrogen bonding, within ECM and soluble signalling molecules [25]. Fibronectin, for instance, serves as a receptor for several growth factors, encompassing fibroblast growth factors (FGFs), vascular endothelial growth factors (VEGFs), and platelet-derived growth factors (PDGFs). Additionally, heparin/heparin sulfate exhibits affinity towards fibronectin, VEGFs, and FGFs. Moreover, the surface of macromolecular skeletons within the ECM presents chemical functional groups, such a COOH, NH_2, and CH_3 groups, which directly engage in interactions with cells, thereby modulating their activities and functions [25].

1.1.2.3 Biophysical cues

Biophysically, the ECM communicates with cells via the macromolecular structure, network rigidity, and spatiotemporal fluctuations. Biophysical signals are crucial for neurogenesis, nerve repair, neuronal cell migration, and axonal development [35].

Anisotropic and hierarchically structured ECM structures can influence tissue performance and function. The breadth and density of fibres may influence the cellular responses; however, these effects are often relevant to the mechanical properties of the ECM and biochemical signals. Moreover, the ECM networks feature holes in their interstitial regions. The sizes and densities of the pores impede cell development by restricting the accessible space.

The mechanical characteristics of biological tissues span orders of magnitude, ranging from a few kPa for neural tissues to hundreds of MPa for bone tissues [3]. With Young's moduli of 0.50–6.63 kPa for the spinal cord and 1–4 kPa for the brain, nervous tissue is the softest tissue in the human body [36, 37]. The behaviour and fates of NSC are also regulated by biophysical cues. To be specific, NSC cannot survive in materials with Young's moduli lower than 0.1 kPa or higher than 100 kPa; they prefer a soft environment (1 kPa) for development into nerve cells and a stiffer environment (7–10 kPa) for differentiation into glial cells [38].

1.1.3 Soluble factors

Basic nutrients and soluble signalling molecules represent only some of the many soluble components that cells are exposed to in their watery *in vivo* environments. In terms of essential nutrients, oxygen is depleted quickly owing to its low solubility. The inefficiency of oxygen supply has been a significant barrier to developing tissue structures *in vitro*. Furthermore, different types of cells respond differently to changes in oxygen content [39].

As the most-studied soluble signalling molecules for biomimetic cell microenvironment manipulation, growth factors have received considerable attention in recent years [40]. Growth factors are produced by the same cell or neighbouring cells to give each developing cell a growth factor milieu (endocrine signalling). The

concentration gradients of these growth factors are similar and are tightly regulated both spatially and temporally, whether they freely diffuse in aqueous fluids or are confined inside the ECM.

1.1.4 Physical fields

Except for biochemical and biophysical signals, cells react to a diverse of physical stimuli, such as mechanical strain, stress, and electrical and magnetic fields. The ECM mediates physical signals, particularly tension and stress [41].

New technologies facilitate physiologically appropriate stress and strain for mechano-transduction studies of artificial tissue construction. Depending on the loading technique and parameters, these mechanical fields exert diverse effects on different cell activities. For example, stretching could stimulate the release of growth factors of muscle cells and thus induce the formation of new muscle fibers [42]. Similarly, in bone cells, mechanical stretching can stimulate the production of ECM proteins and mineralization, leading to bone growth and remodeling [43]. Shear stress is another type of mechanical stress that occurs when cells are exposed to fluid flow. This mechanical stimulation can activate signaling pathways and gene expression, leading to changes in cell behavior. For example, in endothelial cells, shear stress can stimulate the production of nitric oxide, which controls blood vessel dilation and flow [44]. In cartilage cells, shear stress can stimulate the production of lubricants and ECM proteins,

which help protect and stabilize joints [45, 46]. Additionally, electrical, magnetic, acoustic, and thermal forces may be applied to cells. For example, electric fields accelerate the development of cells and tissues in cardiac, skeletal muscle, and bone tissue engineering [3].

1.2 Microenvironment factors regulating neuronal differentiation

The clinical and industrial uses of neuronal differentiation processes are extensive. Neurons produced by stem cells have been extensively applied in basic neurological research, drug screening platforms, neurodevelopmental and neurodegenerative disease modelling, and cell-based treatments for neurological illnesses [47, 48].

1.2.1 Biochemical environments

In addition to tissue homeostasis and repair, a variety of biochemical inducers control processes, including cell division, differentiation, and growth. The majority of these inducers are proliferative peptide hormones or chemical substances.

1.2.1.1 Growth factors

Growth factors are critical in neural regeneration. NSC in the CNS are more likely to survive and differentiate into neurons when exposed to growth factors, such as brain-derived neurotrophic factor (BDNF), basic fibroblast growth factor (bFGF), nerve growth factor (NGF), and neurotrophic factors. They affect PI3K/Akt and other signalling pathways to improve adipose stromal cells (ASC) survival and activity, producing morphological and migratory alterations. In addition, the cytoskeleton of growing cells is modified to mimic fibroblast processes via the polarisation of Rho/myosin II components [49].

Hepatocyte growth factor is an additional neurotrophic factor that allows sensory and parasympathetic neurons to survive longer and proliferate. It functions as a growth factor for neocortical explants and as a chemoattractant for the axons of spinal motor neurons. Mesenchymal stem cells (MSCs) may be encouraged to develop into neuroglia by combining bFGF and NGF with retinoic acid (RA). Stem cells tend to develop into oligodendrocytes when the neurotransmitter nor-epinephrine is introduced [50].

1.2.1.2 Chemical compounds

Certain chemicals may also stimulate neuroglia. By increasing cysteine absorption and intracellular glutathione levels, β-mercaptoethanol promotes neuronal survival in culture [51]. Butylated hydroxyanisole, valproic acid, insulin, and potassium chloride have also been used to stimulate neuronal and glial differentiation [52]. Similarly, ethanol, valproic acid, and hormones, such as hydrocortisone and insulin, may also induce neuronal differentiation of NSC [53]. Although the independent effects of these chemical inducers on neuronal differentiation have been fairly understood, the use of these chemical compounds has been limited because of their toxicity. How to reduce the toxicity of chemical inducers and the combined effects of chemical compounds would be the focus of investigation in the future.

1.2.2 Mechanical microenvironments

The mechanical microenvironment comprises mechanical support, environmental

pressures, and forces in the ECM, produced by cellular interaction with surrounding support cells. Neural stem cell growth, division, and differentiation are intrinsically linked to the mechanical niches in which they reside. NSC can perform their numerous roles regularly in a physiologically mechanical environment, but when this environment changes, stem cell capabilities are altered too. Substrate topology, substrate stiffness, shear stress, tension strain, and stress represent only some of the mechanical microenvironmental factors that should be investigated to better understand how they affect stem cell proliferation and differentiation.

1.2.2.1 Topography structure

Stem cells benefit from topography at micro- and nano-scale levels. Cell alignment, polarisation, extension, migration, differentiation, and gene expression are regulated by a combination of chemicals bound to the substrate and scaffold physical features. Recent *in vivo* studies have shown that physical signals, such as surface topography, are important for the proliferation of stem cells. For example, radial glial cells move alongside neuronal cells during cerebral cortex development. Through the manipulation of micro- and nano-scale patterns on substrates, stem cell fates can be effectively modulated by inducing alterations in cytoskeletal alignment and intracellular assembly of focal adhesion proteins. The structures of the nanomaterials used for ECM have also been shown to affect stem cell behaviour. Using electrospun nanofiber scaffolds for peripheral nerve regeneration, Jaswal *et al*. discovered that graphene-encapsulated gold nanoparticles in poly(caprolactone) (PCL) fibre scaffolds approximated the natural

ECM and promoted cell differentiation and neural network creation [54]. When various copolymers were added to PCL, the rat neural stem/progenitor cells (NSPCs) could differentiate into astrocytes and neurons without a growth stimulus, highlighting the importance of fibre nanotopography.

1.2.2.2 Mechanical stiffness

Stem cell activities, including differentiation and self-renewal, are increasingly being attributed to mechanical features of the cellular microenvironment [55]. For example, the alterations in cytoskeletal tension and the activation of the mechano-transduction signalling complexes and transcription factors are controlled by spatial and temporal variations in ECM stiffness, which regulate stem cell activity. In addition, advances in materials have provided access to substrates with precisely regulated qualities (e.g., biochemical composition, mechanical strength, biocompatibility, and protein functionalisation). By growing stem cells in such a scaffold, a desirable cell fate may be induced by mechanical stimulation.

In a ground-breaking study, polyacrylamide gels with elasticities between 0.1 and 1 kPa were covered with collagen I and applied to induce neural development of human mesenchymal stem cells (hMSCs) without a soluble factor. Immunofluorescence, western blotting, and microarray analyses indicated that hMSCs acquired a neuronal shape and expressed a wide variety of neuronal markers. Furthermore, the hMSCs were permanently committed to a neuronal cell destiny after three weeks of growth on these

soft substrates, despite myogenic and osteogenic inducers [56].

Stem cell responses to stiffness variation have also been studied using laminin-coated methacrylamide chitosan (MAC) hydrogels. The proliferation and differentiation of NSC improved on scaffolds with elasticities lower than 1 kPa. In addition, Functionalising MAC hydrogels with the same stiffness as that of brain tissue increased the efficiency with which NSC underwent neuronal differentiation compared to NSC treated with BDNF [57].

Polydimethylsiloxane (PDMS) substrates with varying stiffness were also used for NSC culture. In this study, the maximum rate of astrocyte differentiation was observed on soft substrates, but the rate of oligodendrocyte differentiation was independent of the substrate stiffness. Although the total number of mature and differentiated neurons was unrelated to stiffness, the degree of stiffness significantly impacted the process, as neuronal axon growth and synaptic protein expression improved in brain-like stiffness scaffolds [58].

1.2.2.3 Mechanical strain and stress

Native NSCs exist in a constantly changing dynamic niche, which are essential regulators of cell survival, proliferation, metabolism, and differentiation [59]. Increasing evidence suggests that the fate of NSC is also influenced by mechanical cues, such as shear forces, fluid flow, mechanical stretching and compression [60]. Recent research has shown that external physical stimuli may be converted into intracellular

forces to regulate gut organoid development via Wnt/β-catenin signalling [61]. In particular, stretching might enhance neuronal development, axon growth, and neurite outgrowth.

In similar studies, cyclic stretching alone has been shown to cause neurite outgrowth of PC12 and SH-SY5Y cells, and induce the differentiation of NSC into neuron-like cells [62]. Moreover, stretching has been shown to stimulate neurite development in adult neurons. A 10% cyclic stretch stimulates the neurite outgrowth of neurons, and strains may stimulate axon development and branching [63]. However, these studies have drawn contradictory conclusions regarding the cyclic strain amplitude that produces neurite outgrowth or neuronal differentiation. This may be related to the various cell types and the maturation levels of the brain cells.

During CNS development, cell sheet motion and tissue folding put endogenous NSPCs under local physical stress. In CNS impairment, there is immediate physical straining of the brain tissue; this has been reproduced *in vitro* using equibiaxial stretching, which dramatically alters the functions of neurons and glia. Despite the lack of research regarding the effects of mechanical stretching upon neuronal differentiation in the CNS, it has been shown that progressive mechanical stretching promotes the lengthening and maturation of adult rat hippocampus NSPC-derived neurons. The existence of mechanical forces throughout development and in traumatic conditions necessitates the identification of their effects on NSPC differentiation [64].

1.2.2.4 Supramolecular interaction

In addition to traditional macro mechanics discussed above, micromechanics (supramolecular interaction) is ubiquitous in the ECM and exerts a fundamental role in regulating cell behaviour including cell migration, proliferation, differentiation, and apoptosis. Among various kinds of supramolecular interaction, host-guest is noteworthy within the realm of biomedicine owing to their inherent tunability and dynamic characteristic which allow force-induced dissociation/association. Yang *et al*. developed a sliding hydrogel by host-guest interaction for 3D stem cell culture and differentiation [65]. The study found that the fluidity of the sliding hydrogels allowed the recombination of cells and rearranged the hydrogel network, which enhanced the differentiation of NSC into multiple lineages. In another study, Alexandra *et al*. developed a host-guest dynamic supramolecular polymer and investigated the effect of a dynamic matrix on neuronal activity [66]. They demonstrate that host-guest interactions can promote neuronal infiltration and activate the biological activity of neuronal receptors. Furthermore, supramolecular hydrogels have shown great promise for *in vivo* neural regeneration. Multiple studies have shown that supramolecular hydrogels can promote axon growth and synapse formation, which bring an emerging choice for nerve injury and neurodegenerative diseases [67].

1.2.3 Electrical environments

The electrical properties of neurons and their microenvironment are indispensable for

the function of the nervous system. Information transmission occurs via electrical impulses generated by nerve cells. It was reported that the conductivity of neural tissue is range between 8×10^{-4} to 4×10^{-2} S/m [68, 69]. Given the intrinsic electrical properties of neurons, the electric signal is also a possible trigger for neural stem cell differentiation. Electrical field has been explored to promote neuronal differentiation by modulating the electrical properties of NSC and promoting the expression of genes associated with neuronal development [70]. The mechanism by which electrical stimulation induces neuronal differentiation is complex and is still being studied, but some of the proposed mechanisms include modulation of ion channels and activation of intracellular signaling pathways (MAPK/ERK and PI3K/Akt pathways) [71].

Conductive materials provide a promising choice for study of electrical stimulation on neuronal differentiation *in vitro*. These materials can provide a conductive environment that mimics the natural electrical properties of the nervous system and allow the application of ES to NSC in them to investigate the mechanisms underlying the effects of ES on neuronal differentiation. Several conductive materials, including polypyrrole (PPy), PEDOT, and polyaniline (PANi), have been used as scaffolds to regulate stem cell activity [72, 73]. These substances include repeated single and double bonds with overlapping pi bonds (pi-type), which enhances the transfer of free electrons between atoms. When cultivated on 0.1M HCl-doped PANi substrates, MSCs underwent conductivity-dependent neuronal differentiation, demonstrating properties previously associated with neurons. Surfaces with different conductivities (e.g., PANi) facilitated

the electrical stimulation of MSCs, increasing neuronal marker expressions. NSC could differentiate into mature neuron-like cells on a PANi substrate after exposure to a continuous potential of 1.5 V, even without doping treatment. In a separate investigation, significant filopodial elongation, decreased nestin expression, and increased Tuj-1 expression were also observed in MSCs [74].

In addition, electrical currents may also encourage the migration of neurons cells, and can direct the formation of neurites. In research exploring the effects of ES on MSC, ultra-low-frequency pulsed electromagnetic fields have been reported to induce the production of osteocytes and osteogenic genetic markers. Both axonal myelination and osteocyte differentiation are boosted by ultra-low-frequency electrical stimulation [75].

1.2.4 Magnetic environments

Magnetic stimulation has been used as a non-invasive therapy for controlling neural activity and inducing neuronal differentiation [76]. The underlying mechanism through which magnetic stimulation induces neuronal differentiation is not yet fully understood but is thought to involve the hinge of the effects of calcium and cyclic adenosine response element-binding protein (CREB) [77]. To be specific, electromagnetic stimulation can accelerate intracellular and extracellular calcium ion exchange and increase the voltage-gated calcium channels during the differentiation process. The transcriptional regulator CREB may be phosphorylated by calcium influx, which then

attracts more calcium-binding proteins to trigger the neuronal differentiation process [77]. In addition, both the CREB and epigenetic pathways can influence the production of BDNF, which plays a crucial role in NSC activity. Liu *et al.* have found that low-frequency magnetic stimulation can enhance the development of mature neurons from iPSCs while high-frequency magnetic stimulation may promote differentiation into glutamatergic neurons [76]. Furthermore, intermittent theta-burst magnetic stimulation could promote the formation of synapse.

The bromodeoxyuridine (BrdU) and nestin incorporation techniques have demonstrated that electromagnetic fields (EMFs) can also enhance BrdU and nestin in the region of subventricular zone (SVZ), indicating that EMFs have a significant influence on the proliferation and migration of NSC [78]. According to Cuccurazzu *et al.*, extremely low-frequency and low-intensity EMF stimulation increases adult hippocampus neurogenesis [79]. Moreover, Arias and co-workers demonstrated that activation of the transcranial magnetic field stimulates neurogenesis in SVZ cells after nigrostriatal injuries [80].

1.3 Biomaterials for the design of biomimetic microenvironments

Biomaterials for the creation of bio-inspired microenvironments should replicate cell growth, proliferation, differentiation, and cell death in terms of their composition, structural characteristics, mechanical properties, degradability, and electrical conductivity.

1.3.1 Natural biomaterials

Early biomaterials, many of which are still in use today, were derived from natural sources and are chemically and structurally similar to damaged tissues. Host cells can recognise natural biomaterials, thereby minimising rejection; this is the driving force behind their adoption [81]. In addition, naturally occurring polymers promote cell adhesion and proliferation. Scaffolds comprising pure ECM molecules (e.g. collagen or other proteins, HA, and specific polysaccharides) have been used in addition to matrices based on generic mixes of ECM components [82]. However, the mechanical characteristics of biomaterials of natural origin are insufficient, and they biodegrade too quickly to provide sufficient support. These biomaterials can be manufactured in numerous ways, including *in situ* gellable solutions, scaffolds, fibres, and conduits [83].

1.3.1.1 Collagen

As an essential structural protein of mammalian ECM, collagen constructs networks

and threads that provide a physical framework and vital metabolic signals for sustaining cells and tissues. Collagen plays a crucial role in nerve formation and maintenance. It also offers excellent support for cell proliferation and may promote the differentiation of a wide variety of cell types [84].

Collagen hydrogels fill lesion deficiencies in nerve conduit channels, promote axon development in the collagen matrix, and enhance sensory function [85, 86]. 3D collagen scaffolds have been printed using cryogenic direct-plotting technology, wherein the extruded collagen is promptly frozen to preserve its structure [87]. Yoo *et al*. discovered that 3D-printed collagen scaffolds provide a biomimetic environment for neural regeneration, which promotes axon regeneration and remyelination [88]. Due the excellent neural regeneration effects, collagen-based products for are commercially available now (e.g., NeuraGen (Integra) and NeuroMatrix (all Stryker)) for never repair [89].

1.3.1.2 Gelatin and GelMA

Gelatin, a protein derived from collagen, has demonstrated significant promise in neural tissue engineering [89]. Compared to collagen, gelatin has improved water solubility, reduced immunogenicity, and retained its high biological activity. However, the weak crosslinking (soluble at body temperature), limited mechanical strength and easy degradation limited its application. Fortunately, the development of chemically modified gelatin-methacryloyl (GelMA) has addressed the above limitations and

expanded the applications [90, 91].

GelMA has gained increased popularity in neural tissue regeneration, including cell transplantation, drug delivery, and nerve repair due to its excellent properties [90, 92]. Firstly, GelMA is similar to the natural ECM and possesses the arginine-glycine-aspartic acid (RGD) sequence for cell adhesion and growth, which contributes to its excellent biocompatibility. GelMA hydrogel can be crosslinked rapidly, in just one minute or even a few seconds. Furthermore, the mechanical properties of GelMA can be tuned to the desired condition through various methods, from varying the gel concentration to more complex methods such as co-polymerization.

Many studies have demonstrated the excellent performance of GelMA hydrogel in nerve regeneration. Zhou *et al.* found that GelMA hydrogel loaded with NSC can promote motor function recovery and neuronal differentiation in rats with hemicomsected spinal cords [93]. Chen *et al.* used parallel modified-electrode rods to align GelMA hydrogel into fibrous bundles, which can guide neuronal cell migration or axon extension [94]. Additionally, other researchers have used dopamine-functionalized GelMA hydrogel as a scaffold to induce NSC differentiation. Dopamine in the GelMA hydrogel scaffold can promote neural network formation and enhance neuronal differentiation [95].

1.3.1.3 Hyaluronan

Hyaluronan, also known as hyaluronic acid, is a linear glycosaminoglycan comprised of alternating of D-glucuronic acid and N-acetyl-D-glucosamine units. Interest in the field of neural tissue engineering has been sparked by discovering that HA, an extracellular component of the CNS, may stimulate neurite formation [96]. Combining low-power laser irradiation with transplanting foetal spinal cord nerve cells into an adult rat's transected spinal cord led to axon regeneration and a partial recovery of locomotor function. Immobilised HA hydrogels containing cell-adhesive oligopeptides assisted in regenerating wounded brain tissue and axon regrowth. Angiogenesis was induced in rat cortical lesions when RGD- or isoleucine-lysine-valine-alanine-valine (IKVAV)-modified hyaluronic acid hydrogels were implanted [97].

The esterification of hyaluronic acid greatly improves resistance to biodegradation. The biodegradation rate is proportional to the level of esterification. Benzylated hyaluronans were shown to be stable in water for extended periods. Twenty days after subcutaneous implantation in rats, the ethyl ester of HA was completely dissolved, although the benzyl ester remained stable even after 90 days. The breakdown products of benzylated hyaluronan are harmless to cells. Hyaluronan hydrogels were also prepared by replacing some of the polysaccharide backbones with methacrylate groups, followed by cross-linking the resulting molecule with light. The holes in these hydrogels were ~50 μm in diameter and possessed an isotropic open porous architecture [98].

1.3.1.4 Fibrin

Fibrin is a fibrillar protein primarily responsible for blood coagulation. Fibrinogen meshes and produces fibrils in the presence of calcium ions and thrombin, forming a plug or clot at the site of the injury.

Fibrin gels have been used to transport NGFs. Schwann-cell-containing fibrin has been used as a luminal filler to stimulate axonal regeneration. The addition of neurotrophic and Schwann cells to fibrin has also been applied to regenerate the sciatic nerves of rats. Inkjet printing has made it possible to build layers of brain cells and fibrin and produce a 3D structure [99].

Fibrin sealant has also been effective in rats with severed sciatic nerves. In addition, fibrin binds to hyaluronic acid and the von Willebrand factor. Fibrin may interact with integrins in Schwann cells via its RGD and two AGDV sites. The binding of fibronectin to fibrin provides an extra benefit for Schwann cells because fibronectin enhances their proliferation [100].

Neurite outgrowth from the dorsal root ganglion neuron is affected by the concentration of RGD peptides used to alter the fibrin backbone and improve fibrin hydrogel properties. The density of the adhesion sites had the greatest effect on neurite extension when it was moderate and the least effect when it was high [101].

1.3.1.5 Alginate

Alginate is a naturally occurring polysaccharide with a prospective function in tissue engineering. The linear polysaccharide alginate is generated from brown algae and other microorganisms. It consists of a polymer chain comprising (1-4)-linked D-mannuronic acid (M) and L-guluronic acid (G) due to the binding of divalent cations to the G-units, and gels quickly. This binding results in the distinctive transformation of the alginate structure into the so-called "egg-box" shape [102].

Native or unmodified alginate is a poor substrate for mammalian cell adhesion. These cells lack receptors that adhere to alginate, rendering the development of processed cells impossible without alginate modifications. The combination of collagen, fibronectin, laminin, or cell-adhesive peptides with alginate has shown tremendous promise for peripheral nerve regeneration and spinal cord injury therapy [83].

1.3.2 Synthetic biomaterials

The application of synthetic biomaterials is another common practice. Synthetic biomaterials can be manufactured using a wide range of methods and architectural designs specific to the tissue type. Hence, these materials appear to compensate for the shortcomings of natural biomaterials [81]. In addition, biodegradability can precisely be regulated by choosing the appropriate polymer or its composition. However, they also have drawbacks, such as reduced bioactivity, which increases the post-implant

rejection risk. Given that many systems are composed of a variety of biomaterials, understanding the origins of these biomaterials is necessary [103].

1.3.2.1 Poly (2-hydroxyethyl methacrylate) (pHEMA)

pHEMA could be crosslinked using dimethacrylate monomers for polymerisation. Hydrogel tubes made from pHEMA polymers have mechanical properties analogous to those of the spinal cord. The morphology displays a microporous layer on the inside and a gel-like layer on the outside. By altering the monomer composition and surface chemistry of the molds used to make the tubes, these mechanical and morphological qualities have been reported as viable treatment for spinal cord injuries [104].

Several studies have investigated the efficacy of different pHEMA types. Adult rat spinal cords were implanted with p(HEMA-MMA) tubes, resulting in the development of axons and the construction of tissue bridges inside the tubes. However, axons did not traverse the entire length of the tube; the astroglia did not penetrate the tube but instead surrounded it [105].

1.3.2.2 Poly (ethylene glycol) (PEG)

PEG is a hydrophilic polymer that is linear and has a low binding affinity. It is a biodegradable polymer comprising ethylene oxide (EO) units. PEG is extremely biocompatible and suitable for hydrogels owing to its hydrophilic and biochemically inert qualities, which are essential for nutrition and waste transfer. In addition, PEG is

resistant to protein absorption and is non-immunogenic. However, unlike the natural polymers employed in hydrogels, PEG is not bioactive and is often combined with other bioactive polymers [106].

PEG hydrogels have been widely utilized in neural tissue engineering [107]. Neuronal cell culture on PEG platforms improves neural cell survival, proliferation, and differentiation, suggesting considerable potential for treating CNS ailments. Hydrogels can be developed and manufactured in many forms (2D or 3D). However, the features and qualities of the design seem to have a greater impact on neuronal cell behaviour in 3D than in 2D cultures. For 2D PEG cultures, Lampe *et al*. demonstrated that hydrogel characteristics did not influence metabolic or apoptotic activities but influenced cell proliferation and glial cell reactivity [108]. In 3D PEG cultures that closely resembled the stiffness of the original brain tissue, the metabolic activity, proliferation, and apoptosis rates were enhanced.

The adaptability and lack of toxicity of PEG have allowed for preclinical testing and intravenous administration after brain damage. After severe traumatic brain damage, an intravenous injection of PEG reduced cerebral cell loss and delayed the degeneration of wounded axons to the extent that the brains of PEG-treated mice resembled those of uninjured animals. Moreover, PEG has shown promise in treating spinal cord damage by considerably accelerating and improving the process of membrane resealing and restoring mechanical integrity after compression.

1.3.2.3 Conductive materials

Conductive polymers were discovered midway through the 1970s and gained attention regarding their biological use in the 1980s. In addition to possessing qualities comparable to those of conventional polymers, conductive polymers exhibit desirable and controllable electrical properties [109]. Conductive polymers are combined or copolymerised with degradable polymers to produce conductive biomaterials owing to the weak cell adhesion, inability to biodegrade, and limited mechanical control. Conductive biomaterials with anisotropic conductive characteristics have been developed to promote neurite extension and enhance myoblast growth. PEDOT:PSS and their derivatives are probably the most well-known organic conductive materials owning to their exceptional electrical conductive attributes, adhesion to substrates, tuneable mechanical properties, and biodegradability [110, 111]. As shown in **Schematic 1.4** PEDOT:PSS is a composite material composed of two different PEDOT and PSS, which work together to create a material that possesses the unique properties [112]. The principle of conduction in PEDOT: PSS is based on the movement of charge carriers, specifically electrons, and holes, through the polymer matrix. PEDOT is a conjugated polymer that allows for the movement of electrons through the polymer chain, while PSS provides charge balance and stabilizes the PEDOT backbone. When PEDOT:PSS is doped with a counterion, such as p-toluene sulfonate (PTS), it becomes a p-type semiconductor, meaning that it has an excess of positive charge carriers or holes. The holes can move through the polymer matrix by hopping from one PEDOT chain to another, and the application of an electric field to PEDOT:PSS separates the

holes and electrons, creating a current flow through the material. Maintaining the electrical conductivity of the hydrogel matrix while supporting the growth and function of cells remains a significant challenge, despite the potential benefits of conductive hydrogels for personalizing of the 3D cell microenvironment [72].

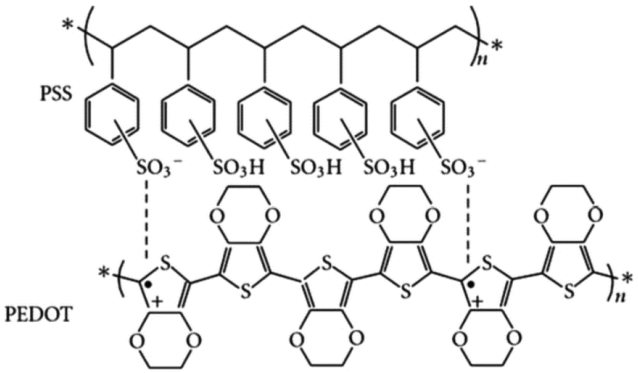

Schematic 1.4 The structure of PEDOT: PSS [112].

Carbon-based nanomaterials, including carbon nanotubes (CNTs) and graphene, represent a distinct category of conductive materials extensively employed in diverse biomedical applications [113]. Conductive hydrogels made from CNTs have been created for cardiac and neural tissue engineering applications. In biohybrid actuators, the excitation thresholds and beating frequency are affected by the orientation of the electrical signals with respect to CNTs, which are typically vertically oriented. Hydrogels have been mixed with carbon nanofibres, graphene, and graphene derivatives to create conductive hybrids. The popularity of graphene stems from its plethora of useful properties, including its malleability, high electrical conductivity, and solubility in water. Progressions in the production and performance of conductive hydrogels based on carbon nanomaterials have been attributed to the toxicity of CNTs and reduced graphene oxide.

1.4 Technologies for constructing biomimetic nerve network models

In vitro models of CNS are in great demand for studying neurological illnesses, injuries, regeneration, and therapeutic effectiveness. As a result of the closer physiological relationship between 3D models and *in vivo* conditions, 3D-cultured neuronal models exhibit superior survival and distinct cell behaviours compared to 2D-cultured models [114]. The cultures of 3D models are compatible with intracellular and extracellular electrophysiological methods, which is very important. Various technologies can be used to construct biomimetic nerve network models, including conventional methods, self-assembly, microfluidic channels, and 3D printing, as briefly described in the following sections.

1.4.1 Conventional methods

Solvent casting and particle leaching are standard processes for fabricating three-dimensional brain models. To produce a scaffold, the polymer is dissolved in an organic solvent and then poured into a mould. The scaffold is moulded into the proper form/dimensions by applying salts to obtain the necessary geometry. Popularly available leaching agents include sodium chloride (NaCl) and sugar. Kaplan *et al*. constructed 3D tissue models that enhanced the development and long-term survival of functional brain networks [115]. Adapting this paradigm to iPSCs facilitates a more direct investigation of the human situation. Diverse cell types, including neurons and

astroglia cells, interact in these 3D tissue cultures, exhibiting spontaneous neuronal activity (as validated by electrophysiological recordings and calcium imaging over at least nine months). This tissue model can be employed to identify early-stage disease biomarkers, facilitate earlier illness detection, and enhance our knowledge of disease development.

1.4.2 Supramolecular self-assembly

Through non-covalent interactions, molecules and components self-organise into patterns or architectures of nanofibres, resulting in malleable, randomly oriented networks known as self-assemblies. When used in neural tissue engineering, self-assembled nanofibrous scaffolds offer several advantages, and their fast recovery not only enhances the lifetimes of materials but also restores their original properties [116].

Peptides can self-assemble into a helical, sheet, or hairpin structure, which can then be used to construct 3D scaffolds for studying human neuronal reprogramming and maturation. Human neurons generated from iPSCs in self-assembling, peptide-containing nanofibrous scaffolds have shown impressive functional activity. Alongside increasing neuronal survival, RADA16-I scaffolds also increase neurite length by hundreds of micrometres inside the host brain tissue. The IKVAV amino acid sequence promotes neurite outgrowth. Nanofibrous hydrogel scaffold structures are formed *via* the self-assembly of IKVAV molecules in neural progenitor cells (NPCs) cultures.

Consequently, NPCs cultured in 3D scaffolds develop neurons faster than those grown on the hydrogel surface. Therefore, the self-assembly of this hydrogel suggests that it may comprise a useful component for neural tissue regeneration [117].

1.4.3 Microfluidic channels

Microfluidic technology is sometimes called a lab-on-a-chip or a micro-complete analysis system. This approach has been widely used in gene and protein analysis, drug toxicity, multidrug resistance, cell cultures, and tissue engineering [118]. Microfluidic channels have been used to link axon and neuron chambers to create biomimetic nervous system models [119]. Nervous system models offer novel and effective research platforms for studying injury, degeneration, and regeneration in the nervous system. By altering the microenvironment of the system, these models can easily imitate chemical or physical nerve injuries [120]. Using precision manufacturing technology, microfluidic technology and traditional 3D techniques have been combined to create microfluidic biomimetic models [121]. Microfluidic biomimetic models can generate a regulated microenvironment using microchannels to provide steady nutrition and other chemical compounds. Their microscale dimensions are congruent with the microstructure and microenvironment *in vivo*, making it simple to create microenvironmental conditions comparable to those seen in the human body [122].

Using a PDMS microfluidic system comprising a pyramid-shaped cell culture chambers,

Yin *et al*. investigated the optimal local concentration of tacrolimus for peripheral nerve regeneration [123]. In addition, *in vitro* models of the blood-brain barrier can be created by integrating models of the neurological system with the architectures of blood arteries to examine the trafficking of medications, nutrients, metabolites, and other substances between the blood and CNS. Owing to the failure of the blood-brain barrier, these microfluidic biomimetic models may be useful for studying certain neurological disorders, including Alzheimer's disease and disseminated sclerosis.

1.4.4 Three-dimensional bioprinting

Bioprinting is a promising approach that combines biomaterials, bioactive chemicals, and cells to create 3D cellular constructs that mimic the brain architecture *in vivo* [124]. This can facilitate personalised biomedical device applications that apply combinatorial strategies to address brain regeneration issues. 3D printing integrates 3D imaging with robotics-based biomanufacturing for anatomical precision, diverse bio-inks with adaptability and quick prototyping for combinatorial sampling. When replicating complicated systems (e.g. the nervous system), these qualities are preferable to alternative methods.

First, 3D printing customises scaffolds for the nervous system and trauma recovery. Using 3D imaging and topological data, scaffolds can be designed to fit the 3D microenvironment of each injury. The cell-to-cell contact generated by 3D printing may

enhance the regenerative abilities of the transplanted cells. To improve brain networks, 3D printing can be used to route regenerated axons [125].

Direct 3D printing achieves the best and most effective localisation by printing the appropriate cell types or biomolecules directly into the necessary scaffold, which allows for the creation of more physiologically relevant models [126]. Regeneration of the orthotopic nervous system can be enhanced by adding cells or chemicals to regionally tailored conduits.

Lastly, 3D printing can increase the complexity of neural networks. 3D printing with sacrificial hydrogel ink can create complex circulatory and brain networks [127]. Specific cells and growth factors can be used to construct a neurovascular system. Basic research into translational drug discovery can be applied to create microenvironmental platforms for nervous system function, disease modelling, and pharmacology studies [128].

While bioprinting has many advantages for constructing biomimetic nerve network models, there are also challenges that need to be addressed including the accuracy of 3D printing, integration of multiple cell types, and cell viability and functionality after printing. The development of ideal bioinks with adequate biocompatibility and excellent printability would be the promising solutions to these challenges. Recently, an increasing number of studies have focused on developing bio-inks with high

biocompatibility and printability to print NSC directly into desired shapes without affecting cell viability. For example, Gu *et al*. constructed lattice-shaped mini-neural tissue via the bioprinting of NSC within hydrogel matrices [129]. Printed NSC exhibited high viability and could differentiate into neuronal and glial cells *in situ*. The calcium imaging results also demonstrated that the printed neural mimics had functional neurons, which could be used as a platform for neural development and neural network formation. Zhou *et al*. developed a novel bio-ink with enhanced neuronal differentiation abilities using dopamine-modified GelMA [95]. NSC seeded on printed scaffolds showed excellent neural network formation and promoted gene expression. These studies highlight the importance of mimicking the neural tissue microenvironment and the potential of bioprinting for developing neural tissue mimics that better replicate neural tissue complexity.

1.5 Biomedical application of *in vitro* nerve network models

1.5.1 *In vitro* nerve network models for pathophysiological studies

Parkinson's disease and Alzheimer's disease (AD) are linked to growing brain dysfunction. Despite the increasing number of CNS studies, our understanding of brain function remains largely insufficient, and the *in vivo* study of the human brain has numerous limitations. Future models of the physiology, pathology, and pharmacology of the nervous system will incorporate 3D neural mimics [130].

AD is a neurodegenerative pathology typified by neuronal death, cognitive impairment, and memory loss. Despite numerous attempts, several therapies targeting AD-related pathways have proven unsuccessful in animal models. The research on AD has faced challenges in understanding the pathophysiology of late-onset Alzheimer's disease (LOAD) and developing effective treatments to prevent or reverse the disease-related physiological changes. To address these issues, iPSC-based neural models have been employed to replicate Alzheimer's disease features in the CNS, enabling the exploration of AD pathology and facilitating drug screening. Notably, both LOAD and early-onset Alzheimer's disease (EOAD) iPSCs can generate cortical neurons exhibiting AD characteristics. This phenotypic variation highlights the importance of subclassifying AD patients and neurons when conducting drug screening studies [131].

Kaplan *et al*. developed a 3D iPSC human brain model utilizing embryonic mouse brain

cells by including human cells from healthy individuals as well as AD and Parkinson's disease patients [115]. The evaluation of this tissue model involved the utilization of stem cells derived from individuals with Alzheimer's and Parkinson's diseases. Electrophysiological assessments were conducted to evaluate the functional activity of the 3D brain tissue models, which demonstrated robust activity. Furthermore, genetic profiling conducted on the 3D models revealed tissue differentiation, neuronal cell proliferation, and cell type selection. These findings have significant implications as they can be employed to identify early disease markers, thereby facilitating earlier diagnosis, and enhancing our understanding of disease progression and development.

1.5.2 *In vitro* nerve network models for drug screening

Despite breakthroughs in neuroscience, treating nerve illnesses is tough. It is difficult to measure pharmacological effects owning to the vast array of potential secondary targets, encompassing both neuronal and non-neuronal elements [132]. Drug development is associated with significant adverse consequences, as evidenced by the fact that less than 10% of proposed drugs successfully receive clinical approval. The development of medications for neuropathy in Phase II and III are particularly affected, experiencing a delay of 8.1 years due to high attrition rates observed in clinical trials. Importantly, numerous clinical impairments emerge at a late stage in these trials, indicating a disconnect between the findings from preclinical studies and the outcomes observed in hospitalized patients. This disparity highlights the need for improved

translation of preclinical findings into clinical settings to enhance the effectiveness and efficiency of drug development processes.

Animal models used *in vivo* to anticipate the effects of medications. Drosophila and zebrafish are capable of high-throughput testing and rapid screening for toxicity. Because gene expression and cellular metabolism are distinct, animal models have problems accurately simulating human disease etiology and treatment response. Behavioral tests or *in vivo* electrophysiological measurements of cerebral activity (e.g. EEG) have been the primary focus of early preclinical safety inspections [133]. These techniques hinder a comprehensive understanding of the mechanistic and molecular bases of neural network function changes [114].

In vitro models of neurons exhibit remarkable similarity to their natural counterparts in terms of cell type diversity, intracellular communication, cell-matrix interactions, and nutrient transport. Among these models, 3D-cytoarchitectural cultures represent a more advanced *in vitro* approach compared to monolayer co-cultures, particularly in the context of drug toxicity evaluation. The three-dimensional nature of cytoarchitectural cultures provides a more physiologically relevant environment, allowing for improved recapitulation of cellular behavior and response to drugs. As a result, 3D-cytoarchitectural cultures hold great potential as a valuable tool for investigating drug toxicity and improving our understanding of drug effects on neuronal cells. Sirenko *et al*. conducted a study focusing on drug toxicity using 3D human iPSC brain spheroids

as a model system. In this study, the researchers explored the capacity of 3D spheroids to identify potential hazards by subjecting them to various neuroactive chemicals and neurotoxins [134]. To assess cytotoxicity-induced disturbances or seizures in iPSC-neurons, a calcium oscillation assay was employed, which detects intracellular calcium alterations. This assay was particularly useful for screening a panel of chemicals that represent environmental hazards and neurotoxicity, including pesticides, brominated compounds, and organophosphorus flame retardants. Additionally, the electrophysiological dynamics of local neurons were evaluated using a microelectrode array (MEA). The results showed that 57% of the tested chemicals exhibited neurotoxic effects. Furthermore, concentration-response profiling allowed for the ranking of medicines based on their neurotoxicity potential. By incorporating both *in vivo* human responses and *in vitro* toxicity data, industrial chemicals were also ranked in terms of their potential health and environmental risks. This study underscores the importance of utilizing iPSC models for toxicity assessment during the development of novel medications and the evaluation of chemicals that may pose risks to human health and the environment.

1.6 Current challenges, motivations, and objectives

The nervous system is a complicated network of specialised cells that transmit various signals to guide physiological activities [135]. The complex physiological structure and harsh microenvironment of the nervous system pose significant challenges to its repair.

Furthermore, the nervous system has intrinsic limitations regarding regeneration and self-healing [136]. Whilst peripheral nervous system (PNS) has a certain ability to regenerate, the regeneration of damaged CNS has been almost impossible [137]. Our understanding of neuroscience and neural development is also minimal because of the difficulty of collecting samples of brain tissue at important developmental time periods.

Nerve tissue is the softest tissue, and nerve cells live in a highly interactive and dynamic niche. Understanding how the microenvironment regulates neural behaviour and function has important implications for biomedical research and nerve regeneration applications. However, reconstructing a 3D biomimetic environment for *in vitro* studies remains challenging owing to the lack of appropriate soft elastic substrates.

To meet these challenges, the following projects were designed as concrete objectives:

Specific objectives of Project 1:

(1) To develop a variety of soft and elastic hydrogel systems to mimic soft nerve tissue environment.

(2) To investigate the effects of matrix stiffness on neuronal differentiation.

(3) To investigate the effects of mechanical stimulation (i.e. stretching) on neuronal differentiation in 3D environments.

Specific objectives of Project 2:

(1) To develop a conductive hydrogel to mimic the electric signals of the neural system.

(2) To investigate the effects of ES on neural behaviour.

(3) To investigate the effects of co-stimulation (mechanical and electrical stimulation) on neural behaviour.

Specific objectives of Project 3:

(1) To develop a novel host-guest hydrogel bio-ink for constructing neural tissue mimics (NTMs) via bioprinting.

(2) To study the electroactivity of 3D-printed NTMs.

(3) To study the effects of host-guest interactions (to mimic a dynamic ECM environment) on cell behaviour.

Chapter 2 Mechanical stimulation on 3D GelMA-PEGDA hydrogel for neuronal differentiation

2.1 Introduction

NSC must differentiate into suitable neural lineages for nerve regeneration and neurogenesis studies [138]. Among different factors affecting NSC differentiation, the mechanical microenvironment is one of the key elements, where differentiation is guided by matrix stiffness and mechanical stimuli, such as stretching [139, 140]. However, the lack of relevant knowledge hinders the development of possible innovative neural therapies, such as the transplantation of NSC [141], and differentiation must occur under ideal mechanical circumstances to reduce tumorigenic results [142]. Therefore, multiple studies have investigated the influence of mechanical stimulation on neuronal development [143] using material topography and structure [144, 145], stiffness [146, 147], or mechanical stretching of material [148]. However, the bulk of these experiments have focused on standard 2D substrates - rather than having a third dimension - with insufficient softness and elasticity, which does not adequately mimic *in vivo* conditions, providing less insight into the underlying mechanisms.

It is well known that nervous tissue is the softest tissue [36, 37]. The brain moduli are reportedly around 1-4 kPa [149-155], while the moduli of the spinal cord range from 0.50 to 6.63 kPa [156-158]. To meet the above research gaps, we prepared a series of

hybrid hydrogels to mimic the soft environment of nerve tissue for 3D cell encapsulation via incorporating high molecular weight PEGDA into GelMA, where the former polymer is for soft elasticity, and the latter is for cell adhesion. While PEGDA and GelMA have different origins (synthetic vs natural), structures, and physical and chemical properties, both have been used in 3D cell encapsulation and stem cell transplantation [159-168]. As the main component of extracellular matrices, GelMA has an abundance of cell-adhesive peptides and excellent biocompatibility for cell growth, proliferation, and differentiation [169]. Conversely, PEGDA lacks cell-adhesive peptides but has an exceptionally flexible linear and long-chain chemical structure. Changing the ratio of PEGDA and GelMA, a series of hybrid hydrogels were developed to mimic neural tissue.

Through GelMA-PEGDA hydrogels, three significant aspects of NSC differentiation could be investigated. First, the hybrid hydrogels provide a highly biocompatible, soft, and elastic 3D environment for NSC encapsulation and growth. By manipulating the concentrations of PEGDA and GelMA, biomimetic hydrogels were engineered with a wide range of compressive moduli (0.8 kPa to 10 kPa) to elucidate the impact of matrix stiffness on the process of neuronal differentiation. Secondly, to mimic the dynamics of the neural microenvironment at the cellular and tissue level, stretching was further applied to NSC encapsulated in hybrid hydrogel to investigate the influence of mechanical stimulation on NSC differentiation in a 3D matrix.

2.2 Methodology

2.2.1 Synthesis of GelMA and PEGDA

Methacrylate anhydride (MA, Sigma-Aldrich) was covalently immobilised on type A gelatin through an amide reaction [164, 170]. First, 300 mg of gelatin was solubilized in 30 mL phosphate buffer solution (PBS, HyClone, pH=7.4) at 50 °C. Then 0.03 mL MA was dripped into the above solution while stirring at 500 rpm. The reaction was conducted at 50 °C for 2 h. After that, the solution was subjected to filtration and dialysed in DI water for 7 days and then freeze-dried. As indicated in the literature, ^{1}H-NMR spectroscopy (JEOL ECZ500R 500 MHz) was used to evaluate the degree of substitution (DS) of the resultant GelMA [164, 170].

The carboxyl group of acryloyl chloride (Sigma-Aldrich) was reacted with the hydroxyl group of PEG (20 kDa, Sigma-Aldrich) to produce PEGDA [171]. After stirring for 30 min, 10% PEG was dissolved in dichloromethane. The solution was then added gradually to acryloyl chloride and triethylamine (Sigma-Aldrich). PEG, triethylamine, and acryloyl were combined in a 1:4:4 molar ratio. The materials were combined overnight while being protected by N_2. After the reaction, ether was used to precipitate the by-product. After further purification via rotary evaporation and dialysis, the product was freeze-dried to eliminate any leftover contaminants. In addition, ^{1}H-NMR gave further evidence of PEGDA structure.

Different amounts of GelMA and PEGDA polymer were dissolved in 0.5 wt% photo-initiator, lithium phenyl-2,4,6-trimethyl-benzoyl phosphonate (LAP, Sigma-Aldrich), to prepare hybrid hydrogels. For photo-crosslinking, the above mixture was exposed to an intensity of 6.9 mW/cm^2 (360–480 nm, UV light) for 20 s.

2.2.2 The characterisation of physical and chemical properties of hydrogels

2.2.2.1 Mechanical tests

The mechanical properties of hybrid hydrogels were conducted using a dynamic universal mechanic system (Instron, US). For the tensile tests, dumbbell-shaped hydrogel samples (L=15mm, W=2mm, T=1.5mm) were prepared, while cylindrical samples (d=10mm, h=5mm) were prepared for the compression test. Meanwhile, as performed before, specimens were immediately reloaded following initial loading-unloading during the cyclic tensile test [172, 173]. The specimens (L=15mm, W=2mm, and T=1.5mm) were stretched by 50% of their original length 100 times. The established protocol dictated that all examinations be conducted using a consistent rate of 0.5 mm/min. Compressive and tensile moduli were derived by fitting linear regressions to the stress-strain curves in the deformation range of 0 to 10% [170].

2.2.2.2 Swelling experiment

Cylindrical specimens (d=10 mm, h=3 mm) were subjected to a swelling test at room

temperature to determine the impact of crosslinking on hydrogel [170]. The hydrogel samples were immersed in PBS for different periods, and the swelling capacity of the hydrogels was calculated by **Eq. (2.1)**.

$$\text{Swelling} = \left(\frac{W_s - W_i}{W_i}\right) \times 100\% \quad \textbf{(2.1)}$$

where W_i is the initial hydrogel weight before being immersed in PBS, whereas W_i is the wet hydrogel weight after being immersed in PBS for a certain period.

2.2.2.3 Viscosity test

Viscosity was tested through a rheometer (MCR 702) on a parallel plate (25mm in diameter) with a temperature control system set at 37°C. The shear rate ranged from 0.1 s^{-1} to 1000 s^{-1}.

2.2.2.4 Degradation of hydrogel

Different columnar hydrogels (d=10 mm, h=3 mm) were first immersed in DI water for 12 h to reach swelling equilibrium. Subsequently, the swollen hydrogels were immersed in collagenase type II solution (Sigma-Aldrich, 0.2 U/mL) at 37°C [174].

At predefined time intervals, hydrogel specimens were extracted from the collagenase solution and subjected to precise weighing procedures. The degrading characteristics of hydrogels were determined using **Eq. (2.2)** [175].

$$\text{Mass remaining (\%)} = \left(\frac{W_t}{W_0}\right) \times 100\% \quad \textbf{(2.2)}$$

where W_0 is the initial mass after equilibrium swelling, and W_t is the mass remaining after collagenase degradation at various times.

2.2.3 Cell culture and differentiation

2.2.3.1 Cell culture

N2a (ATCC, USA) cells were used in this chapter. They have been used extensively for research on neuronal development, axon growth, and signalling pathways, and has been shown to maintain stem cell properties while being capable of differentiating into neurons and glial cells [176]. Despite being derived from tumour tissues, several studies have indicated that the original cells are not superior to human cell line models. Furthermore, the use of the N2a cell line offers high reproducibility, thereby facilitating comparisons of results across different studies. As previously reported, N2a cells were cultured in a full medium (Dulbecco's Modified Eagle Medium (DMEM) and 10% fetal bovine serum (FBS)). The culture medium was replaced bi-daily during the course of cultivation.

2.2.3.2 Cell differentiation

For the differentiation of N2a, retinoic acid (RA, LOKCO Technology) was used to stimulate neurite outgrowth and differentiation. N2a cells were cultured in different RA concentrations (0μM, 10μM, 25μM, 50μM) to deduce the optimum concentration for

the differentiation medium [19]. Cell morphology and differentiation were determined under a microscope after 48 h of culture.

2.2.4 Cell culture and differentiation on 2D hydrogels

The GelMA-PEGDA solution containing 0.5 wt% photo-initiator underwent filtration using a 0.22-μm membrane to sterilise before cell culture. After pipetting 150 mL of hydrogel into each well of a 12-well plate, the whole plate was incubated at 37°C for 10 min, allowing for homogenous distribution of the hydrogel across all wells. The hydrogel was subjected to 6.9 mW/cm^2 of UV radiation for 20 s of photo-crosslinking (360–480 nm). After photo-crosslinking of the hydrogel, 0.5 mL of N2a suspensions (1×10^5 cells/mL) were seeded on the top hydrogel. The cells were given a whole night to adhere to the hydrogel. N2a cells were differentiated using a differentiation medium of 99% DMEM, 1% FBS, and 10μM RA.

2.2.5 Cell encapsulation and 3D stretching hydrogel system

To prepare the 3D stretching system, N2a cells were encapsulated in hydrogel precursor at a density of 1×10^6 cells/mL. Then 10 μL of the cell-loaded hydrogel solution dripped onto plasma-treated rubber bands, which were subsequently cross-linked by UV. To achieve different stretching proportions, we used a glass cutter to make three different lengths of glass for each ratio (i.e., 24 mm for the initial length; 30 mm for 25% stretch;

and 36 mm for 50% stretch). The plasma-treated rubber bands were tied and fixed onto glass slides of initial length, and 10 μL of the cell-loaded hydrogel suspension was dripped onto the rubber bands. After photo-crosslinking of the hydrogel, the rubber bands were stretched at a certain ratio, and the hydrogel was stretched accordingly with the rubber bands and maintain the stretching ratio of either 25% or 50% by fixing to a specific length of glass slides. A schematic of a stretched cell-laden hydrogel system for neuronal differentiation is shown in **Schematic 2.1**.

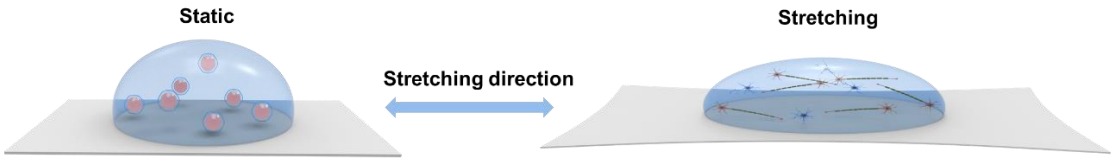

Schematic 2.1 A stretching cell-laden hydrogel system for neuronal differentiation.

2.2.6 Cell viability and proliferation

The viability of N2a cells was evaluated using live/dead staining, followed by quantitative analysis using Fiji software to determine the percentage of viable and non-viable cells. The proliferation of N2a cells at different time points during cultivation was assessed using the Cell Counting Kit-8 (CCK-8) assay. A control group was established, consisting of N2a cells cultured on tissue culture polystyrene (TCP) in a 12-well plate.

2.2.7 Cell morphology

The cytoskeleton with phalloidin and the nucleus with DAPI were stained to examine the cell morphology. Samples were first treated with paraformaldehyde for fixation. After 20 min of permeabilisation with 0.1% Triton X-100, the cells were then blocked for 45 min with 1% bovine serum albumin (BSA). Next, the samples were incubated in phalloidin solution coated with Alexa Fluor 488 (1:1000 dilution; Thermo Fisher, Hong Kong) for 45 min, and then DAPI solution (1:1000 dilution; Thermo Fisher, Hong Kong) for another 5 min in the dark. Specimens were examined using fluorescence microscopy (Nikon, Japan) after being rinsed three times with PBS.

2.2.8 Immunocytochemistry and gene expression

2.2.8.1 Immunocytochemistry

Antibody labelling validated neural stem cell differentiation. First, the hydrogel samples were treated for 20 min in paraformaldehyde. After implementing the permeabilization and blocking protocols as detailed in section 2.27, samples were treated overnight with two primary antibodies (rabbit anti-GFAP and mouse anti-Tubulin 3, 1:1000 in primary antibody diluent) at 4°C. Following the binding of the primary antibody, the samples were incubated in the dark at 37°C for 2 h alongside Goat pAb to Ms 594 Red conjugated 1:1000 and Goat pAb to Rb 488 FITC-conjugated 1:1000 as the antibodies (Abcam, UK). Finally, the DAPI solution was stained for another 5min. Then, the samples were inspected by confocal microscopy after three rounds of PBS washing (ZEISS LSM 900).

Olympus inverted microscope (Nikon, Japan) and confocal microscope pictures were used to quantify morphological features (ZEISS LSM 900). The Fiji package in ImageJ was used to analyse all the photos. In addition, Fiji's NeuronJ plugin was used to measure average neurite length [177].

2.2.8.2 Gene expression

According to the literature, reverse transcription quantitative polymerase chain reaction (RT-qPCR) was utilized as quantitative gene expression [178]. Cells grown on 2D hydrogel were harvested using trypsinisation after various incubation periods. Collagenase type II (Thermo Fisher, Hong Kong) was used to break down and liberate the 3D cells encapsulated in hydrogels. Using a Total RNA Kit (Omega, Hong Kong), total RNA was isolated from N2a cells. a Prime Script RT Master Mix Kit (Takarabio, Hong Kong) was used to reverse-transcribe the extraction into cDNA. As an internal control, GAPDH was employed to standardize the findings. **Table 2.1** lists the sense and antisense primer sequences for a group of related genes. The $2^{-\Delta\Delta Ct}$ technique was used to determine gene expression.

Table 2.1 The primer sequences used for RT-qPCR

Genes	Sequences
Nestin	F: 5'-AAGTTCCCAGGCTTCTCTTG-3' R: 5'-GTCTCAAGGGTATTAGGCAAGG-3'
GFAP	F: 5'-GCTGGAGGGCGAAGAAAAC-3' R: 5'-GCCTTCTGACACGGATTTGG-3'

Tuj-1	F: 5'-ACCCCGTGGGCTCAAAAT-3' R: 5'-CCGGAACATGGCTGTGAACT-3'
MAP2	F: 5'-CCTGGTGCCCAGTGAGAAGA-3' R: 5'-GTCCGGCAGTGGTTGGTTAA-3'
GAPDH	F: 5'- GCTGGAGGGCGAAGAAAAC-3' R: 5'-GCCTTCTGACACGGATTTGG-3'

2.3 Results and discussion

2.3.1 Physicochemical characterisation of hydrogels

2.3.1.1 Chemical properties of hydrogels

In the ^{1}H-NMR spectrum of GelMA (**Figure 2.1A**), a vinyl group at 5.64 and 5.36 ppm revealed that MA was grafted onto gelatin. In addition, the modification of MA on gelatin could also be confirmed by a significant methyl peak increase (1.9 ppm) followed by a decrease in the proton peak of lysine methylene (2.9 ppm). We found the DS as 90% upon utilising peak area changes at 2.9 ppm on GelMA and gelatin (**Eq. 2.3**) [170].

$$\mathrm{DS} = \left(1 - \frac{I_1}{I_2}\right) \times 100\% \quad (\mathbf{2.3})$$

I_1 is lysine methylene's integrated area on GelMA, while I_2 is on gelatin.

Similarly, PEGDA synthesis was also confirmed by 1H NMR. By comparing the spectra of PEG and PEGDA, the characteristic peaks of the acrylate group (5.8, 6.1, and 6.4 ppm) were presented on PEGDA (**Figure 2.1B)**, confirming the successful synthesis of PEGDA. The ether groups (-CH_2OCO-) in the chemical structure of PEGDA were found at around 4.3 ppm [179, 180].

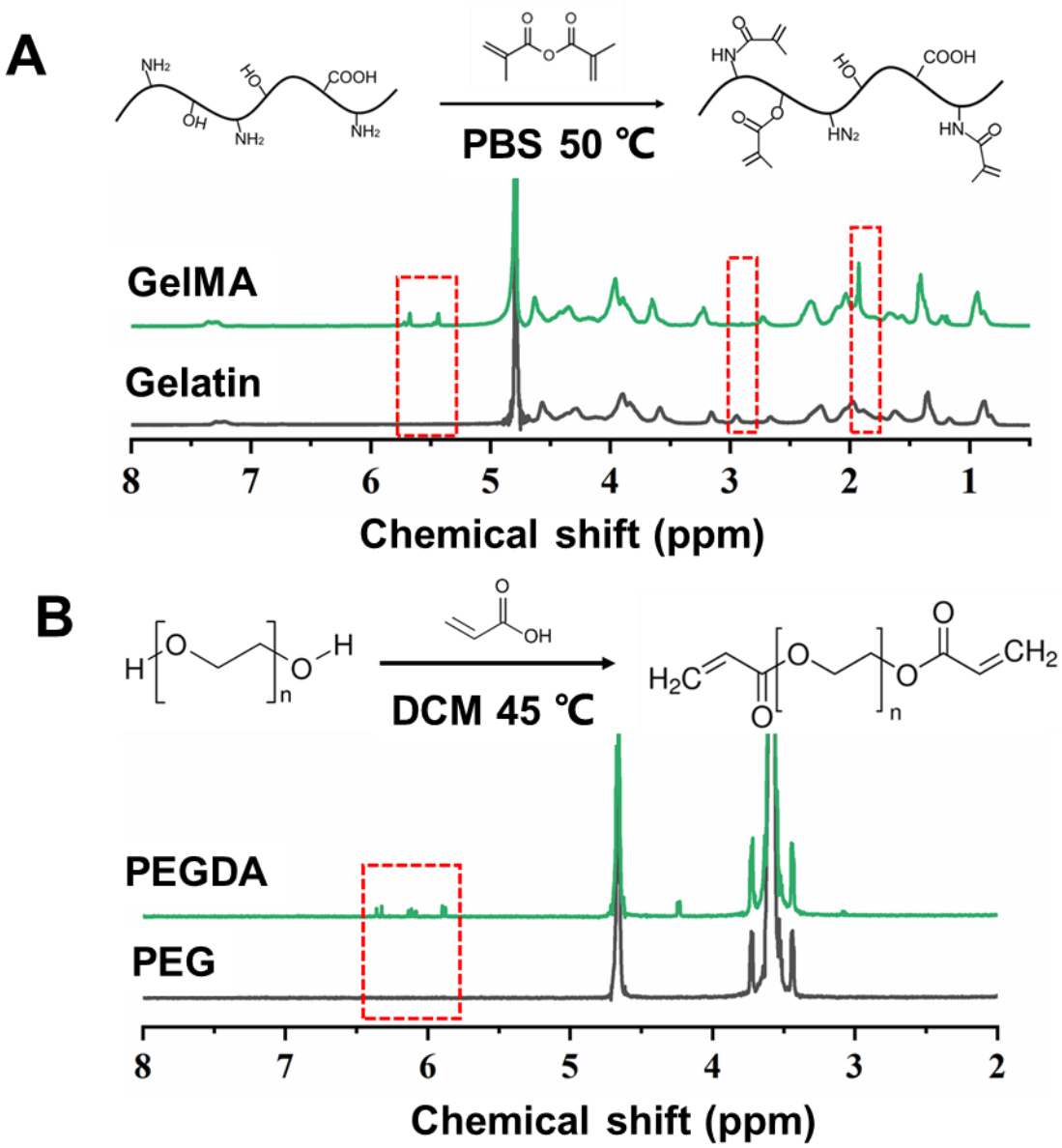

Figure 2.1 (A) Scheme of the chemical reaction and ^{1}H-NMR result of GelMA. **(B)** Scheme of the chemical reaction and ^{1}H-NMR result of PEGDA.

2.3.1.2 Mechanical and swelling characterisation of hydrogels

Because NSC differentiation and proliferation substantially impacted mechanical attributes, designing hydrogels of varied compositions and mechanical attributes was paramount (**Figure 2.2A-E**). The annotations for the three distinct compositions were:

for 2.5 wt% GelMA + 2.5 wt% PEGDA, G:P=2.5:2.5; for 4 wt% GelMA + 1 wt% PEGDA, G:P=4:1; for 5 wt% GelMA, G. At mild stress, all hydrogels exhibited normal linear elasticity. **Figure 2.2C** demonstrates that adding PEGDA may considerably enhance elongation at break. G:P=2.5:2.5 exhibited the greatest elongation (1.8 times), then G:P=4:1 (approximately 1.5 times), and lastly, G (approximately 0.6 times). With increasing PEGDA ratio, tensile modulus and stress (**Figure 2.2A-B**) of the composite hydrogels reduced to roughly 10 kPa (G:P=2.5:2.5) from around 60 kPa (5 wt% GelMA). Meanwhile, the compression stress and modulus (**Figure 2.2D-E**) reduced to 0.8 kPa (G:P=2.5:2.5) from approximately 6 kPa (5 wt% GelMA). It was reported that neuronal development is normally advantageous in stiffness between 1 and 10 kPa; therefore, our hydrogels provide a mimic neural microenvironment for investigating the influences of matrix stiffness on neuronal differentiation [38].

In addition, **Figure 2.2F** shows hydrogel crosslinking capacity, which indicates swelling behaviour and substantially impacts mechanical characteristics. After 9 h of soaking in PBS, the swelling reached its equilibrium. As PEGDA concentration grew, so did the swelling ratio, with GelMA having the lowest swelling ratio (approximately 8%) followed by G:P=4:1 (about 23%) and G:P=2.5:2.5 having the greatest (about 80%). These results corroborated our prediction that the insertion of PEGDA with a high molecular weight may vary hydrogel stiffness, elongation, and swelling by increasing chain flexibility and altering the cross-linked network topology [181-183].

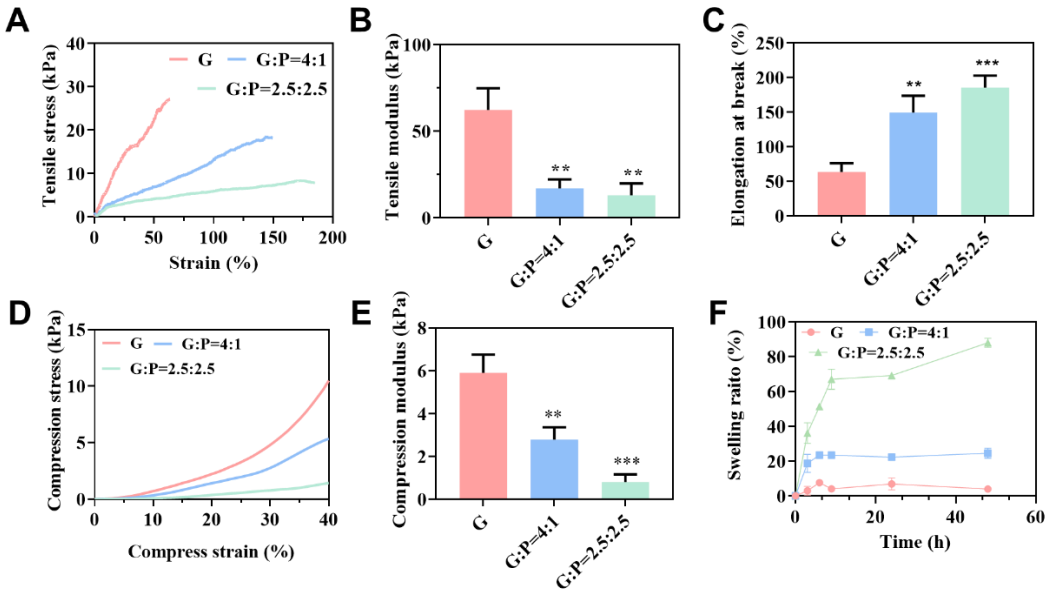

Figure 2.2 Mechanical and swelling results for GelMA-PEGDA hydrogels. **(A-B)** Tensile properties of the hydrogels. **(D-E)** Compression properties of the hydrogels. **(C, F)** Elongation at break and swelling properties of the hydrogels.

The samples of hydrogel were subsequently put through a cyclic tensile test. **Figure 2.3** illustrates the average stress versus strain curves on the first, tenth, and 100th cycles. After 100 loading-unloading cycles, all hydrogels displayed outstanding tensile recoverability, demonstrating that the hydrogels were exceedingly stretchy. As a viscoelasticity attribute, hysteresis was likewise seen from the cyclic tensile curves [172, 184]. A hysteresis loop exhibiting minor residual strain was found between the first two runs upon repeatedly stretching the hydrogels to identical strains. Meanwhile, hysteresis achieved stability alongside significantly decreased significance between the tenth and hundredth cycles. The findings of cyclic tensile testing revealed that all hydrogels were stretchy and recoverable for applications involving stretching stimuli. Compared with pure GelMA hydrogel, incorporating PEGDA dramatically reduced

strength tensile-wise and enhanced hydrogel stretching capacity, which aligns with the mechanical results elucidated in **Figure 2.2**.

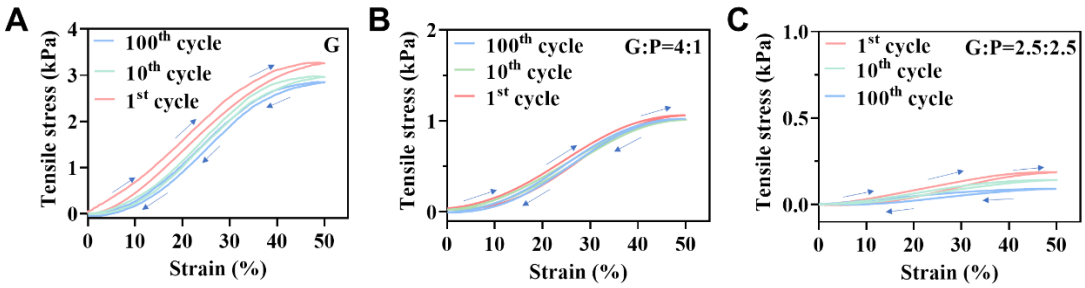

Figure 2.3 The cyclic tensile stress curves of different hydrogels **(A)** G, **(B)** G:P=4:1, and **(C)** G:P=2.5:2.5, respectively.

As with several other mechanical parameters, viscosity may influence cellular activity. Viscosity predominantly affects cell activity by reorganising the structural configuration [185, 186]. A rheometer was used to measure hydrogel viscosity with varying components at 37°C (MCR 702) with shear rates from 0.1 s^{-1} to 1000 s^{-1} (**Figure 2.4**) and investigate if GelMA-PEGDA viscosity was acceptable for the encapsulation, development, and differentiation of NSC. All the hydrogels had equivalent shear-thinning capabilities (**Figure 2.4A**). Meanwhile, with the increase in the proportion of PEGDA, there was a slight decrease in viscosity from 6.8 mPa·s to 4.7 mPa·s (**Figure 2.4B**), which is similar to the viscosity of ECM-derived hydrogels that have been shown to support cell survival [187].

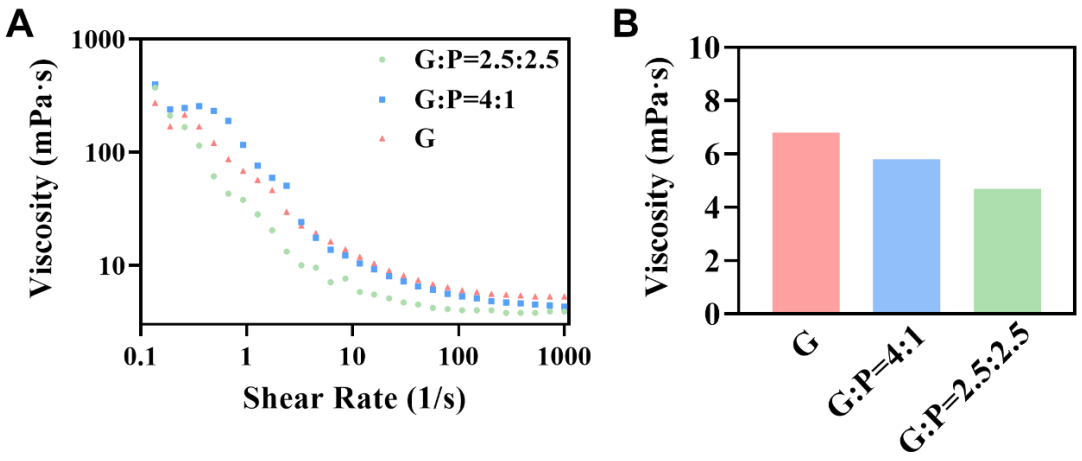

Figure 2.4 (A) The continuous flow test (viscosity-shear curves) with a rotational rheometer at 37°C. **(B)** The viscosity of hydrogels at a specific shear rate.

The breakdown of several hydrogels in collagenase solution is shown in **Figure 2.5**. Hydrogels with a higher PEGDA content disintegrated more quickly than 100% GelMA hydrogels; complete degradation happened in 80 h for G, 70 h for G:P=4:1 and 50 h for G:P=2.5:2.5. Conventional PEGDA hydrogels are often vulnerable to gradual deterioration [188]. Nevertheless, owing to larger hydrolysable ester ratios and reduced crosslinking density, the low concentration and high molecular weight of PEGDA hydrogel may expedite hydrolysis substantially [189]. Enzymatic GelMA network degradation increased PEGDA hydrolysis, leading to fast GelMA-PEGDA decomposition. The poor crosslinking network decreased the breakdown period, and gave flexible and soft qualities to the hydrogel, allowing mechanical stimulation and cell survival.

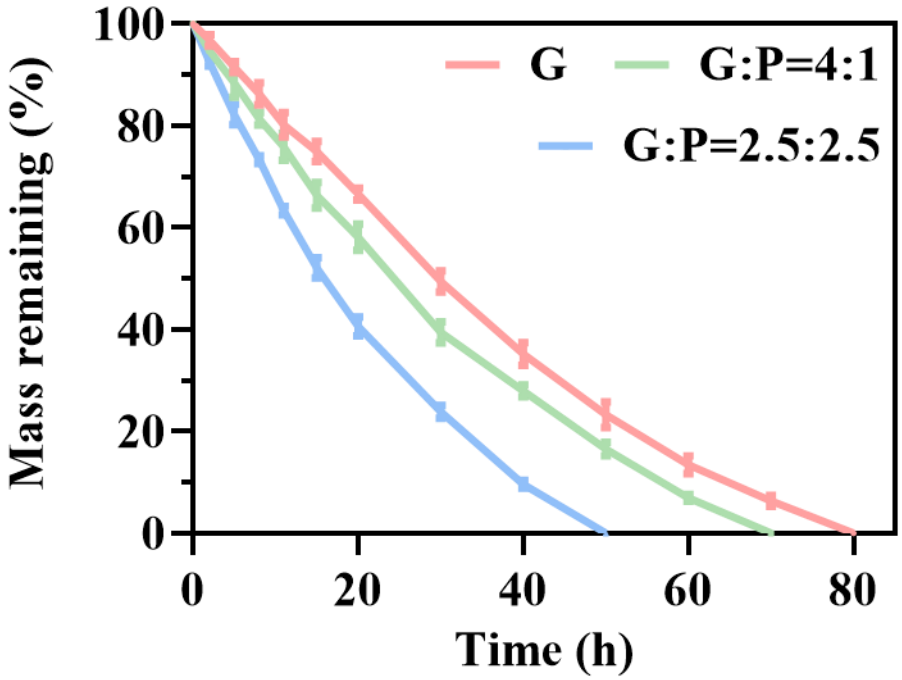

Figure 2.5 Percentage of mass remaining showing the effect of hydrogel composition on degradation (mean ± SD, n = 3) incubated in collagenase type II solution.

Besides, we monitored the changes in hydrogel modulus during the 3D cell encapsulation process by examining the modulus changes in the culture medium over a span of 7 days. **Figure 2.6A** illustrates the swelling ratio of the hydrogels in the culture medium. The addition of PEGDA resulted in an increased swelling ratio of the hydrogels, with GelMA exhibiting approximately 8% swelling, followed by G: P= 4:1 (slightly higher than GelMA, around 20%), and G: P=2.5:2.5 displaying the highest swelling ratio (reaching 80%). This outcome aligns with our hypothesis that the incorporation of PEGDA can modulate hydrogel swelling by enhancing chain flexibility and altering the cross-linked network topology. **Figure 2.6B** presents the moduli of the hydrogels incubated in DMEM solution for 7 days. As depicted in **Figure**

2.6B, the addition of PEGDA significantly reduced the compression modulus of the hydrogels. The compression modulus decreased to 1.0 kPa (G: P=2.5:2.5) from approximately 7.0 kPa (GelMA), which is consistent with our previous findings. Throughout the 7-day period, the compression modulus of the hydrogels remained relatively stable, with a slight initial decrease on the first day due to hydrogel swelling. The stable mechanical structure of the hydrogels provides a foundation for our subsequent investigation of the mechanical properties during neural differentiation.

Additionally, we employed enzymatic degradation to accelerate the breakdown of the hydrogels and monitored the changes in modulus during the degradation process. Hydrogels with higher PEGDA content exhibited faster degradation compared to GelMA hydrogel. As shown in the line chart, G: P=2.5:2.5 completely degraded by day 3, followed by G: P=4:1 (retaining approximately 13% mass at day 3), while GelMA exhibited the slowest degradation (with approximately 30% mass remaining at day 3). The introduction of low-concentration and high molecular weight PEGDA resulted in a higher hydrolyzable ester ratio and reduced crosslinking density, thereby expediting hydrolysis [188, 189]. The enzymatic degradation of the GelMA network increased PEGDA hydrolysis, leading to rapid decomposition of GelMA-PEGDA composite hydrogel. The decreased crosslinking network shortened the degradation period, imparting flexibility and softness to the hydrogel, which is essential for mechanical stimulation and cell viability. Furthermore, all three hydrogels showed a significant decline in compression modulus under collagenase degradation, with GelMA exhibiting

the greatest reduction (up to 3.6 kPa), followed by G: P=4:1 (approximately 2.27 kPa), and finally G: P=2.5:2.5 (1.1 kPa). During this period, the relative magnitude of the compression modulus of the three hydrogels remained consistent with the trend observed in **Figure 2.6D**, indicating that enzymatic degradation did not alter the relative compression modulus among these hydrogels.

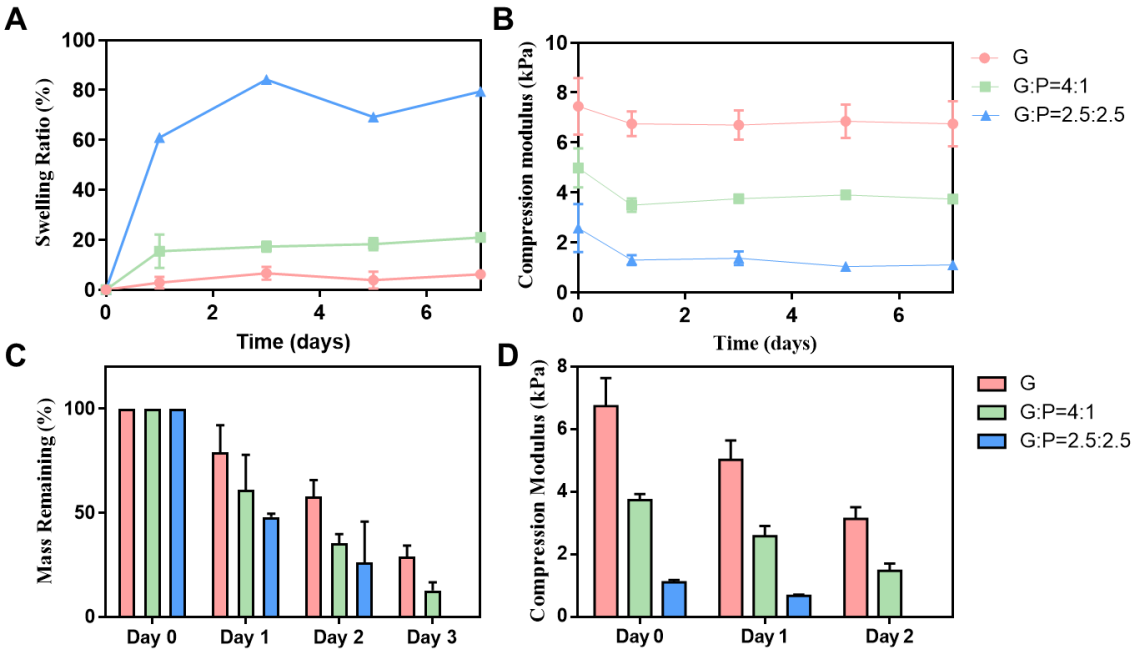

Figure 2.6 (A) Swelling properties of the hydrogels in DMEM. **(B)** Compression modulus of the hydrogels incubated in DMEM solution within 7 days. **(C)** Degradation properties of the hydrogels in 0.2 U/mL collagenase type II solution. **(D)** Compression modulus of the hydrogels incubated in collagenase within 2 days.

2.3.2 Cell differentiation with retinoic acid

N2a cells were maintained in a differentiation medium for 48 h in different retinoic acid

concentrations. Cell morphology was used to evaluate neuronal differentiation. As shown in **Figure 2.7**, more differentiated cells with dendrites and axons were observed in the RA-treated groups. The longest neuronal outgrowth (76μm) and highest cell differentiation rates (36%) were observed in 10μM RA group. On the other hand, lower cell differentiation rates and viability were detected at higher RA concentrations (50μM). Such findings were probably because a low RA concentration induces cell differentiation by EGF signalling, while a high dose of RA inhibits cell viability by decreasing ERK1 activation [19]. Therefore, 10μM RA was used to induce cell differentiation in succeeding experiments.

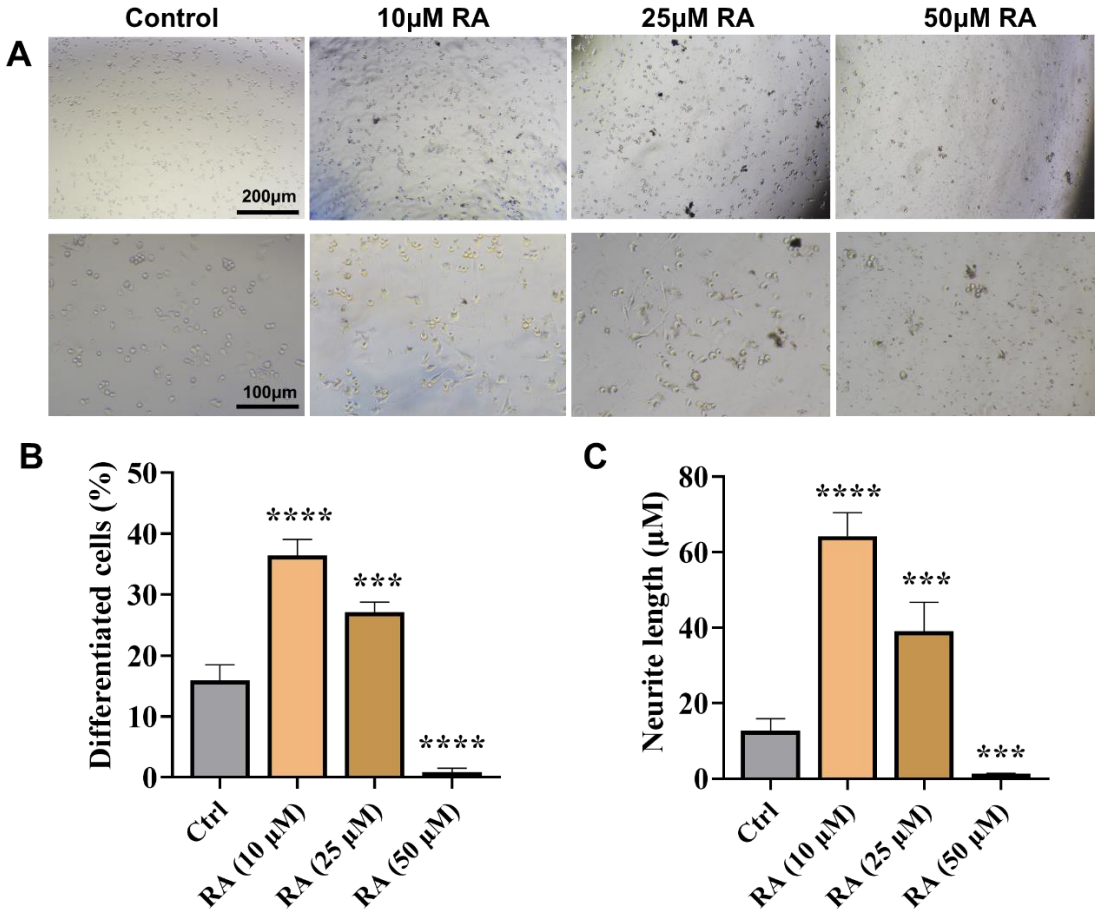

Figure 2.7 N2a cells treated with various retinoic acid concentrations. **(A)** The morphology of N2a cells after being cultured for 48 h in DMEM medium with 1% FBS.

(B) Quantification of differentiated cells induced by different RA concentration. **(C)** The quantitative neurite outgrowth induced by different RA concentration.

2.3.3 Cell viability and proliferation on 2D hydrogels

N2a cell proliferation and viability on 2D hydrogels were examined for validating GelMA-PEGDA in neural tissues. The assessment of cell viability on hydrogels was performed by employing live/dead staining. For the control, N2a cells were grown on a 12-well plate. **Figures 2.8A** and **2.8Ci** showed that the cells were extremely viable, and no substantial cytotoxicity was seen. After 1 and 5 days of cultivation, 90% of the cells remained alive. As with the control samples, the N2a cells were evenly distributed on the hydrogels, demonstrating high cytocompatibility.

To investigate N2a cell morphology on the hydrogels, we used phalloidin/DAPI for staining actin filaments green and N2a cell nuclei blue (**Figure 2.8B**). On the first day, N2a cells were round and equally dispersed. Five days after full-growth media incubation, the cell population rose dramatically, although the majority remained undifferentiated and round.

CCK-8 assessed the proliferation of N2a cells (**Figure 2.8Cii**). Control expanded quickest after 5 days of culture ($p \leq 0.001$), followed by G and G:P=4:1. However, G:P=2.5:2.5 had the least proliferation, perhaps owing to the high PEGDA ratio, which

lacked RGD peptides and other biological ligands for cellular adhesion and proliferation [190].

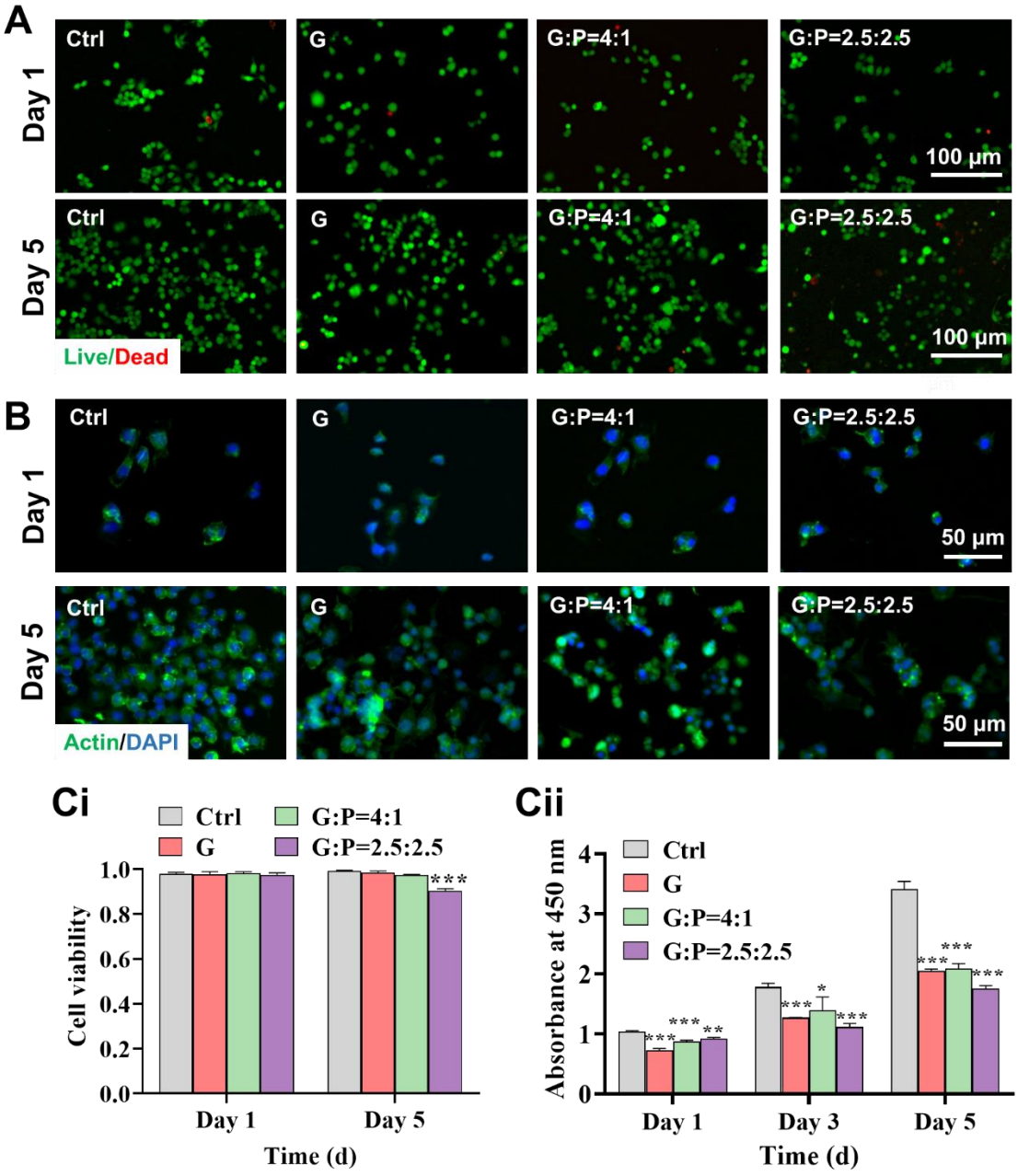

Figure 2.8 The viability and proliferation of N2a cells on hydrogels. **(A)** Live/dead staining of different groups. **(B)** Cell morphology of different groups on day 1 and day 5 stained by phalloidin and DAPI. **(Ci-ii)** The quantification of cell viability and proliferation in different groups at different times.

2.3.4 Impact of UV on cell viability

The impact of UV radiation on cell viability within GelMA hydrogel was investigated in this study, as GelMA hydrogel served as the primary hydrogel throughout the entire thesis. **Figure 2.9** illustrates the detrimental effects of UV on cells. The viability and proliferation of N2a cells exhibited a decline as the UV energy increased, particularly when the UV energy exceeded 0.24 J/cm^2. It is worth noting that at low UV energy levels (<0.12 J/cm^2), the hydrogel was not fully crosslinked, as evidenced by the 2D morphology of the cells (**Figure 2.9A**). In order to strike a balance between cell viability and hydrogel crosslinking, a UV energy of 0.12 J/cm^2 (equivalent to 20 seconds at a UV intensity of 6.9 mW/cm^2) was chosen for the UV crosslinking process. This energy level ensured that the hydrogel achieved proper crosslinking while minimizing cell damage.

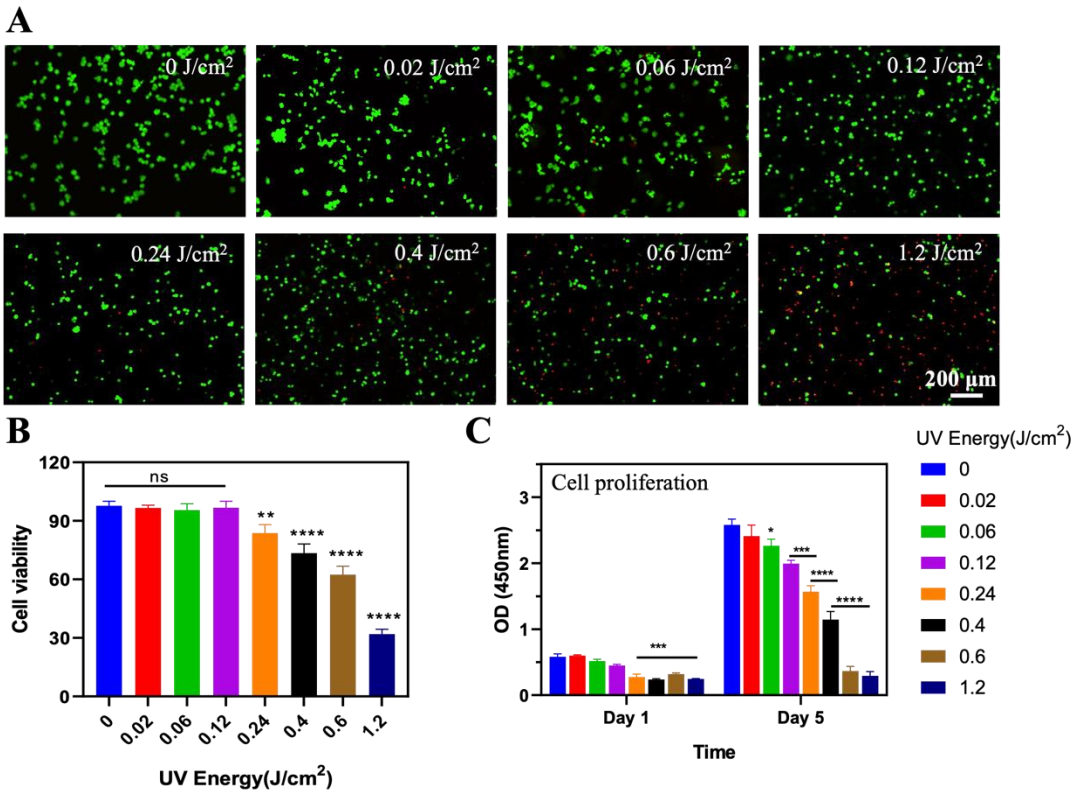

Figure 2.9 The effect of UV on N2a cell viability in 5% GelMA hydrogel. **(A)** Live/dead staining images **(B)** Cell viability obtained from the quantitative analysis of live/dead staining images **(C)** Cell proliferation in different UV Energy by CCK-8.

2.3.5 Effect of stretching on cell viability

With the increase in stretching ratio, cell viability decreased to varying degrees among all groups, indicating that stretching indeed affects cell viability (**Figure 2.10**). Notably, among groups subjected to the same stretching ratio, the GelMA groups displayed the most pronounced influence on cell viability. Specifically, as the stretching ratio increased from 0% to 50%, cell viability decreased significantly from 99% to 75% (**Figure 2.10C**). This observation can be rationalized by the relatively higher modulus

of GelMA hydrogel, which generates greater mechanical stress during the stretching process (approximately 6 kPa), consequently resulting in a more substantial reduction in cell viability. Conversely, the impact of stretching on cells within the GP hydrogel group was comparatively minimal due to the lower levels of mechanical stress exerted (approximately 3 kPa). In fact, at a stretching ratio of 50%, cell viability remained relatively high at 86% (**Figure 2.10C**). This finding suggests that the cells within the GP hydrogel experienced less strain and maintained their viability to a greater extent. Following a five-day culture period, the cells in all groups exhibited relatively high viability, meeting the requirements set forth by the research objectives involving stretching (**Figure 2.10D**). Moreover, a comparison between the initial and subsequent days revealed a consistent trend in cell viability, accompanied by noticeable cellular proliferation. These findings collectively affirm the feasibility of our stretching method and its potential for promoting cell proliferation within the experimental system.

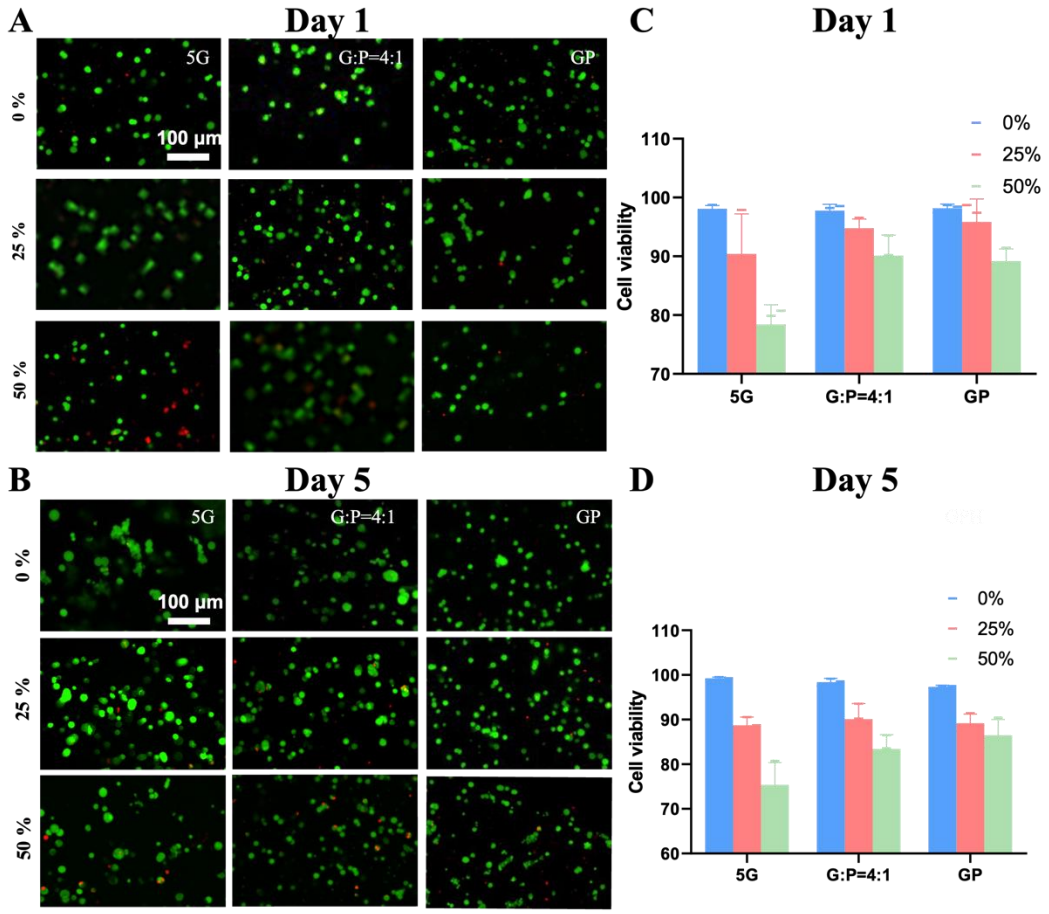

Figure 2.10 The effect of stretching (stretching ratio=0%, 25%, 50%) on N2a cell viability. **(A, B)**. Cell viability determined by Live/dead staining after 1, 5 days (Green: live cells; red: dead cells) **(C, D)**. Quantification from the live/dead assay via ImageJ software. (5G: 5% GelMA, G:P=4:1 4%GelMA+1% PEGDA, GP=2.5%GelMA+2.5%PEGDA)

2.3.6 Neuronal differentiation on 2D hydrogels

Following the determination of hydrogel cytocompatibility, neuronal differentiation was induced on 2D hydrogels using the differentiation medium. On days 1 and 5, N2a cell morphology pre- and post-differentiation was examined using phalloidin/DAPI

staining. As in prior trials, the control consisted of 12-well plate-grown N2a. On day 1, the spherical cells never spread, as seen in **Figure 2.11A**. For G:P=4:1 and 5 wt% GelMA, lengthy synapses were detected. Cell morphology changed substantially 5 days after incubation in differentiation media, with most cells assuming a spindle-like structure and spreading out entirely. As previously stated, G:P=2.5:2.5 did not disperse compared to others, potentially because of a significant proportion of PEGDA, where there is no biological ligand for cell attachment.

To assess gene expression and cell differentiation, RT-qPCR and immunocytochemical staining were used based on these biomarkers: nestin, Tuj-1, and GFAP [191]. On day 1, N2a cells were round in all groups with no neurite outgrowth, and only a minimal amount of neuronal differentiation protein expression (GFAP, Tuj-1) was detected from immunofluorescence staining (**Figure 2.11B**). On day 5, both the control and hydrogel groups showed significant expression of neuronal differentiation markers along with noticeable neurite growth. The neurite length was then measured by tracing the neurite length of representative neurons using ImageJ **(Figure 2.11Ci)** [192]. The GelMA group had the highest neurite development (154μm), and neurite length dropped to about 30μm with the increase of PEGDA, possibly because of the weakening cell adhesion caused by the absence of RGD peptide. **Figure 2.11Cii-iv** demonstrates that the control group had the lowest nestin expression and the relative nestin expression rose in parallel with the quantity of PEGDA. The relative nestin expression in G:P=2.5:2.5 was doubled when compared to the GelMA group. In contrast to Tuj-1

expression (**Figure 2.11Civ**), GFAP (an astrocyte marker) was considerably greater (2.5-fold) in the stiffer hydrogel group (higher GelMA ratio) (**Figure 2.11B, Figure 2.11Ciii**). These results confirm recent findings [38, 193-195] that a more rigid hydrogel mechanical environment renders NSC marginally more sensitive to astrocyte differentiation. Furthermore, while there was no significant change in neuronal marker expression between G and G:P=4:1, expressions of Tuj-1 and GFAP were reduced in G:P=2.5:2.5, possibly owing to the lack of cell adhesion ability caused by greater PEGDA concentration.

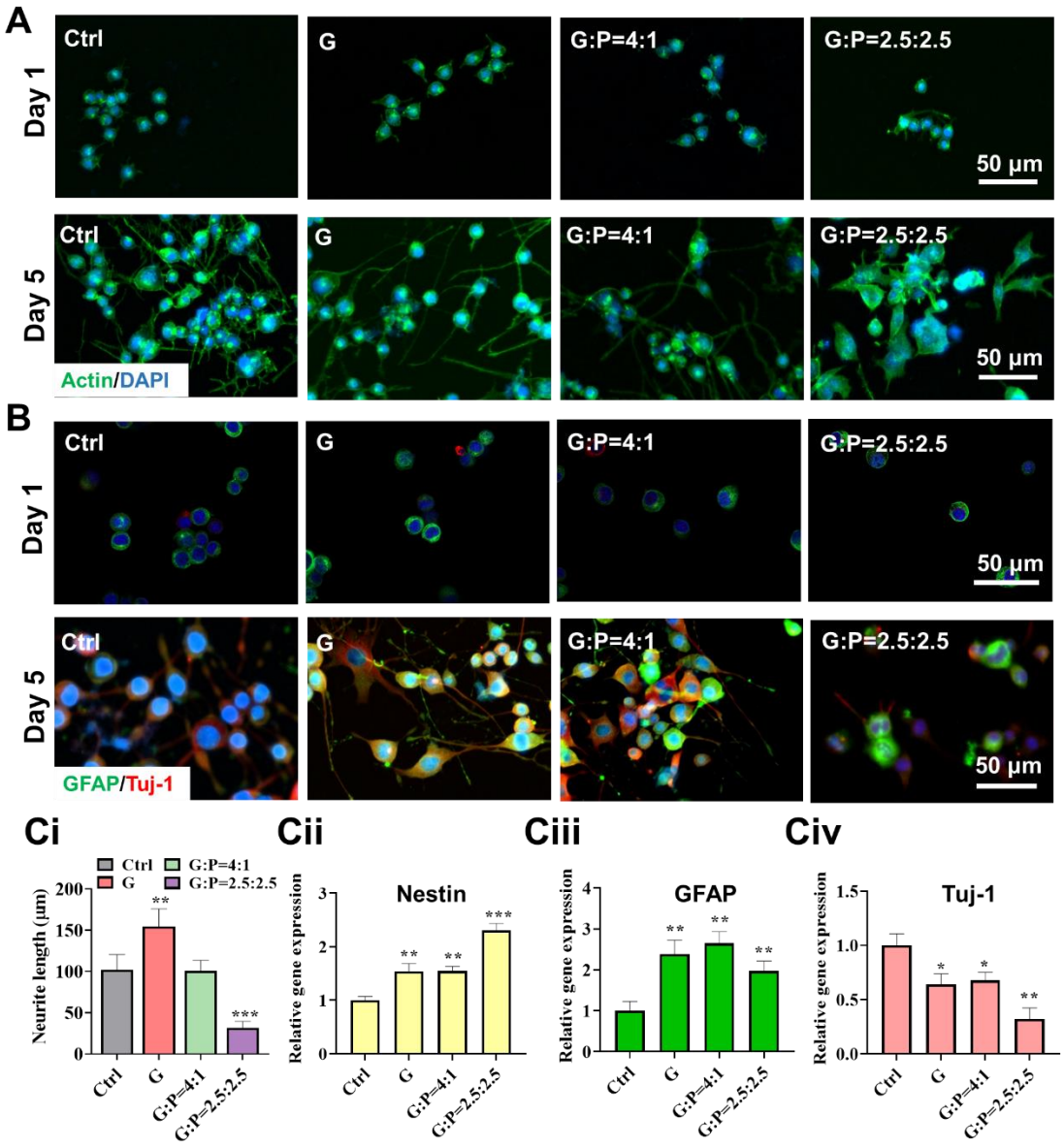

Figure 2.11 The influence of stiffness on neuronal differentiation on 2D hydrogels. **(A)** Cell morphology of different groups stained by phalloidin and DAPI. **(B)** Tuj-1 and GFAP immunofluorescence staining of different groups on days 1 and 5. **(Ci-iv)** The quantitative neurite outgrowth and RT-qPCR evaluation of neural differentiation-related gene expressions on day 5.

2.3.7 The influence of matrix stiffness on neuronal differentiation in 3D hydrogels

After proving the efficacy of 2D hydrogels, the same properties were investigated for 3D hydrogels. Firstly, the viability of cells within 3D hydrogels was assessed using live/dead staining. As depicted in **Figure 2.12Ai**, N2a cells in all hydrogel groups were in good condition, with only a few dead cells observed. After 5 days of cultivation, N2a cells proliferated significantly and formed cell clusters, indicating the favorable biocompatibility of hydrogels for 3D cell encapsulation. The quantitative cell proliferation was evaluated by CCK-8. As seen in **Figure 2.12Aii**, the proliferation of encapsulated N2a cells rose considerably from day 1 to day 5 in all hydrogels. In addition, like the 2D results, the proliferative capacity of N2a cells within the 3D G:P=2.5:2.5 group exhibited a comparatively lower rate in contrast to both the G and G:P=4:1 group. This discrepancy can be attributed to the increased incorporation of PEGDA and subsequently diminished presence of RGD peptide, as previously elucidated. Using a bright-field microscope, cell morphology in the 3D hydrogel was examined (**Figure 2.12B**). Significantly less cell differentiation occurred in 3D hydrogels than in 2D hydrogels. Compared to the GelMA groups, G:P=4:1 and G:P=2.5:2.5 groups showed different cell morphologies. Specifically, the round form and increased number of synapses of cells in the GelMA group indicated that they had developed into glial cells. In contrast, cells in the G:P=4:1 and G:P=2.5:2.5 groups exhibited a fusiform morphology and developed into neuronal cells. In this regard, it appeared that the material stiffness in a 3D environment influences N2a cell

differentiation significantly; the relatively stiff hydrogel environment (GelMA) promotes glial cell development while the relatively soft environment (G:P=4:1 and G:P=2.5:2.5 groups) facilitates neuronal cell differentiation [38, 194, 196].

To validate our results, cell differentiation and relative gene expression in 3D hydrogels were assessed on day 5 using immunofluorescence labelling and RT-qPCR. GelMA hydrogels exhibited more green fluorescence (GFAP) and high GFAP relative expression (1.4-fold) than GelMA-PEGDA hydrogels (**Figure 2.12C-D**), but GelMA-PEGDA hydrogels exhibited greater red fluorescence (Tuj-1) and high Tuj-1 expression (1.5-fold). This was consistent with our findings of cell morphology. However, differentiation in 3D hydrogels was much lower than in 2D hydrogels, indicating that neuronal differentiation in 3D hydrogels required much more sensitive control. Consequently, we examined the influence of mechanical stimulation (i.e. stretching) on neuronal development in a three-dimensional environment in more detail.

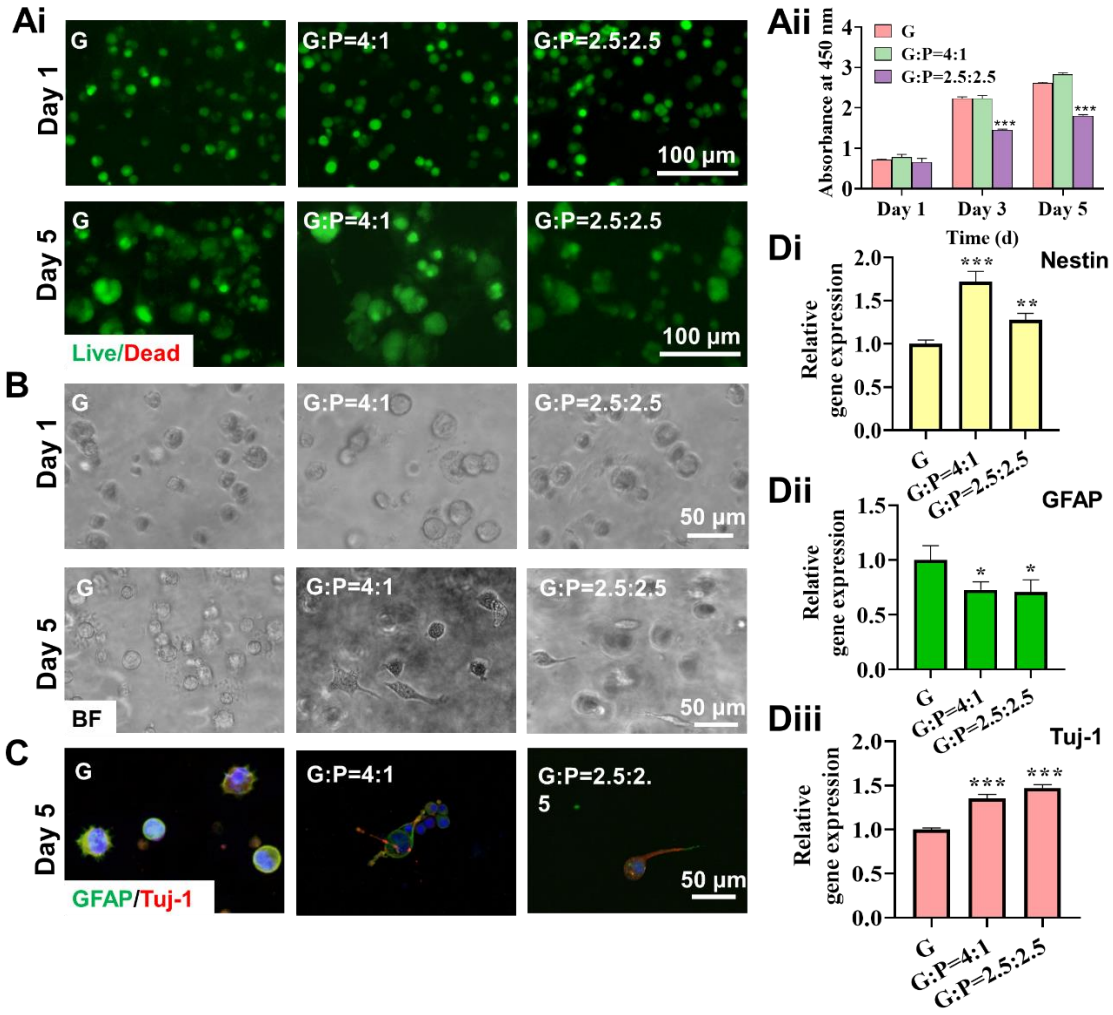

Figure 2.12 The influence of hydrogel stiffness on NSC differentiation in 3D hydrogels. **(Ai)** The Live/dead staining of different groups. **(Aii)** Cell proliferation in different 3D hydrogels. **(B)** Cell morphology of different groups. **(C)** Tuj-1 and GFAP immunofluorescence staining of different groups on day 5. **(Di-iii)** The RT-qPCR evaluation of relative gene expressions on day 5.

2.3.8 The influence of mechanical stretching on neuronal differentiation in 3D hydrogels

2.3.8.1 The influence of mechanical stretching on neuronal differentiation in 3D GelMA hydrogel

As indicated in **Figure 2.13**, GelMA hydrogels were elongated by 0%, 25%, and 50% of their original length. A live/dead experiment on day 1 demonstrated that cells in stretched hydrogels were still alive despite some dead cells, and that stretching had a minor influence on the viability of encapsulated N2a cells (**Figure 2.13A**). Cell morphology was investigated on a stretched 3D hydrogel using bright field microscopy (**Figure 2.13B**). The stretched cells exhibited more synaptic structures and extended axons (**Figure 2.13B** red arrows) than the non-stretched cells, which was most evident on day 5. On day 1, most cells were spherical and showed little neurite outgrowth. However, the cell pseudopodia exhibited evident elongation, especially in the stretching group on day 5. Again, most cells in GelMA hydrogel were glial cells because NSC were sensitive to glial differentiation in a stiffer environment (7-10 kPa) [196].

Relative gene expression and immunocytochemistry were used to evaluate the impact of mechanical stretching on neuronal differentiation in G hydrogels in detail. GFAP and Tuj-1 were used as unique markers for astrocytes and neurons, respectively. Neurite length rose when the stretching ratio was raised compared to the non-stretching group (**Figure 2.13C**). Compared with non-stretched G hydrogel, there was high gene expression in GFAP (2.3-fold) and Tuj-1 (1.5-fold) in the stretched G hydrogels,

indicating that mechanical stretching might enhance N2a differentiation (**Figure 2.13D**). Moreover, following stretching, the expression of GFAP rose more than that of Tuj-1 (a sign of neuronal cells), most likely because of the greater modulus (i.e. stiffness) of GelMA hydrogel.

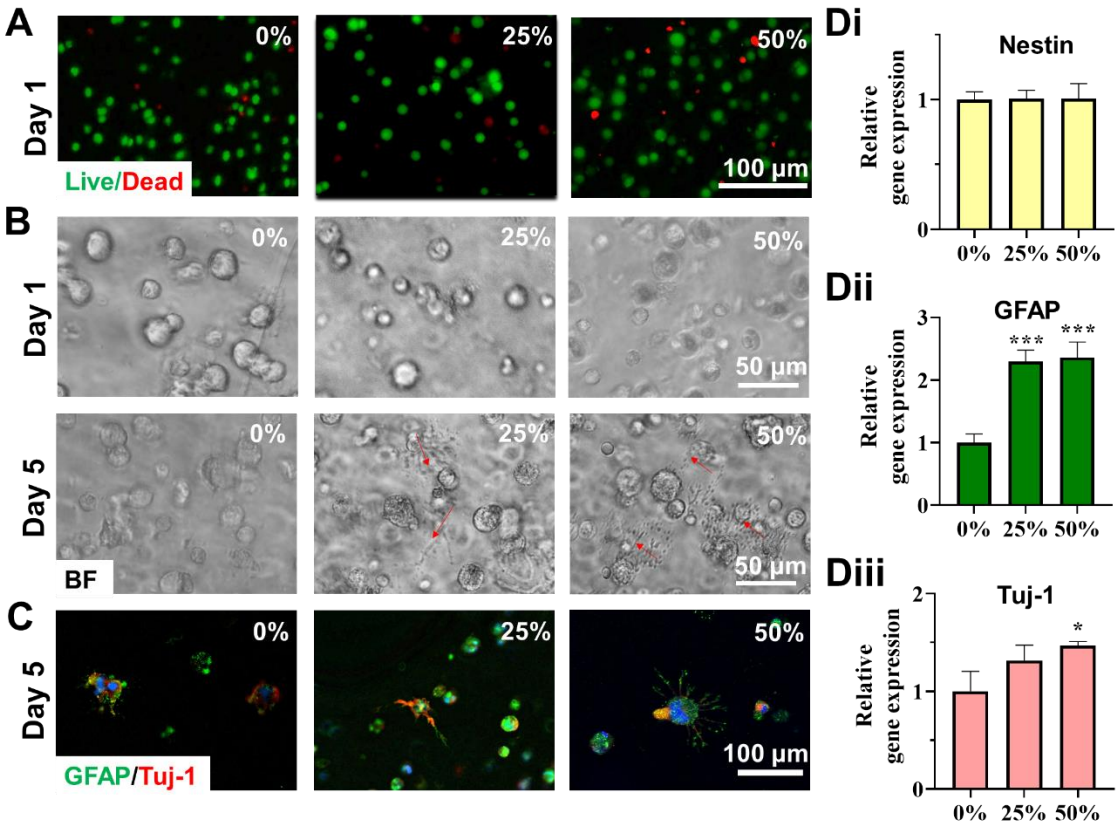

Figure 2.13 The influence of stretching 3D G (5 wt% GelMA) hydrogels on neuronal differentiation. **(A)** Live/dead staining of cells at different stretching ratios on day 1. **(B)** Cell morphology at different stretching ratios. **(C)** Tuj-1 and GFAP immunofluorescence staining at different stretching ratios on day 5. **(Di-iii)** The RT-qPCR evaluation of neuronal differentiation-related gene expressions at different ratios on day 5.

2.3.8.2 The influence of mechanical stretching on neuronal differentiation in 3D

GelMA-PEGDA hydrogels

G:P=4:1 and G:P=2.5:2.5 hydrogels were stretched for further investigation (**Figures 2.14** and **2.15**), and most stretched N2a cells maintained high viability (**Figure 2.14A** and **Figure 2.15A**). The morphology of N2a cells following stretching on days 1 and 5 was seen using microscopy (**Figure 2.14B** and **Figure 2.15B**). Compared with the GelMA group, no neurite outgrowth was seen on day 1. However, significant axons were developed after 5 days of incubation. Stretching may greatly boost neurite outgrowth, resulting in longer axon extension than the non-stretched groups. On day 5, neurites developed randomly in the 0% stretching hydrogels (**Figures 2.14C** and **2.15C**), but they grew in a more directed manner in the stretching hydrogels. Thus, the extension of the axon tended to follow the direction of stretching, as opposed to the random outgrowth in non-stretched hydrogels.

Immunocytochemistry aided in confirming the above results (**Figure 2.14C** and **Figure 2.15C**). GelMA-PEGDA hydrogels that were stretched exhibited longer neuron development than those that were not. In addition, the growth direction of neurite elongation correlated to tensile tension. In contrast, the intensity of Tuj-1 increased significantly in the stretched hydrogels. RT-qPCR was used to further measure relative gene expression (**Figure 2.14D** and **Figure 2.15D**). After 5 days of culture, the relative gene expressions of GFAP and Tuj-1 in the stretched GelMA-PEGDA hydrogel were about thrice and twice greater than in the non-stretched state, respectively. These results demonstrate conclusively that mechanical stretching impacts neuronal development

under stretching circumstances, particularly when the hydrogels are sufficiently flexible.

By comparing **Figures 2.14**, and **2.15**, we observed that the effect of stretching improves with an increase in PEGDA concentration. Specifically, the G:P=2.5:2.5 group exhibited the most significant elongation of axons, suggesting that the decrease in hydrogel modulus resulting from higher PEGDA content is favorable for neuronal differentiation and axonal extension. Additionally, the local stress induced by stretching was reduced as the increase of PEGDA (GelMA ~ 6 kPa, G:P=4:1 ~ 3 kPa, and G:P=2.5:2.5 ~ 1 kPa), leading to decreased cellular damage. Moreover, as the stretching ratio increased from 0% to 25%, a higher number of differentiated cells and increased gene expression were detected. However, beyond a stretching ratio of 25% and up to 50%, the effect of stretching appeared to diminish. Therefore, we propose that G:P=2.5:2.5 with a stretching ratio of 25% would be the ideal condition for our further investigations in Chapter 3.

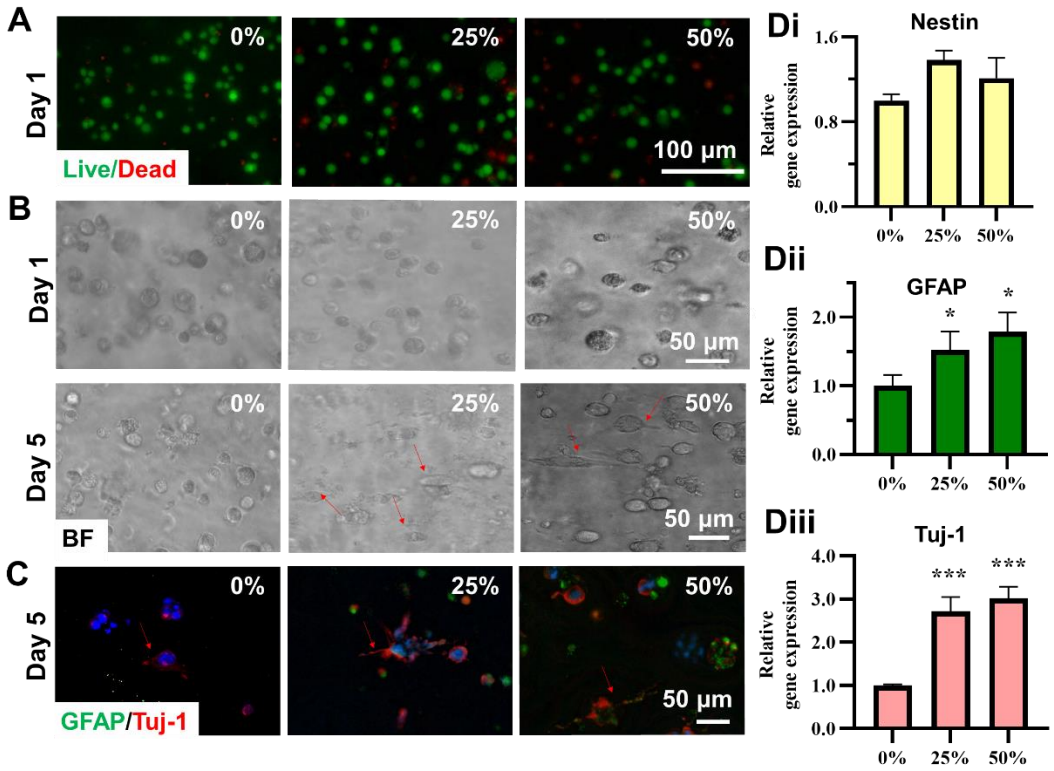

Figure 2.14 The influence of stretching 3D G:P=4:1 hydrogel on neuronal differentiation. **(A)** Live/dead staining of cells at different stretching ratios on day 1. **(B)** Cell morphology at different stretching ratios. **(C)** Tuj-1 and GFAP immunofluorescence staining at different stretching ratios on day 5. **(Di-iii)** The RT-qPCR evaluation of neuronal differentiation-related gene expressions at different ratios on day 5.

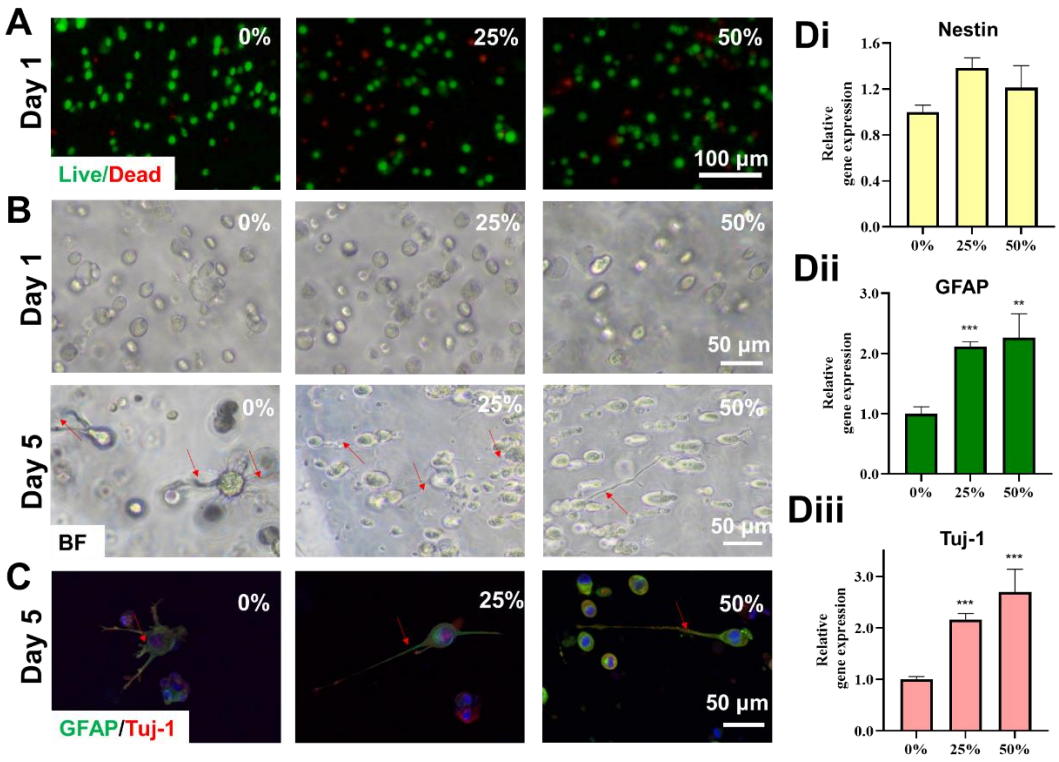

Figure 2.15 The influence of stretching 3D G:P=2.5:2.5 hydrogels on neuronal differentiation. **(A)** Live/dead staining of cells at different stretching ratios on day 1. **(B)** Cell morphology at different stretching ratios. **(C)** Tuj-1 and GFAP immunofluorescence staining at different stretching ratios on day 5. **(Di-iii)** The RT-qPCR evaluation of neuronal differentiation-related gene expressions at different ratios on day 5.

2.4 Summary

In summary, we developed soft and flexible GelMA-PEGDA hydrogels with an appropriate 3D environment for developing neuronal cells. Combining PEGDA into GelMA and altering concentration, we could adjust hydrogel matrix stiffness and increase their tensile characteristics. GelMA-PEGDA had an extraordinarily high biocompatibility for the growth of 3D neural cells, even though the addition of PEGDA had a small influence on cell survival and development owing to inadequate RGD group. Stem cells with significant GFAP protein expression in GelMA hydrogel (around 5.8 kPa) were more conducive to glial cell differentiation. In contrast, stem cells with significant Tuj-1 protein expression in GelMA-PEGDA hydrogel (0.8-2.8 kPa) were more conducive to neuronal cell development. This may be linked to variations in hydrogel stiffness and concentration of RGD peptides. Moreover, stem cells are sensitive to stiffness, and the mechanical modulus of 3D hydrogels affects neuronal differentiation more than changes in RGD peptide concentration, as shown by prior research [197]. According to our results, stiffness regulated neuronal cell differentiation, which was consistent with the findings of several previous research [38, 198]. In addition, we demonstrated that mechanical pressures might enhance 3D neuronal differentiation regarding axon extension and neurite direction. Overall, these findings demonstrated the high biocompatibility of GelMA-PEGDA hydrogel as a potential strategy to enhance the efficiency and viability of neural stem cell therapies.

Chapter 3 Effect of electrical stimulation and mechanical stretching on neural stem cell differentiation

3.1 Introduction

Previous studies have shown that mechanical strain may induce neuron development and neurite outgrowth in a 3D environment. In addition to mechanical cues, electrical signals are also a possible trigger for NSC differentiation. Mild electrical currents generated by bioelectric fields have been shown to promote growth factors that can increase nerve fibre outgrowth and accelerate axonal development on a 2D surface to control NSC differentiation [199, 200]. In the CNS and PNS, electric fields have been shown to trigger neuron regeneration *in vivo* [201]. ES has gained more attention because of its effectiveness in promoting nerve regeneration by altering the electro-responsiveness of neural cells [202]. However, because of the shortage of materials possessing appropriate conductivity and good biocompatibility, most research on ES remains focused on 2D substrates rather than 3D matrices [203]. Therefore, it is critical to create materials with similar conductivity and modulus as those of nerve tissues to facilitate 3D ES research.

Conductive hydrogels can provide an appropriate environment for direct ES applications to further enhance cell encapsulation and other cell responses [204]. Based on the potential and promising features of conductive hydrogels, incorporating ES into hydrogels will increase their suitability for diverse biomedical applications, such as

bimodal neural probes, tissue regeneration, and spinal cord repair [205, 206].

Among several conductive additives for hydrogels, PEDOT:PSS is supposed to be the best-known example among organic conductors due to its high conductivity, flexibility, and biocompatibility [112, 207, 208]. PEDOT-related polymers have been extensively employed as electroactive materials to control stem cell adhesion, proliferation, and differentiation. For example, Pires *et al*. found that a crosslinked PEDOT:PSS film increased the number of differentiated neurons [200]. In the previous chapter, we developed soft and stretchable GelMA-PEGDA (G:P=2.5:2.5, GP) hydrogels with high biocompatibility to support N2a viability and proliferation. In this chapter, we incorporated PEDOT:PSS into GP hydrogel for improving conductivity.

Herein, a photo-crosslinkable conductive hydrogel was developed based on GelMA-PEGDA by adding various PEDOT:PSS concentrations, which created a highly electrochemical environment. The concentration of PEDOT:PSS was optimised by mechanical properties, conductivity, and biocompatibility of the hydrogel. Next, the effects of ES intensity and duration on neuronal differentiation, neurite outgrowth, and relative gene expression were examined. Subsequently, the effects of combining mechanical stretching with ES on the neuronal development capacity of 3D conductive hydrogels were examined. Morphological traits, neuronal biomarker expression levels, and relative gene expression levels were investigated with various treatments. In addition, the MEA system was used to assess electrophysiological signals of neural

cells under both ES and mechanical stretching. Based on previous research and preliminary results, a combination of mechanical and ES may enhance the differentiation of NSC into mature and functional neurons.

3.2 Methodology

3.2.1 Fabrication of conductive hydrogels

GelMA and PEGDA were produced following the procedure described in Chapter 2, and GelMA and PEGDA hydrogels were synthesised using an amide reaction. To construct the conductive hydrogel, PEDOT:PSS was incorporated into GP hydrogel. To obtain solid PEDOT:PSS, its liquid form (MACKLIN, Shanghai) was first freeze-dried for 24 h according to a previously reported method [209]. Next, the completely dried product was dissolved in GP hydrogel at 0.5 and 1 wt% according to a previously reported method to form conductive hydrogels [210]. Correspondingly, GPL represents GP+0.5 wt% PEDOT:PSS; GPH represents GP+1 wt% PEDOT:PSS. The hydrogel solution was then thoroughly mixed with 0.5 wt% LAP for further crosslinking. Subsequently, the mixed hydrogel was photo-crosslinked by UV as before.

3.2.2 Physicochemical characterisation of conductive hydrogels

3.2.2.1 Scanning electron microscopy (SEM)/Energy-dispersive spectroscopy (EDS)

SEM was employed to characterize the morphologies of the hydrogels produced after freeze-drying. The crosslinked conductive hydrogels with a cylindrical shape (d=10 mm, h=3 mm) were prepared and lyophilised under vacuum at -80°C. After coating with gold, the dry hydrogels were split along the centre and photographed by SEM. In

addition, EDS was used to describe the fundamental hydrogel composite at an accelerating voltage of 12 keV.

3.2.2.2 Fourier transform infrared (FTIR)

An FTIR spectroscope (Thermo, 6700) was used to assess the chemical structure and composition of the conductive hydrogels. The hydrogel and potassium bromide were compressed into pellets using a PerkinElmer. Scans (n=64) were performed on each sample with a resolution of 4 cm^{-1} and a wavenumber range of 4000–500 cm^{-1}.

3.2.2.3 Mechanical testing

Mechanical stretching was performed using a dynamic universal mechanical system. Dumbbell-shaped hydrogel samples (L=15 mm, W=2 mm, T=1.5 mm) and cylindrical samples (d=10 mm, h=5 mm) were prepared separately for tensile and compression tests, respectively [211].

3.2.2.4 Swelling experiment

To ascertain the effect of crosslinking on the hydrogels, cylindrical samples (d=10 mm, h=3 mm) were subjected to swelling tests at room temperature [170]. The ability of the hydrogels to swell was evaluated by measuring the change in mass of specimens immersed in PBS at varying intervals through **Eq. 2.1**.

3.2.3 Characterisation of the electrical behaviour of conductive hydrogels

3.2.3.1 Conductivity

A Keithley model 2361 multimeter was used to assess the electrical conductivity of the conductive hydrogels in a previous study (Keithley Instruments, USA) [212]. The hydrogel samples were cut into 2×2×10 mm rectangles, and their resistance (R) was measured using a multimeter to determine the electrical resistivity (ρ) (**Eq. 3.1**):

$$\rho = R\frac{A}{L} = R\frac{W \times H}{L} \qquad \textbf{(3.1)}$$

where L, H, and W are the specimen's length, height, and breadth and A is the specimen's cross-sectional area. Electrical resistivity (ρ) and conductivity (σ) are opposites of one other σ = 1/ρ, in units of S/m.

3.2.3.2 Electrochemical impedance (EIS)

EIS of the conductive hydrogels was performed using an electrochemical workstation (CHI600E, CH Instruments, China). The electrolyte solution used was PBS (0.1 M, PH7.4). Crosslinking and testing of the conductive hydrogels on the working electrode (**Schematic 3.1B**) were performed, with Ag/AgCl and platinum (Pt) serving as the reference and counter electrodes (CE), respectively (**Schematic 3.1A**). The activity between 1 and 100,000 Hz was examined.

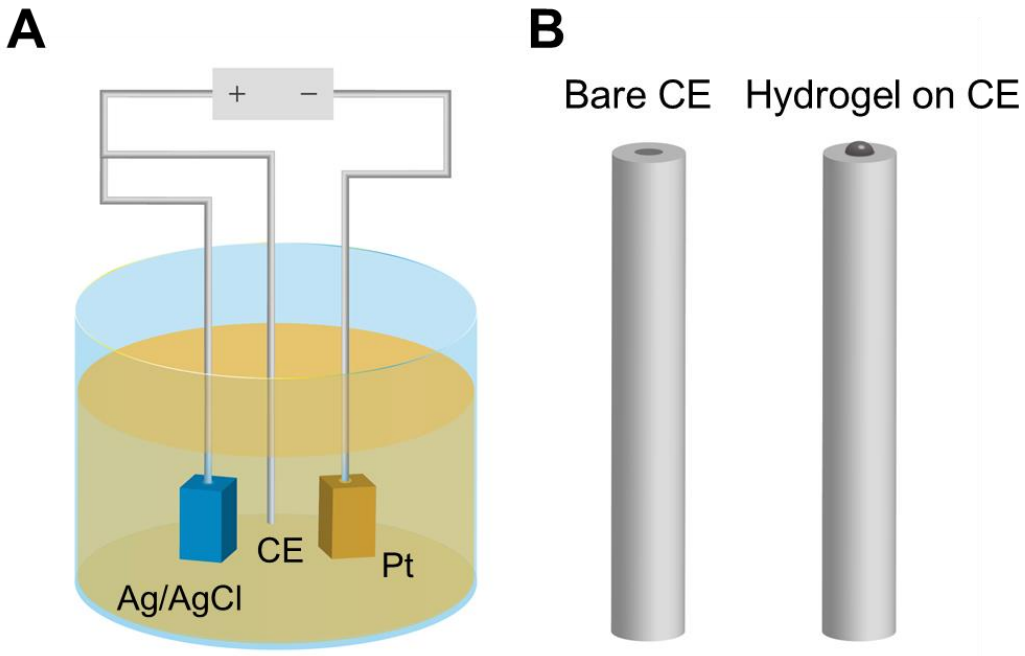

Schematic 3.1 (A) Electrochemical impedance properties of conductive hydrogel were measured with a three-electrode system. **(B)** Photographs of (left) a bare carbon electrode (CE) and (right) the hydrogel immobilised on the CE.

3.2.3.3 Cyclic voltammetry

To investigate the current response and charge delivery capacity of the conductive hydrogel, cyclic voltammetry (CV) was performed at another electrochemical workstation under the same conditions as EIS. The conductive hydrogel was crosslinked on top of the carbon electrode and was used as the working electrode. After three repetitive potential scans, the CV curves were obtained between -0.8 and 0.4 V at a scan rate of 100 mV/s.

3.2.4 Cell viability and proliferation

N2a cells were also chosen for the experiments in this chapter; the cell culture procedures are the same as in Chapter 2. The biocompatibility of the conductive hydrogels was assessed by seeding and integrating N2a cells into the hydrogels. The viability of N2a cells was assessed using live/dead staining. The data were then analysed using Fiji software to determine the fractions of living and dead cells. On days 1 and 5, Cell Counting Kit-8 demonstrated the multiplication of N2a cells after they had been grown with conductive hydrogels.

3.2.5 Construction of ES and stretching system

After cells were incorporated into the hydrogel, a complete DMEM medium with 10 % FBS was used on day 1, and a differentiation medium with 1 % FBS and 10μM RA was applied on day 2. For the electrical treatment, ES was applied to both the GelMA-PEGDA hydrogel and conductive hydrogel using an electrical pulse generator (SDG-2105 function generator, DINGYANG) from day 3. An electrical field of 100 mV/mm with a frequency of 100 Hz was chosen for this experiment through two copper electrodes for 20 min each day (**Schematic 3.2**). The electrodes were connected to a pulse generator using alligator clips [213].

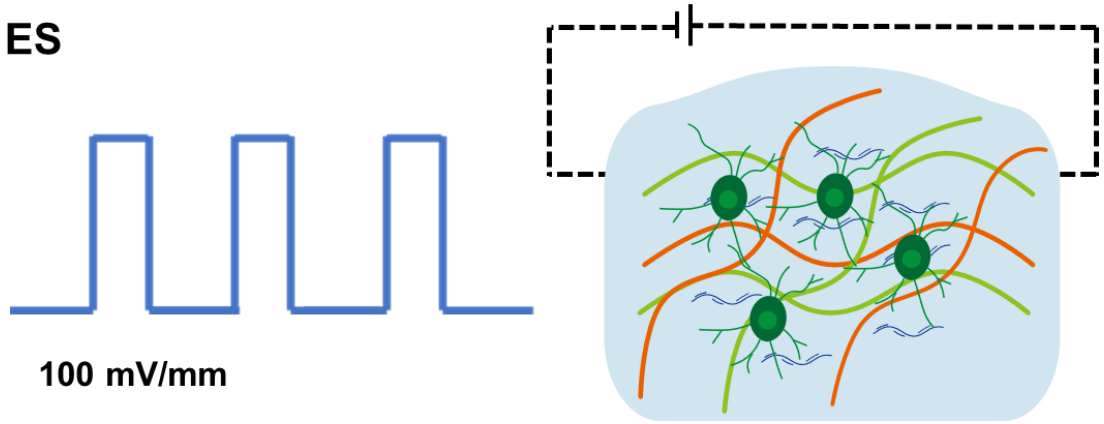

Schematic 3.2 Diagram of electrically stimulated conductive hydrogels and encapsulated cells (100 mV/mm).

We further assessed the effect of ES and optimised the timeframe and electric intensity for stimulation. Cell behaviour under different electrical fields (10 mV/mm, 100 mV/mm, and 1 V/mm) was explored, and neural cells were observed under the microscope after ES every 2 days.

3.2.6 ES and mechanical stretching of 3D conductive hydrogels

A stretchable PDMS mould was designed to provide mechanical stretching to the 3D conductive hydrogel, as shown in **Schematic 3.3**. Different ratios of phases A and B (10:1, 20:1, 30:1, 40:1, and 50:1) were chosen for the construction of the PDMS mould. We found that the stretching ratio increased as the proportion of curing agent decrease from 10:1 to 30:1. However, when the ratio of A:B over 30:1 the cured PDMS became sticky and A:B>50:1 PDMS became difficult to cure. The PDMS mold was fabricated with a PDMS precursor and curing agent (Sylgard 184, Dow Corning Toray) at 30:1

leading to a softer substrate for stretching. After completion, the mould was sterilised by autoclaving before use. Fibronectin human plasma (Sigma, Aldrich) was pre-coated on the PDMS mould for 24 h in an incubator. The N2a encapsulated in the conductive hydrogel was loaded onto the mould with ES or mechanical stretching.

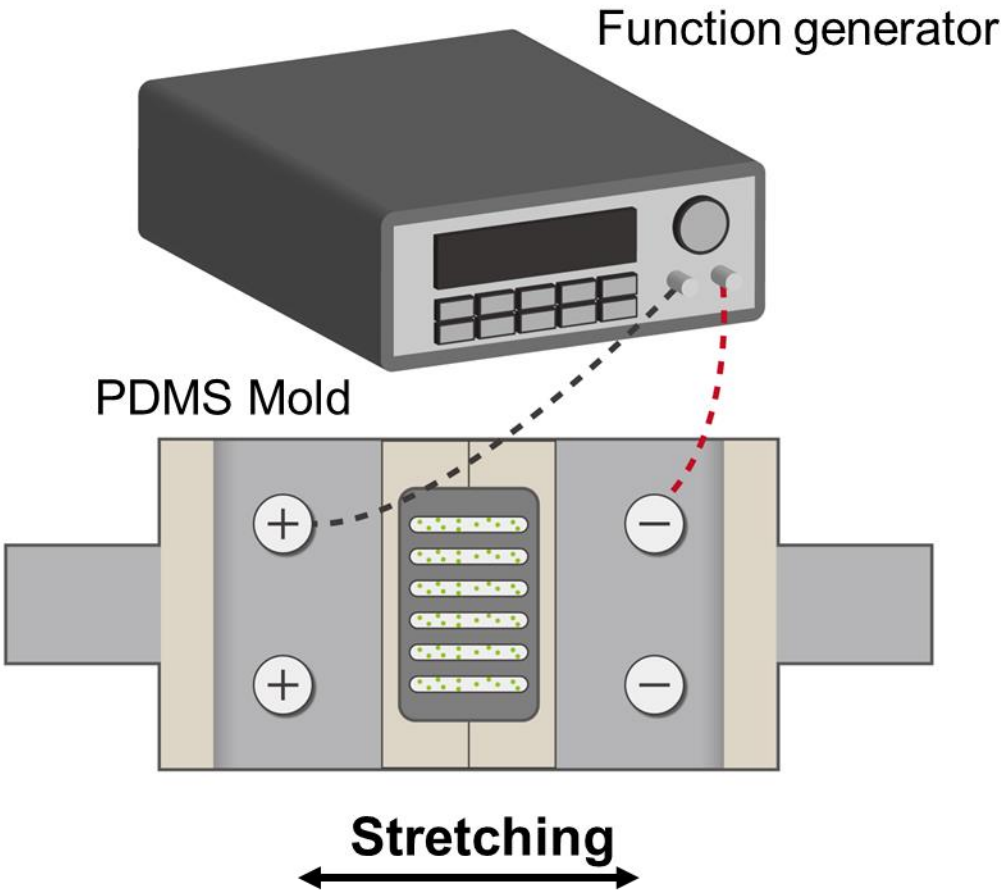

Schematic 3.3 Schematic diagram of ES and mechanical stretching of the 3D conductive hydrogel.

3.2.7 Cell morphology, immunocytochemistry, and image analysis

As described earlier, the cytoskeleton and nucleus were respectively stained with phalloidin and DAPI to examine sample morphology. After 20 minutes of

permeabilization with 0.1% Triton, the cells were blocked in 1% BSA for 45 min. The samples underwent a 45 min incubation in phalloidin solution, followed by a 5 min incubation in DAPI solution. The specimens were observed and analyzed by fluorescence microscope (Nikon, Japan) after rinsing thrice with PBS.

Antibody labelling validated NSC differentiation. All hydrogel samples were treated with 4% paraformaldehyde for 20 min. After 20 min, 0.1% Triton was added to further penetrate the samples. After a 45-min incubation in 1% BSA, samples were treated with two primary antibodies (GFAP and Tuj-1) overnight at 4°C, followed by 2h two secondary antibodies incubation. Finally, after 5 min at 37°C, the DAPI solution was added for counter-staining. The samples were inspected using a confocal microscope (ZEISS LSM 900) after washing thrice with PBS.

Images were captured using an Olympus inverted microscope (Nikon, Japan) and a confocal microscope (ZEISS LSM 900) to quantify the morphological features. The Fiji package in ImageJ (National Institutes of Health, USA) was used for quantitative analysis. NeuronJ plugin of Fiji was used to measure neurite length, and number of roots from 11 cells in each condition was used for statistical analysis [177]. In addition, neurite outgrowth was quantified using ImageJ and categorised into eight classes based on its growth pattern [214].

3.2.8 RNA extraction and gene expression

Per previous literature, RT-qPCR was used to check the target gene expression [178]. The cells grown on the 2D hydrogel were harvested by trypsinization after various incubation periods. Collagenase type II was used to break down and liberate the 3D cells encapsulated in the hydrogels. The total RNA of the obtained N2a cells was extracted using the Total RNA Kit, and reverse transcribed into cDNA. To normalise results, the expression levels were standardized by employing GAPDH as an internal control. **Table 2.1** lists the sense and antisense primer sequences used for a group of related genes. The $2^{-\Delta\Delta Ct}$ technique was used to determine gene expression.

3.2.9 Electrophysiology evaluation

Electrophysiology evaluation was performed using the MEA System (Alpha MED Scientific Inc., Japan). A probe MED-P515A (50×50 μm in size and 150 μm in spacing) with 64 electrodes was chosen for this study, as shown in **Figure 3.1**. The probe was placed in fresh distilled water for 24 h and sterilised using 70% alcohol for 30 min before use. Then, exposure to UV light was provided for 15–30 min for further sterilisation.

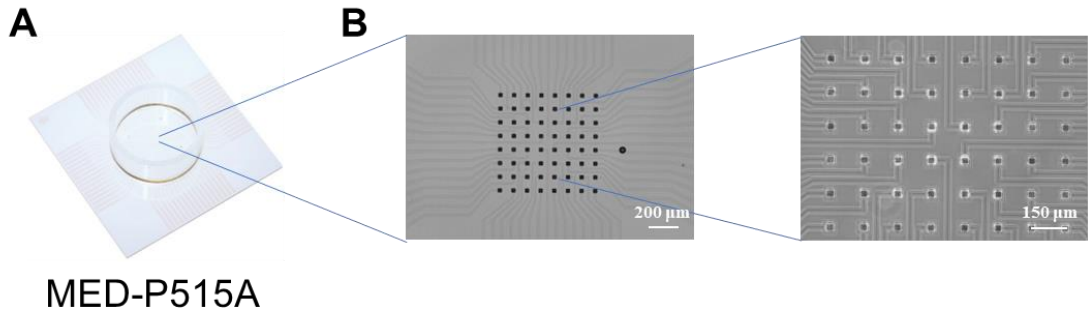

Figure 3.1 The MED-P515A probe **(A)** and magnified microstructure of MED probe (**B**, 50 × 50 µm in size and 150 µm in spacing).

N2a cells encapsulated within the conductive hydrogel were seeded directly onto the probe in a disposable cell Petri dish. A cloning ring with an inner diameter of 5 mm was used to seed the dispersed cells, primarily in the central area containing 64 electrodes. The cells were cultured for 10 days, during which the culture medium was exchanged every second day until recording began. For excitatory postsynaptic potential (EPSP) evaluation, the sample was electrically stimulated by two selected electrodes according to the Mobius EPSP protocol. Each stimulation began with 5 ms pre-stimulation (0 µA) followed by a biphasic ES of 10 µA for 0.2 ms and post-stimulation of 94.8 ms (0 µA). A total of 1000 traces with 1.0 Hz were recorded. Before sampling, baseline signals were captured for 10 min. After 1 min of signal stabilisation, the recording was restarted.

Type	Length (ms)	Amplitude (µA)
Const	5.00	0.00
Pulse	0.2	-10.00
Const	94.80	0.00

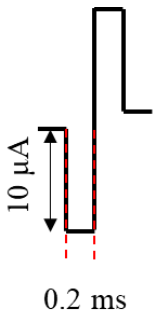

Schematic 3.4 Diagram for excitatory postsynaptic potential stimulus protocol: Pre-

stimulation for 5 ms (10 μA) and post-stimulation for 94.80 ms.

Neural spikes were also recorded through the MEA system according to the spike recording cluster protocol. Signals were recorded every 30 min for 5 min, as shown in **Schematic 3.5**. This was repeated 48 times. Afterwards, the spike signals were sorted through "Spike recording (filter) cluster" workflow templates with a similarity radius of 30%.

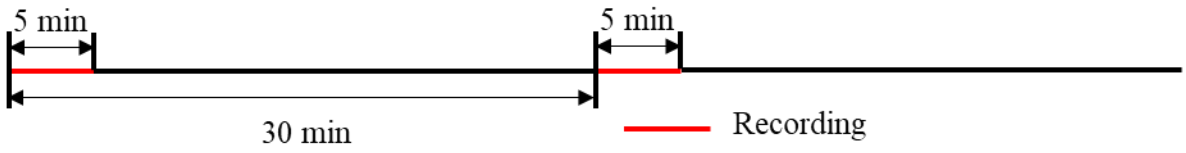

Schematic 3.5 Diagram for spike recording trace (5-min recording every 30 min)

3.3 Results and discussion

3.3.1 Characterisation of conductive hydrogels

3.3.1.1 Morphology and composition of hydrogels

Conductive hydrogels were constructed by incorporating PEDOT:PSS into GP hydrogels. As shown in the macro view in **Figure 3.2A**, the transparency of the conductive hydrogels (GPL and GPH) changed from transparent to dark blue after PEDOT incorporation, and the colour of the hydrogel gradually deepened with increasing PEDOT content. The chemical combination of PEDOT:PSS with GelMA, PEDOT, and the hydrogel is shown in **Figure 3.2B**. The PEDOT:PSS monomer was polymerised to form conducting polymer chains through the hydrogen bonds in the hydrogel network. The microstructural features of conductive hydrogels were characterised using SEM. As visualized in **Figure 3.2C**, the hydrogel displayed a consistently porous structure with the average pore sizes of 21.97μm, 21.70μm and 22.47μm for GP GPL and GPH. Compared to the conductive scaffolds, the average pore size of the remain unchanged, indicating the stability of the porous hydrogel structure, which remained consistent after the incorporation of PEDOT:PSS. Meanwhile, the elemental composition of the GelMA-PEGDA hydrogel and conductive hydrogel (GPL) was analysed by EDS. As shown in **Figure 3.2D**, the fraction of S atoms was increased from 0% in the GelMA-PEGDA hydrogel to 0.5% in the GPL, suggesting the successful introduction of PEDOT:PSS into the hydrogel matrix.

In **Figure 3.2E** of the FTIR spectrum, the distinctive peak observed at 3306 cm^{-1} can be attributed to the C-H stretching vibrations of GP [215]. The peaks at 1647 and 1540 cm^{-1} corresponds to the stretching vibrations of the -C=O short bond and -N-H bond bending, respectively [216]. In the curve of PEDOT:PSS, the peaks of the $-SO_3^-$ group was observed at 1145 and 1009 cm^{-1}. Meanwhile, the peak at 835 cm^{-1} corresponded to the plane vibrations of =C-H [217]. After incorporating PEDOT:PSS into GP, some peaks in the spectra of GPL and GPH showed changes in shape or size compared with those of GP. For example, the peak at 1145 cm^{-1} shifted to 1185 cm^{-1}, indicating the presence of hydrogen bonds between GP and PEDOT:PSS. In addition, with an increase in the PEDOT:PSS content, the characteristic peaks belonging to GP at 3306, 1647, and 1540 cm^{-1} gradually became weaker, and the characteristic peak belonging to PEDOT:PSS at 1009 cm^{-1} gradually became stronger [218]. These changes indicated intramolecular interactions between the two materials.

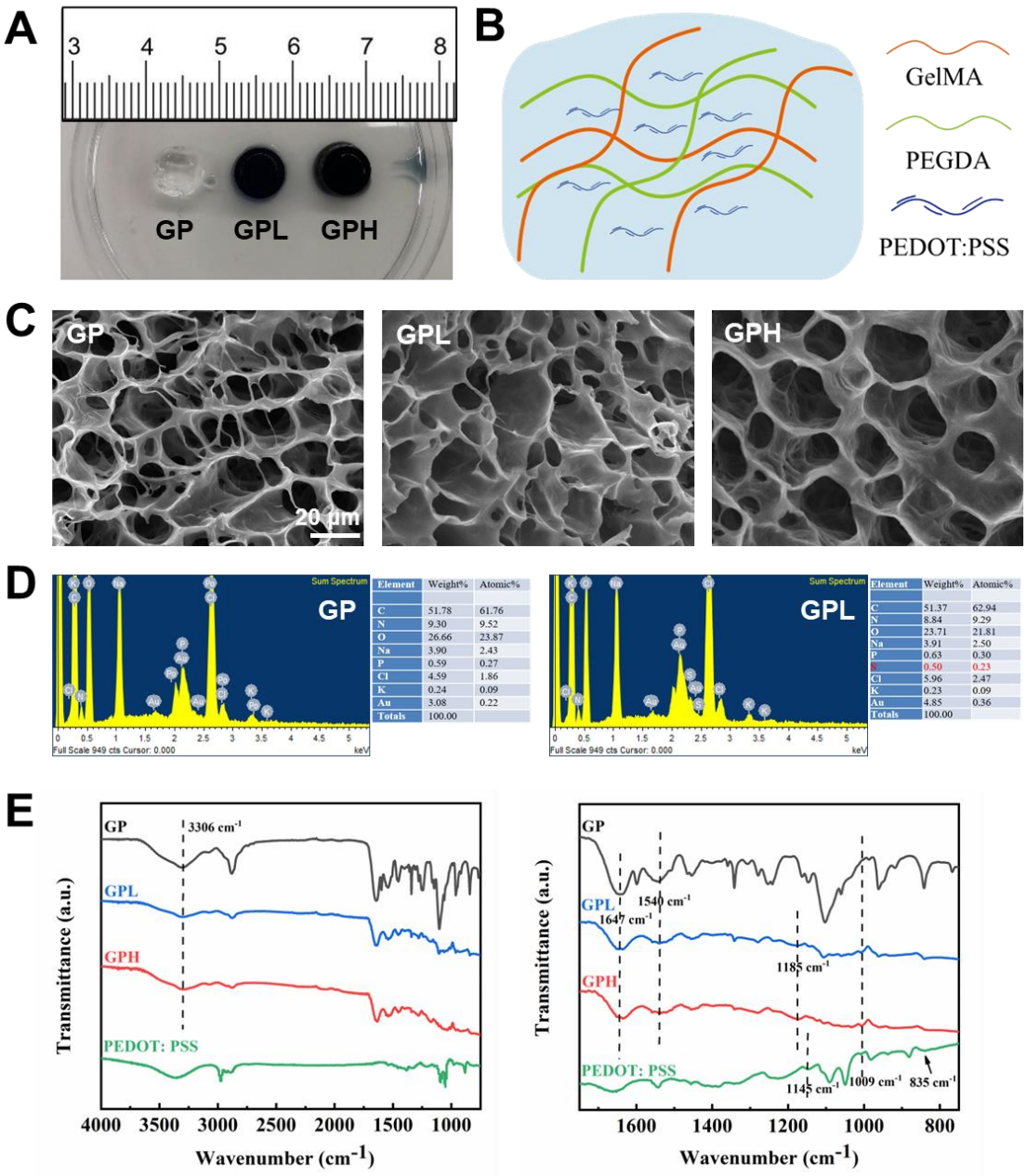

Figure 3.2 Characterisation of hydrogel morphology and composition. **(A)** Macro view of different hydrogels (From left to right: GP, GPL, and GPH hydrogel) **(B)** Schematic representation of the chemical structure of conductive hydrogel. **(C)** SEM micrographs of different hydrogels. **(D)** Elemental composite of GP and GPL hydrogels analysed by EDX. **(E)** FITR spectrum of GP, GPL, GPH, and PEDOT:PSS.

3.3.1.2 Swelling and mechanical characterisations of hydrogels

The swelling behaviour can reflect the network structure and crosslinking performance of the hydrogel, which is an important physicochemical property. Different cylindrical hydrogel samples were immersed in PBS, and the mass changes of the samples were weighted at different time points. **Figure 3.3A** shows that the swelling ratio attained equilibrium after 9 h and increased slightly with the increase of PEDOT:PSS. The GPH group had the highest swelling ratio (approximately 110%), whereas the GP group had the lowest (around 90%). These changes in the swelling ratio were mainly due to the weaker crosslinked network structure resulting from incorporating PEDOT:PSS. There has been repeated discussion on the decreased transparency due to PEDOT:PSS, resulting in decreased photo-crosslinking efficiency.

We further evaluated the compression and tensile moduli of different hydrogels. In the compression test, the different hydrogels demonstrated normal linear elasticity under mild stress (**Figure 3.3B**). Although the compression moduli decreased slightly with the increase in PEDOT:PSS owing to the decrease in transparency, no significant differences were observed (**Figure 3.3E**). The compression moduli of these three hydrogels were approximately 1 kPa, similar to the moduli of our neural tissues [36, 37]. Reportedly, NSC tend to differentiate into nerve cells in a relatively soft environment (~1 kPa). Therefore, these hydrogels are beneficial for cell encapsulation growth and differentiation. In addition, we studied the differences in tensile performance between various compositions because stretching was an important parameter. **Figure 3.3C** illustrates that the incorporation of PEDOT:PSS decreased the

tensile moduli (from 13kPa to 11kPa) and improved the elongation at break (from 175% to 210%) owing to its highly flexible properties [208].

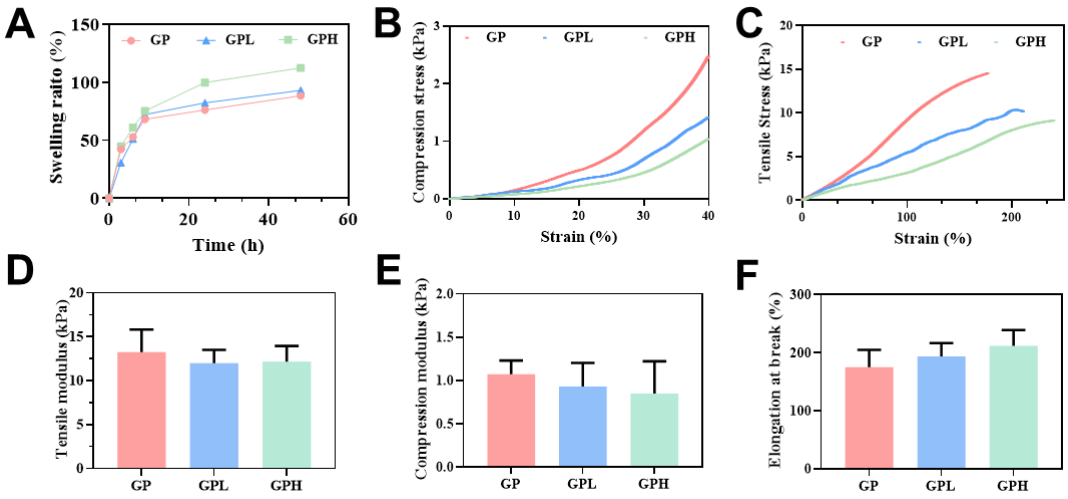

Figure 3.3 Swelling and mechanical results for different hydrogels. **(A)** Swelling properties. **(B)** Compression stress-strain curves. **(C)** Tensile stress-strain curves. **(D-E)** Tensile and compression moduli **(F)** Elongation at break and swelling properties.

In line with our previous method, we also investigated the changes in modulus during the degradation process in this chapter. **Figure 3.4A** demonstrates the swelling ratio of the hydrogels over time, reaching approximately 90%, with no significant differences observed between the groups. Likewise, the modulus of GP, GPL, and GPH exhibited similar trends in **Figure 3.4B**. Initially, there was a significant drop in modulus on the first day due to hydrogel swelling, which was followed by a stable modulus of around 1 kPa for the subsequent six days in the culture medium. Notably, the introduction of PEDOT:PSS into the hydrogel system resulted in an increase in its concentration while simultaneously causing a reduction in system transmittance. This alteration had a discernible impact on the crosslinking dynamics of the hydrogel system [209].

The degradation of the conductive hydrogel and the corresponding modulus changes in collagenase are presented in **Figures 3.4C-D**, respectively. As depicted in the bar chart, hydrogels with higher PEDOT: PSS content (GPH) degraded at a faster rate compared to GP, while only a slight difference was observed between GP and GPL. GPH completely degraded by day 3, followed by GP and GPL with no significant differences. Additionally, all hydrogels exhibited a noticeable decrease in modulus on day 1 under collagenase degradation. Notably, GP demonstrated the highest compression modulus throughout the entire period. The introduction of PEDOT:PSS promoted the degradation of the conductive hydrogel, particularly at higher concentrations, due to the reduced degree of crosslinking caused by decreased light transmittance [208].

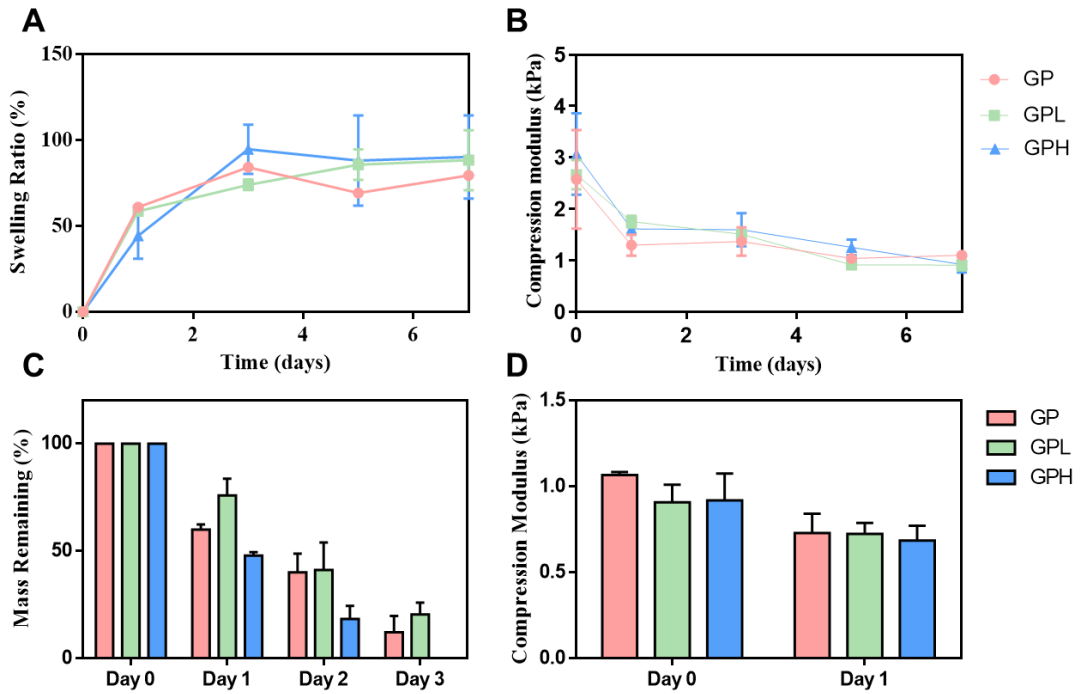

Figure 3.4 (A) Swelling properties of the hydrogels in DMEM. **(B)** Compression modulus of the hydrogels incubated in DMEM solution within 7 days. **(C)** Degradation

properties of the hydrogels in 0.2 U/mL collagenase type II solution. **(D)** Compression modulus of the hydrogels incubated in collagenase within 2 days.

3.3.2 Electrical properties of conductive hydrogels

3.3.2.1 Conductivity

To investigate their electrical properties, conductive hydrogels were cut into rectangular shapes (weight=2 mm, height=2 mm, length=10 mm) using a biopsy punch. The resistivity and conductivity of the hydrogels were measured using a multimeter (**Figure 3.5A**). With an increase in PEDOT concentration, a reduction in resistivity was observed, from 2300 Ω·m to 160 Ω·m for GP and GPH, respectively (**Figure 3.5B**). Concurrently, incorporating PEDOT:PSS increased the conductivity of the hydrogel from 0.0004 S/m to 0.006 S/m (**Figure 3.5C**). The observed improvement in conductivity and reduction in resistance can be attributed to the realignment of densely packed and well-organized structures of PEDOT:PSS. This reorganization promotes enhanced charge transport and facilitates more efficient electron flow within the system. The GPH hydrogel with a high PEDOT:PSS content demonstrated superior electrical conductivity and electron transport properties. Meanwhile, the conductivity of the conductive hydrogel (GPL and GPH) was similar to that of neural tissue (8×10^{-4} to 4×10^{-2} S/m), suggesting that our conductive hydrogel was appropriate for neural regeneration [68, 69, 219].

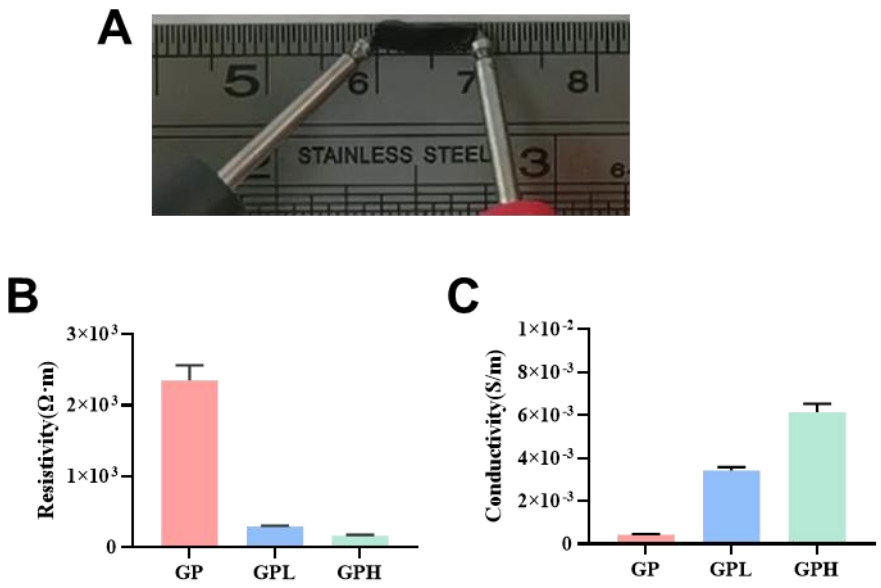

Figure 3.5 Conductivity tests for different hydrogels. **(A)** The schematic representation of the conductivity test. The resistivity **(B)** and conductivity **(C)** of the conductive hydrogels.

3.3.2.2 Impedance spectra

EIS of the conductive hydrogel is also a key component that influences the fate of stem cells through the hydrogel itself or ES. The electrochemical impedance characteristics of the hydrogels with varying PEDOT:PSS concentrations were evaluated using a three-electrode EIS setup. As depicted in **Figure 3.6**, the Nyquist plots for GPL and GPH initially displayed greater radians and steeper increases. The slope of Nyquist curves in GP was approximately 44°, which was reduced to 34° (GPL) and 33° (GPH) after the addition of PEDOT:PSS, suggesting a decreased impedance for charge transfer and a quicker rate of electron transfer between the electrode surface and solution. For the impedance of different hydrogels (**Figure 3.6C**), other than the growth in conductivity,

incorporating PEDOT:PSS into the hydrogel network could provide higher electroactivity and conductivity for electrical signal transmission [220]. GelMA-PEGDA exhibited high impedances at all frequencies, whereas the conductive hydrogels (GPL and GPH) exhibited relatively low impedances. For example, the impedance values of the GP, GPL, and GPH at 10 Hz were 9 kΩ, 5 kΩ, and 3 kΩ, respectively.

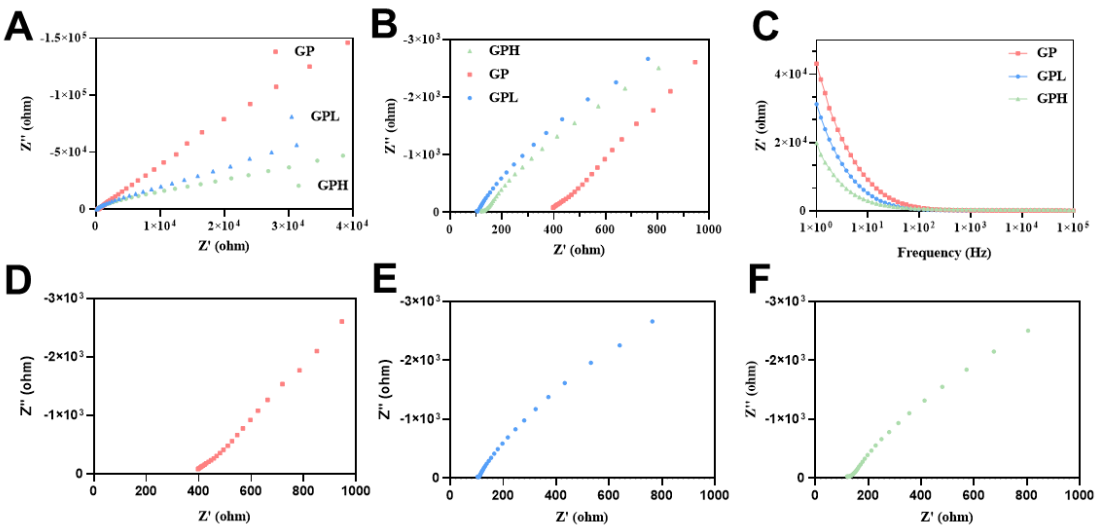

Figure 3.6 Electrochemical impedance spectroscopy (EIS) of different hydrogels. **(A-B)** Nyquist curves. **(C)** Electrochemical impedance curves. **(D-F)** The independent Nyquist curves at low impedance.

3.3.2.3 Cyclic voltammetry

The response characteristics of the conductive hydrogels were assessed by comparing the CV curves of different PEDOT:PSS concentrations. In **Figure 3.7**, the region within the cyclic graph indicates that the charge delivery capacity of the tested capacitors varied. Compared with the pristine GelMA-PEGDA hydrogel (GP), the conductive

GelMA-PEGDA hydrogels (GPL and GPH) exhibited higher currents and capacitances for charge delivery with a larger CV area. These results suggest that incorporating PEDOT:PSS can significantly improve electrical properties. However, the electrical performance of the hydrogels was not significantly improved by increasing PEDOT:PSS (GPH) concentration when PEDOT concentration exceeds 0.5 wt%. Therefore, 0.5 wt% PEDOT:PSS (GPL) was sufficient to create the conductive network. As per previous reports, PEDOT:PSS enhances the electrical properties of the hydrogel by providing densely packed realignment and a highly ordered network structure [221]. The conductive hydrogel constructed in this study met the criteria for the electrical conductivity of ES in neural tissue engineering.

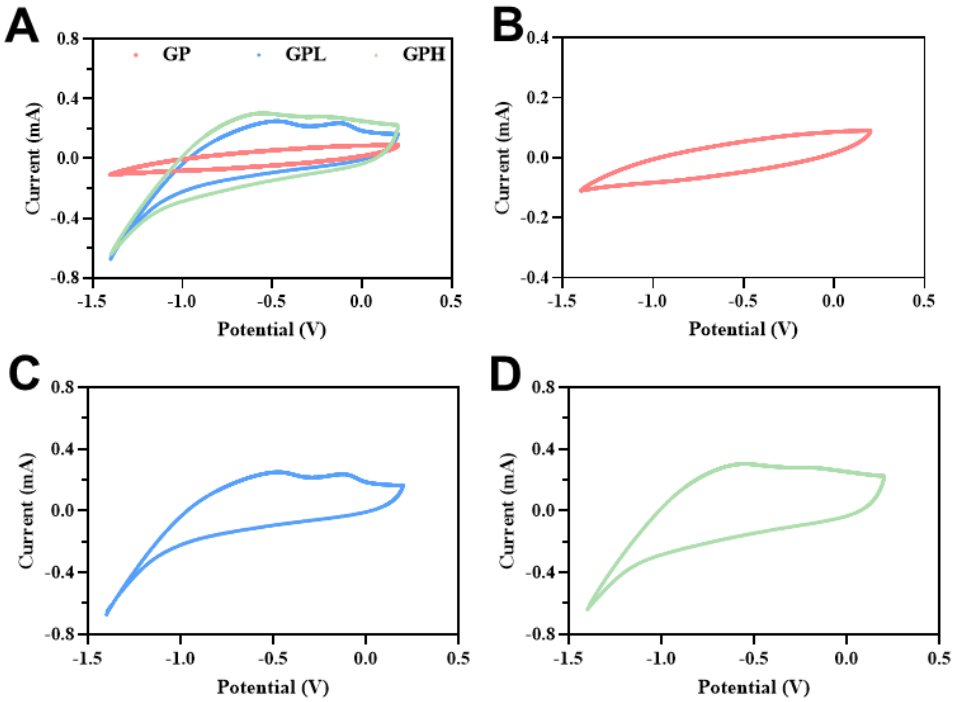

Figure 3.7 Cyclic voltammetry (CV) curves with a scan range from −0.8 to 0.4 V at a scan rate of 100 mV/s. **(A)** CV curves of hydrogels. **(B-D)** The independent CV curve of GP **(B)**, GPL **(C)** and GPH **(D)** hydrogel.

3.3.2.4 The impact of electrical field intensity on the temperature of hydrogels

The heat generated during electrical stimulation has the potential to impact cell viability, differentiation, and function within the hydrogel, particularly if the temperature surpasses a certain threshold. To assess the heat generated by the electrical field, we utilized a thermographic camera [222]. Our observations revealed a correlation between the electrical conductivity and field strength of the hydrogel and the heat produced. With the augmentation of conductivity and electrical field, the temperature of the hydrogel gradually rose, as depicted in **Figure 3.8**. Specifically, a high electric field of 1 V/mm resulted in a temperature increase of 1°C in the hydrogel. However, due to the hydrogel's high specific heat capacity, lower conductivity levels (100 mV/mm) did not induce a significant change in temperature. Consequently, we believe that although a small amount of heat is generated, it does not have a substantial impact on the temperature of the hydrogel or cellular behavior, especially at lower electrical field strengths.

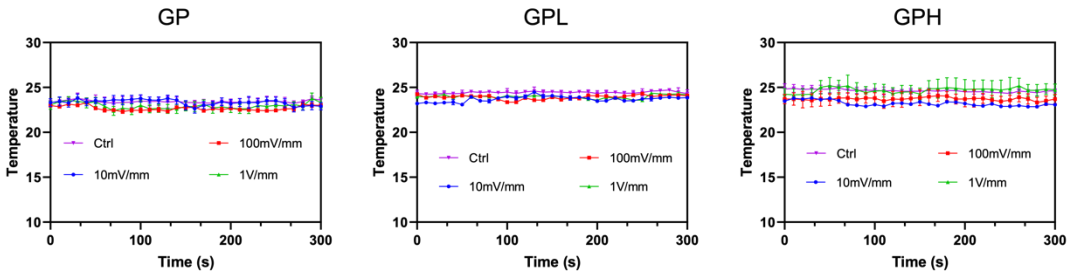

Figure 3.8 Temperature changes during electrical stimulation.

3.3.3 Biocompatibility of conductive hydrogels

We assessed the biocompatibility of the conductive hydrogels for neural tissue

engineering, we conducted an evaluation of N2a cell viability and proliferation on both 2D and 3D hydrogel. To assess cell viability on 2D hydrogels, live/dead cell staining was employed. A 24-well plate containing N2a cells served as the negative control. As depicted in **Figure 3.9A** and **Figure 3.9Ci**, the cells were viable with negligible cytotoxicity detected. After 24 h of incubation, the cells remained 95% viable. Similar to the control samples, the N2a cells were equally distributed over the hydrogels, suggesting high cytocompatibility of the conductive hydrogels. After confirming the effectiveness of the 2D hydrogels, cell morphology and proliferation were assessed in the 3D hydrogels. From the BF images in **Figure 3.9**, cells were distributed evenly in the 3D hydrogel with a spherical shape on day 1, and the cells encapsulated in GP and GPL hydrogels displayed robust cell proliferation and the formation of distinct cell clusters by day 5, suggesting the favourable biocompatibility of GP and GPL hydrogels for 3D cell encapsulation. However, compared with the GP and GPL groups, the cell morphology of the GPH group with a high PEDOT:PSS concentration became less regular, and the number of cell clusters decreased on day 5. Quantitative cell proliferation in the 3D hydrogels was evaluated using CCK-8. As shown in **Figure 3.9 Cii**, similar absorbance values at 450 nm (about 0.25) were observed in different groups on day 1, and the absorbance increased significantly after cultivation for 5 days for the GP and GPL groups, which agreed with the BF observation. The cell proliferation in the GPH group was relatively low compared to the GP and GPL groups, probably because the high PEDOT:PSS concentration induced weak biocompatibility [213]. Although PEDOT:PSS has been reported to have good biocompatibility, neural cells

are very sensitive to their surroundings, particularly in 3D environments [219]. Considering the relatively weak biocompatibility of GPH, we selected a GPL conductive hydrogel for ES in the following experiments.

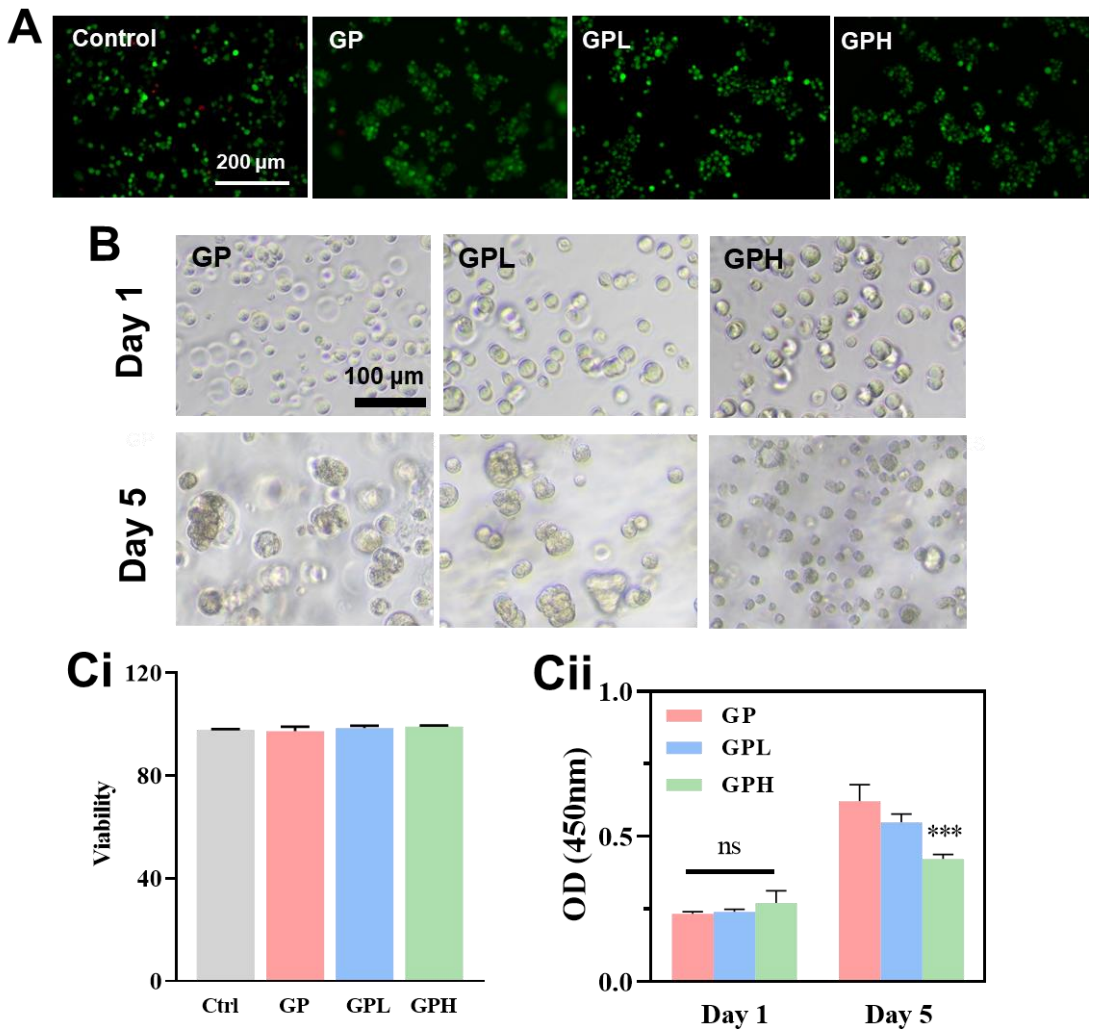

Figure 3.9 Biocompatibility of hydrogel. **(A)** Cell viability on 2D hydrogels. **(B)** Cell morphology in 3D hydrogels. **(C)** Cell viability on different hydrogels **(Ci)** and cell proliferation in different hydrogels **(Cii)**.

3.3.4 Effect of ES on neuronal differentiation

N2a cells was encapsulated in GP and GPL hydrogels. Then we exposed the cells to ES (100 mV/mm) to induce neuronal differentiation after 48 h of culture to demonstrate the effectiveness of the conductive hydrogel and ES on neuronal differentiation in a 3D environment. Using a confocal microscope, images of cell shape and differentiation in four distinct biological contexts were captured and are shown in **Figure 3.10**. After 7 days of incubation, phalloidin/DAPI staining was used to evaluate cell morphology. **Figure 3.10A** shows that the four distinct cell groups had different morphologies. N2a cells exhibited extending and branching processes that are characteristic of neurons. GFAP and Tuj-1, two distinct neuronal markers, were expressed by all neural cells, as revealed immunofluorescence labelling (**Figure 3.10B**). No discernible changes were found between GP with ES treatment and GP without. In contrast, compared with the GP group, the conductive hydrogel (GPL) demonstrated improved neuronal development with neuronal length extension and Tuj-1 (1.2-fold) and GFAP (2.5-fold) overexpression. Additionally, the GPL hydrogel with ES treatment could further support neuronal differentiation by increasing neurite outgrowth compared with the GPL groups (without ES). Neurite length, neurite quantity, and neurite extremity were determined by morphological examination of the cells in four separate groups (**Figure 3.10C**). Regardless of the ES treatment, N2a cells enclosed in a non-conductive hydrogel had the shortest neurites (about 100μm). On the other hand, N2a cells incubated in conductive hydrogel GPL showed significantly longer neurites (about 250μm). The combination of ES and conductive hydrogel might significantly extend

the length of neurite to 450μm. Increases in the number of neurite roots and extremities in the GPL+ES group were associated with increased neurite length. Four neuronal gene markers, including the stem cell protein marker nestin, astrocyte marker GFAP, premature neuronal marker Tuj-1, and mature neuronal marker MAP2, were used in RT-qPCR to examine mRNA expression in various groups to quantitatively evaluate neuronal differentiation. There was no discernible variation in the expression of neuronal genes in the non-conductive hydrogel with or without ES, as shown in **Figure 3.10D**. In contrast, the conductive hydrogel (GPL) with ES expressed GFAP (1.2-fold), Tuj-1 (1.2-fold), and MAP2 (2-fold) genes much more than those without ES. The overexpression of these markers suggests that the combination of the conductive hydrogel with ES treatment could enhance the differentiation of NSC or precursor cells into mature neurons. The conductive hydrogel may effectively transfer electrical signals to the encapsulated N2a cells, enhancing neuronal development. The development of highly induced neuron-like cells may be caused by increased protein expression in neuronal cells during ES treatment [223, 224]. Although the precise underlying mechanism remains elusive, it is postulated that this phenomenon involves intricate cellular and molecular processes. One hypothesis is that the conductive hydrogel and ES treatment can alter the ECM, leading to changes in the membrane receptors of the encapsulated cells. The change in the membrane receptors may activate certain signaling pathways, such as ERK and AKT pathways, which have been demonstrated to exert a significant influence on neural differentiation [60]. The activation of these pathways may then lead to the activation of transcription factors, which are proteins

that control the expression of genes involved in neural differentiation. The increased expression of neural marker genes, such as Tuj-1, GFAP, and MAP2, may then promote neurite outgrowth and branching, leading to the development of mature neurons. However, to comprehensively unravel the intricate mechanisms underlying the promotion of neural differentiation by the conductive hydrogel and ES treatment, further molecular experiments are imperative to provide valuable insights into the precise molecular pathways and molecular events involved.

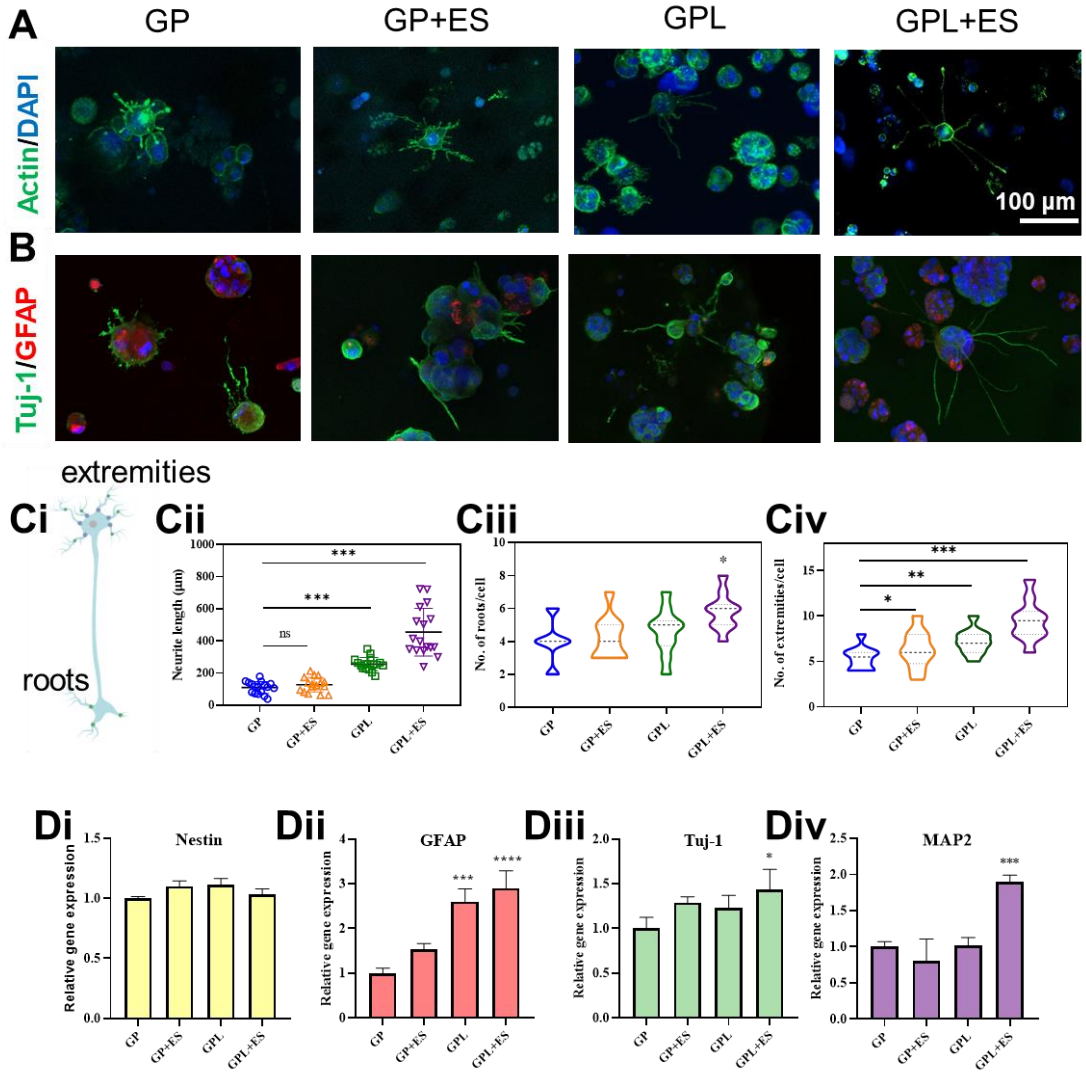

Figure 3.10 Effect of ES on neuronal differentiation. **(A)** Cell morphology by F-actin staining on day 7. **(B)** Immunofluorescence staining on day 7. **(C)** Morphology changes

in terms of neurite length, roots, and extremities. **(D)** Evaluation of day 7 gene expression associated with neuronal differentiation by RT-qPCR.

3.3.5 Effect of electrical intensity on neuronal differentiation

Different electrical fields (10, 100, and 1 V/mm) were delivered to N2a cells enclosed in 3D conductive hydrogels to maximise the electrical intensity of neuronal development. We observed from phalloidin/DAPI staining (**Figure 3.11A**) that the majority of N2a cells developed by extending their dendrites. Additionally, compared with the no ES treatment group, accelerated neurite outgrowth caused by ES was observed. As outlined in the preceding section, neuronal markers (GFAP and Tuj1) were examined by immunostaining using fluorescently labelled antibodies to learn more about N2a differentiation. Numerous N2a cells developed into astrocytes (GFAP) and neuronal cells (Tuj-1), as seen in the fluorescence microscope images (**Figure 3.11B**). Using ImageJ, neurite outgrowth was further evaluated regarding neurite length, number of roots, and neurite extremities (**Figure 3.11C**). Neurite counts and outgrowth significantly increased in the ES treatment groups. Meanwhile, the average length of neurites increased from 255μm to 454μm with an increase in the electrical field from 0 mV/mm to 100 mV/mm (**Figure 3.11Ci**), which agreed with the results of Patel *et al*. [225] and Lee *et al.* [214]. However, when applying a higher electrical field (1 V/mm), neither neurite length nor number showed a significantly increasing trend compared with the control test without electrical stimuli. RT-qPCR was also performed to quantify

gene expressions (GFAP, Tuj-1, and MAP2) for neuronal differentiation. Similar to other results, there was a significant increase in GFAP (2-fold), Tuj-1 (1.5-fold), and MAP2 (2-fold) gene expression with an increase in the electric field from 0 to 100 mV/mm. However, the downregulation of gene expression was observed under an extreme electrical field (1 V/mm). Similarly, Yamada *et al.* found a relatively low differentiation efficiency at high electrical fields [226]. This mechanism is not completely understood yet [200]. One explanation might be that low electric fields have a non-negligible impact on the cell steering mechanism, even under relatively high electric fields [227]. Considering the above results, we selected 100 mV/mm as the optimised electrical field for ES treatment in the following experiments.

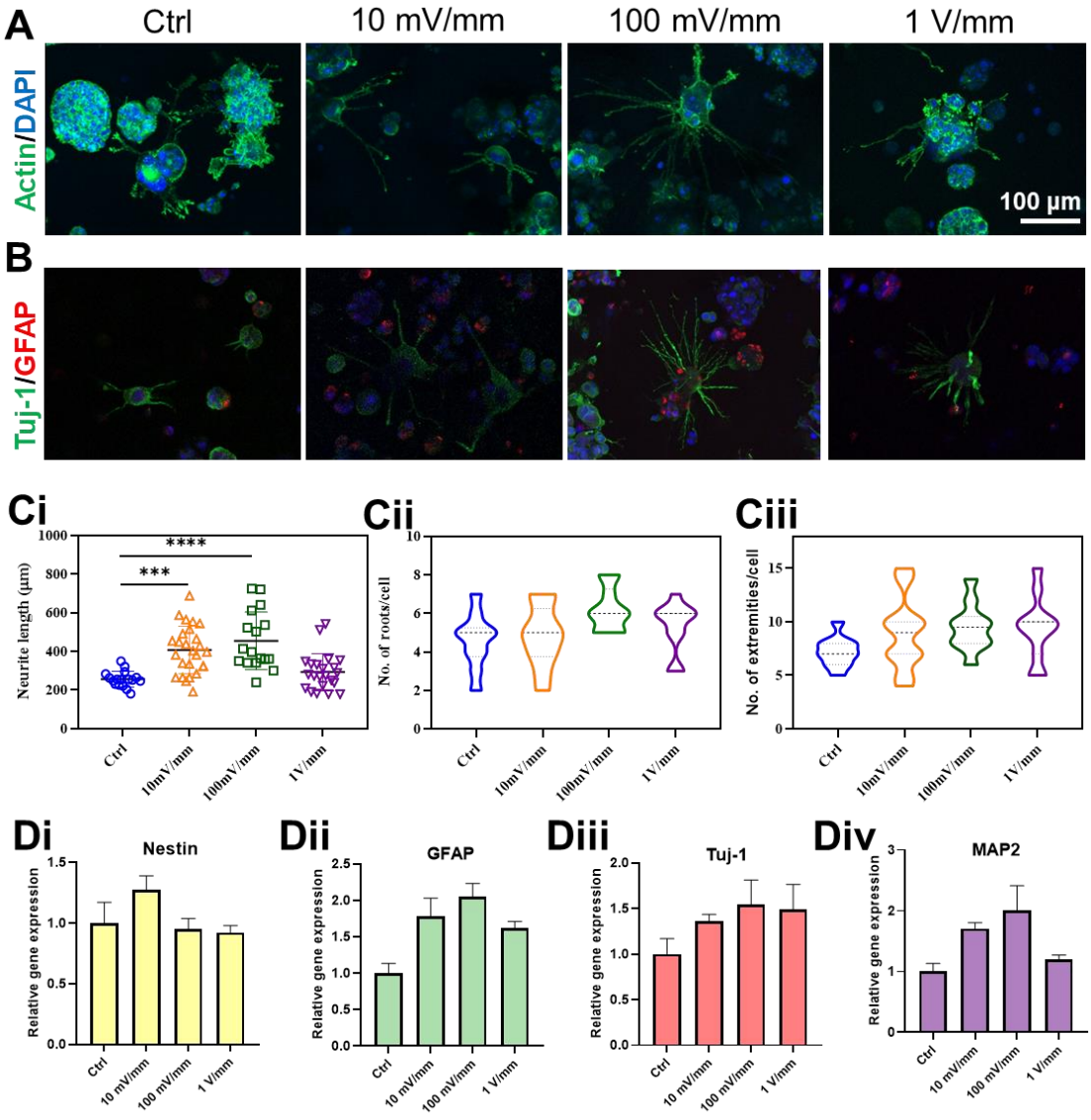

Figure 3.11 Effect of ES intensity on neuronal differentiation. **(A)** Cell morphology at different electrical fields by F-actin staining on day 7. **(B)** Immunofluorescence staining at different electrical fields on day 7. **(C)** Morphology changes in terms of neurite length, roots, and extremities. **(D)** Evaluation of day 7 gene expression associated with neuronal differentiation by RT-qPCR.

3.3.6 Effect of ES duration on neuronal differentiation

After optimising the electrical field of ES treatment, we investigated the effect of different ES treatment times on neuronal differentiation. A schematic of the ES treatment schedule with an electrical field (100 mV/mm, 100 Hz) is shown in **Figure 3.12A**. The efficiency of differentiation was evaluated using BF observation, F-actin staining, immunofluorescence staining, and RT-qPCR. As shown in **Figure 3.12B-C**, from the days 5 to 10, the number of differentiated N2a cells and the average neurite length increased significantly. However, there was no further significant increase between days 10 and 14. From the immunofluorescence images (**Figure 3.12D**), more N2a cells were observed to have differentiated into Tuj1-positive neuronal cells and GFAP-positive astrocytes with increasing culture time. To further obtain quantitative gene expression information, RT-qPCR was performed according to the above description on days 7, 10, and 14.

As shown in **Figure 3.12E**, the relative expression of NSC markers (nestin) and premature neuronal markers (Tuj-1) decreased from 1 to about 0.6 with the increase in culture time from day 7 to 14 as an increasing number of NSC differentiated into neurons and glial cells. Neurons gradually mature from the premature to mature stage. The astrocyte marker (GFAP) and maturing neuronal marker (MAP2) first increased from (reaching their maximum on day 10) and then decreased. The initial rise was the gradual maturation and stability of the neural network, while the later decline in gene expression showed signs of degradation of the neural network [228].

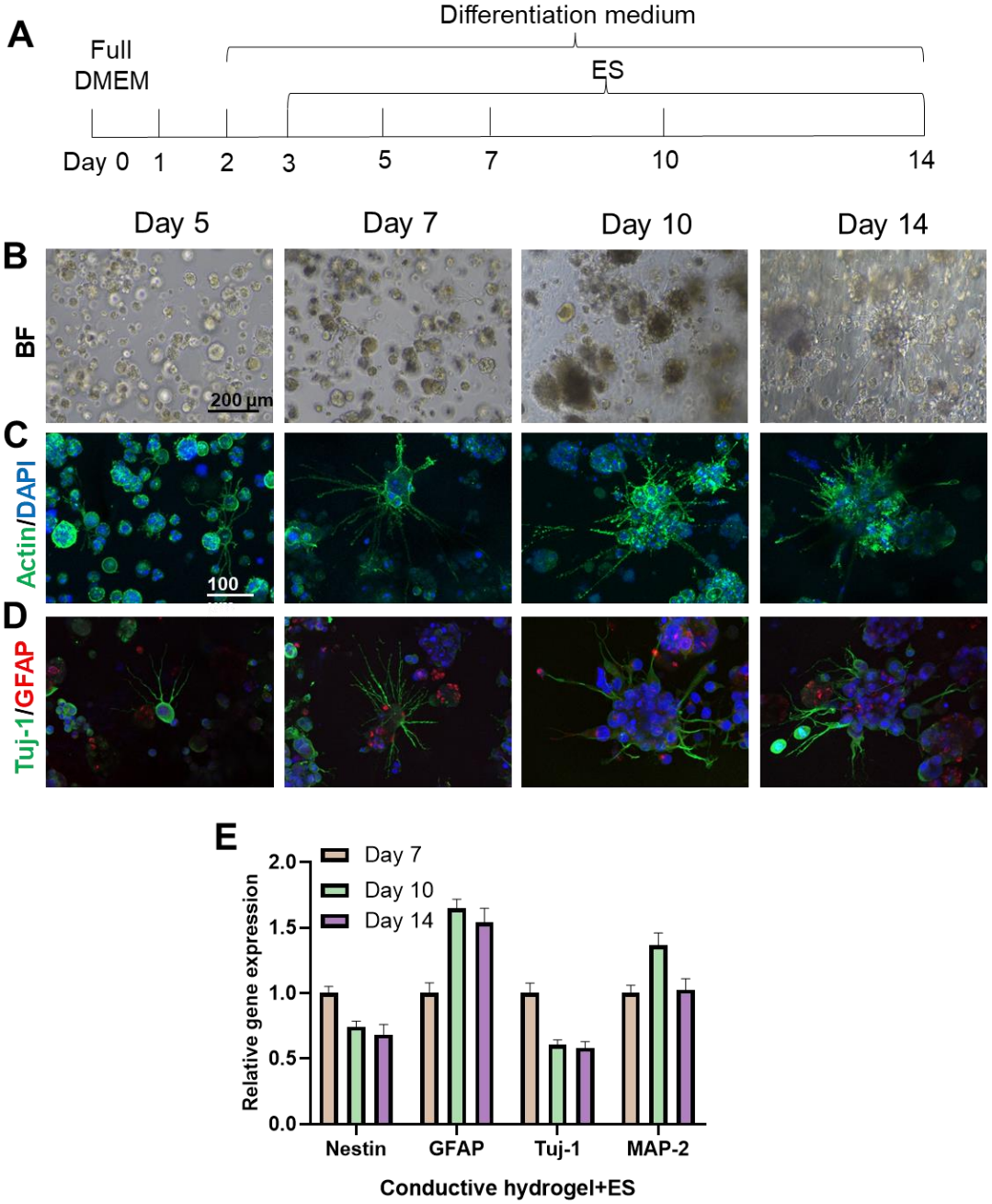

Figure 3.12 Effect of ES duration on neuronal differentiation. **(A)** Schematic of ES treatment schedule. **(B)** The BF cell morphology at different time points. **(C)** Cell morphology at different time points by F-actin staining. **(D)** Immunofluorescence staining at different time points. **(E)** Gene expression associated with neuronal differentiation by RT-qPCR at different time points.

3.3.7 Effect of ES and stretching on neuronal differentiation

To assess the total influence of ES and stretching, cells were tested under mechanical stretching (25% elongation) and ES (100 mV/mm, 100 Hz) co-stimulation. The morphology of the N2a cells under different conditions was evaluated by phalloidin/DAPI staining (**Figure 3.13A**). In addition, specific immunostaining with fluorescently labelled antibodies (GFAP and Tuj1) was used to assess N2a cell differentiation (**Figure 3.13B**). As depicted in the fluorescence microscopy images, more N2a cells differentiated into neuronal cells (Tuj-1) and astrocytes (GFAP) upon stimulation. In addition, independent of the ES treatment, the cells in the static control culture displayed a non-uniform distribution. However, under stress, N2a cells started to align in (i.e. parallel to) the direction of stretching.

Quantitative morphological characterisation in the four groups was further assessed in terms of neurite length, growth direction, number of roots, and neurite extremities using ImageJ (**Figure 3.13C-E**). Compared with the static control, significant increases in neurite outgrowth from 255μm to 635μm were observed under stretching and ES alone. The difference was that ES increased the number of roots and neurite extremities (increased by 30%), whereas stretching was more beneficial to the distribution of neuronal orientation and decreased filopodia density (15% reduction). This was similar to a study by Feng *et al*. [229], where large neurites grew preferentially towards the cell poles closest to the source of tension due to mechanical strain, thereby reducing the number of neurites. Notably, mechanical stretching plus ES increased the length more

efficiently than treatment with electricity alone, with significant differences. Similar to neurite length, higher filopodia density (number of neurite roots and extremities) and uniform distribution were observed in N2a cells under co-stimulation than in single stimulus and invariable control groups.

In neural cell types, qPCR was used to determine the impact of mechanical stretching and ES on the expression of neuronal differentiation markers. Similar to the immunofluorescence findings, stretching and ES alone dramatically increased the expression of genes supporting brain development (GFAP, Tuj-1, and MAP2) compared with the control group. Although stretching was more effective in enhancing Tuj-1 expression, ES was more effective in enhancing GFAP expression. As shown in **Figure 3.13D**, stretching (alone) increased the expression of GFAP and Tuj-1 by 1.3 and 1.9-fold, respectively, while ES (alone) increased the expression of GFAP and Tuj-1 by 3.5 and 2.3 fold, respectively. Compared with the control group or single stimulation alone, co-stimulation induced further upregulation of MAP2 (1.7-fold), Tuj-1 (2.6-fold), and GFAP (5.7-fold). Overall, these results show that ES and mechanical stretching can synergistically promote the neuronal differentiation of N2a cells and upregulate related genes. Furthermore, the precise mechanism of action of ES and stretching on neural differentiation can be studied by molecular experiments.

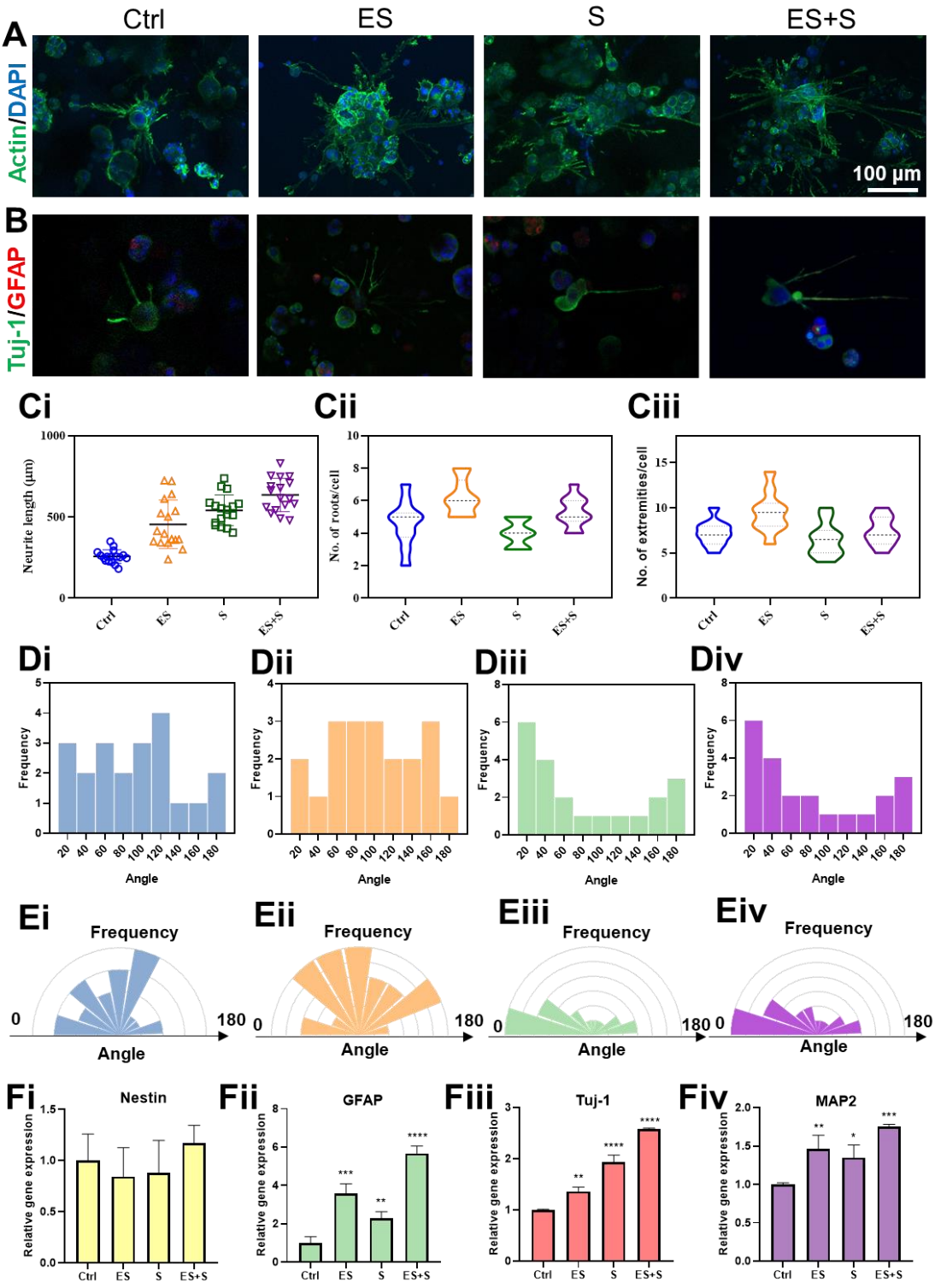

Figure 3.13 Effect of ES and stretching on neuronal differentiation. **(A)** Cell morphology with different stimulation conditions by F-actin staining. **(B)** Immunofluorescence staining with different stimulation conditions. **(C)** Morphology changes in terms of neurite length, roots and extremities. **(D)** Distribution of neuronal

orientation. **(E)** Rose diagram of neuronal direction. **(F)** Evaluation of day 7 gene expression associated with neuronal differentiation by RT-qPCR.

3.3.8 Electrophysiology evaluation

To determine the functional state of encapsulated N2a cells in the conductive hydrogel, the MEA System (Alpha MED Scientific Inc., Japan) was used to evaluate the electrophysiology. Before the measurements, the cells encapsulated within the conductive hydrogel were fixed on the probe through photo-crosslinking (**Figure 3.14A**).

3.3.8.1 Excitatory postsynaptic potential (EPSP)

EPSP was tested to capture the neuron action potential. As shown in **Figure 3.14B**, two random electrodes were stimulated, with action potential induction monitored in the responding electrodes. As shown in **Figures 3.14C-D**, connectivity of extracellular neuronal activities (EPSP amplitude and slope) was observed in N2a cells encapsulated in the conductive hydrogel, suggesting that there were healthy and functioning neurons in our 3D network model. In co-stimulation hydrogel conditions, neural activity (~1.7mV) was much greater than that in statically cultured conditions (~1mV) (Tai *et al.* [230]). Longer periods of hyperpolarisation and greater action potential induction may indicate more active neurons in the conductive hydrogel. Additionally, the increased response time of the modified nerve construct was probably due to the

increased interaction between neurons and glial cells during mechanoelectrical stimulation [231].

3.3.8.2 Spike

Important for neural activity, a spike is a short electrical pulse flow input at the dendrites to outputs at axon terminals [232]. In this study, neural spikes generated in N2a cells encapsulated in the conductive hydrogel were recorded using the MEA system. Spike sorting was used for synchrony analysis to extract a single activity from a multi-unit signal [233]. As shown in **Figure 3.14E**, multi-unit signals were extracted and classified using the Mobius software. Upon spike sorting, we identified four spikes, indicating four neighbouring neurons surrounding the probe. Compared with static cultures, the co-stimulated groups detected more connected neurons (more synergic spikes) in a network around the MEAs responding to the same stimulating signals. This synergic neuronal behaviour further demonstrated enhanced electroactivity by co-stimulation. Overall, the comprehensive mechanical and ES of conductive hydrogel specimens synergistically induced the differentiation and electrophysiological activity of N2a simultaneously, leading to tissues that were functionally competent engineered nerves.

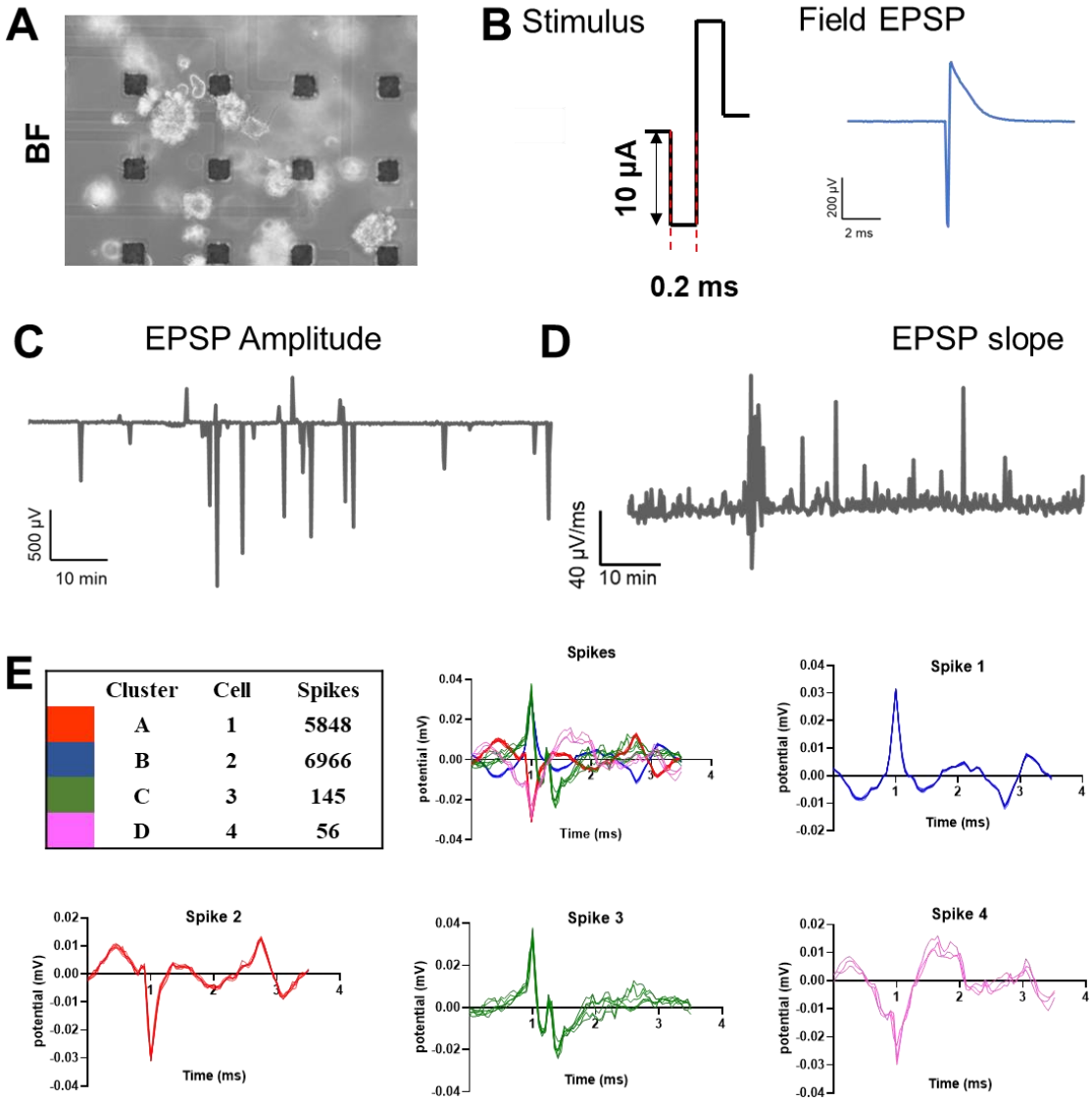

Figure 3.14 Electrophysiological evaluation of 3D neural network. **(A)** N2a cells cultured on MEA probe. **(B)** EPSP stimulated amplitude. **(C)** EPSP amplitude of 3D neural network. **(D)** EPSP slope of 3D neural network. **(E)** Spikes of 3D neural network.

3.4 Summary

Directed differentiation of NSC is of great significance in researching nerve regeneration and treating different types of injuries to the nervous system. Previous studies have demonstrated that neural growth factors and chemical molecules can promote the differentiation of NSC into nerve cells [234]. In addition, some studies have shown that physical cues (e.g., electrical and mechanical stimulation) can promote neuronal cell differentiation. This section studied the effects of ES and mechanical stretching on the differentiation of N2a cells in a 3D microenvironment.

Conductive GelMA-PEGDA hydrogels were first constructed, and their electrical conductivities and mechanical properties were assessed. Subsequently, we investigated the effects of ES on neuronal differentiation. According to our findings, the conductive hydrogel itself promoted the differentiation of neural cells, which was amplified further by ES. The effects of different electric field intensities on neuronal differentiation were studied to optimise the effect of ES. Consistent with Yamada *et al*. [226], we found that the optimal intensity occurred under an electric field of 100 mV/mm. Although some studies have shown a different electric field for stimulation, it may be related to the type and maturity of nerve cells [235, 236].

Further investigations of stretching and electrical co-stimulation were performed using a self-designed device. Consistent with previous research, stretching could also induce neuronal differentiation and promote neurite outgrowth, and directional alignment of

nerve extension was observed upon stretching stimulation [60]. The co-stimulation had synergetic effects on neuronal differentiation in terms of neurite outgrowth and filopodia density. In addition to changes in neuronal morphology, simultaneous co-stimulation can also affect neuronal gene expression. RT-qPCR results showed that co-stimulation improved the relative gene expression of neuronal differentiated genes (MAP2, Tuj-1, and GFAP), which play critical roles in neuronal development and function.

Overall, our study showed that ES and mechanical stretching could synergistically promote the neuronal differentiation of N2a cells and upregulate the expression of related genes. Using physical cues, this study enriches the existing literature on the directed differentiation of NSC within 3D microenvironments, allowing a better understanding of the effectiveness and feasibility of NSC therapies in the future.

Chapter 4 Host-guest self-healing hydrogel for bioprinting neural tissue mimics

4.1 Introduction

Currently, the inaccessibility of live human neural tissue and the inherent limitations of animal studies hinder studies on functions and disorders of the nervous system [128]. For decades, researchers have attempted to model NTMs *in vitro* to investigate the pathogenesis of neurological disorders [237], unfortunately, these studies usually investigated 2D substrates and were not accurately representative of the 3D microstructure and operation of neural tissues [238]. In previous chapters, 3D soft and elastic GelMA-PEGDA-based hydrogels were developed to study the mechanical and electrical microenvironment of neural behaviour in a 3D environment. Although GelMA-PEGDA hydrogels had excellent biocompatibility and tensile properties for the 3D stretching experiments in Chapter 2 and 3, they were static hydrogel networks formed by covalent bonds, which were fragile and could not fully mimic the dynamics of ECM composed of supramolecular chemistry [239, 240]. In addition, the nervous system is intricate and consists of many layers of tissue (e.g., multi-layered brain architecture of the human cortex, grey and white matter structure of the cylindrical spinal cord, and concentrically laminated fascicle structure of the peripheral nerve) [238]. The formation of 3D NTMs with desired shapes and functions is important for nerve regeneration applications.

Currently, 3D NTMs are typically obtained from neurospheres that spontaneously form during stem cell differentiation. However, these neurospheres do not have a specific complex shape and cannot be scaled up owing to diffusional limitations. In addition, constructing a freestanding 3D NTM with nerve function and electrical activity is also challenging when neural cells are seeded on the surface of 3D constructs [241]. Bioprinting, as an additive manufacturing technology, provides a promising technique for constructing *in vitro* neural models because it can replicate the mechanical, structural, and biological features of nerve tissues [242]. During the bioprinting process, bio-inks – which are the combination of biomaterials, cells, growth factors, and drugs – can be deposited layer-by-layer to fabricate tissue-like structures [243]. The 3D bioprinted neural mimics might develop neuronal circuits in their structures during development, giving them the capacity to react sensitively to stimuli.

The limitations encountered in bioprinting predominantly stem from the constraints associated with printable biomaterials. Numerous biomaterial inks, including PCL and PLA, exhibit unsuitability for bioprinting neural systems due to their ability to be printed solely in the form of polymer melts at elevated temperatures or polymer solutions dissolved in organic solvents [244]. Hydrogel bio-inks, such as gelatin, GelMA, and fibrin, have also been developed for bioprinting, which can be used to print fibroblasts but are unsuitable for printing nerves because of their greater sensitivity to the printing process [126]. Although our previously synthesized GelMA-PEGDA hydrogel has excellent biocompatibility for 3D cell encapsulation, it also lacks

sufficient rheological properties to be fabricated into 3D biomimetic neural tissue structures with controlled shape and size. Meanwhile, the lack of necessary functional groups of PEGDA makes it difficult to be further modified with desired properties. Thus, it is necessary to develop a new advanced bio-ink for bioprinting neural tissues.

The overall requirements for an ideal bio-ink for neural tissues are as follows [245]: 1) Biocompatibility: One of the most important key features for bioprinting tissues is to design a microenvironment that is adaptable with neural cellular activities (e.g. cell proliferation, migration, and differentiation). 2) Rheological Properties: Neural cells are highly sensitive to printing procedures. Generally, neural cells show low viability after printing with no proliferation or axon propagation owing to high-shear stress and lack of biological components. It is essential to process high-viscosity inks with the necessary printing pressure and accompanying shear forces to prevent damage to cell viability. 3) Mechanical Properties: The printed structures should be sufficient to maintain the desired 3D shape after printing, and be mechanically analogous to native nerve tissue (a few kPa) to provide structural assistance and signalling hints for cell behaviour.

Natural hydrogels, such as HA and gelatin, have been popular for neural tissue bioprinting. In contrast to synthetic hydrogels, natural hydrogels possess superior biocompatibility and exhibit notable biological activity, making them highly desirable for neural printing applications [246, 247]. As a key element of the ECM and an

important glycosaminoglycan in connective tissues (nerve, cartilage, vitreous humour, and synovial fluids), HA is essential for rheological and structural functions [248]. HA can also regulate neural proliferation, migration, and differentiation through interactions between certain cell receptors [249]. Furthermore, HA has been reported to enhance neural regeneration by organising the ECM into a hydrated open lattice for axonal migration [250]. Gelatin is a natural hydrogel with strong biocompatibility and low antigenicity [251]. Gelatin comprises a mixture of peptide sequences (RGD) that enhance cell attachment [252].

Regeneration failure occurs because conventional hydrogels for neural healing are generally fragile and are quickly destroyed by external forces. Considering the high demands on the rheological properties of bio-inks and the soft nature of nervous tissue, supramolecular reversible crosslinking was introduced into the hydrogel backbone. The fast self-healing property of the host-guest hydrogel could restore its functionalities and morphological and mechanical integrity after printing. In addition, the self-healing property has many advantages for developing neural tissues: 1) avoiding the potential risks of repeated rupture, 2) restoring its original properties after damage, and 3) protecting neural cells from high-shear stress upon printing [253]. Finally, host-guest interactions also provide a 3D biomimetic hydrogel with tenable dynamic properties to regulate cell behaviour and function, forming a united nervous network.

Among the host-guest molecules, β-cyclodextrin (CD) is the best-known host-guest

molecule due to its processable in water, appropriate affinity, and wide distribution in nature. CD has gained extensive utilization across diverse pharmaceutical industries and is widely acknowledged as being safe for its intended applications [254]. Furthermore, characterized by its cavity size of approximately 300 $Å^3$, CD possesses the capacity to encapsulate an array of hydrophobic guest molecules. Among these guests, adamantane (Ad) stands out as a notable representative due to its well-matched size and substantial affinity ($Keq \approx 10^5\ M^{-1}$), making it an exemplary choice for CD inclusion complexes [255]. In this chapter, a novel host-guest supramolecular hydrogel was investigated by grafting CD and Ad into two natural hydrogels, hyaluronic acid and gelatin.

While host-guest dynamic interactions provide hydrogels with shear-thinning and rapid self-healing properties to a certain degree, their mechanical strength remains inadequate for long-term stability and perfusion following bioprinting, primarily attributed to the inherent weakness of non-covalent bonds. However, a promising solution lies in the additional modification of hydrogels through a covalent photo-crosslinking mechanism, which imparts resistance against physical and chemical perturbations, thereby enhancing their overall mechanical robustness [256, 257]. To achieve this objective, the chemical grafting of double bonds into HA and gelatin macromers was accomplished using MA. Subsequently, host or guest moieties were introduced to modify the macromers, enabling the construction of double network structures. Within this dual network framework, the host-guest interactions facilitated reversible energy dissipation,

effectively shielding the covalent network from bond rupture and enhancing the overall mechanical resilience of the hydrogel system.

This chapter describes the development of a novel host-guest hydrogel bio-ink for constructing an NTM. First, host-guest hydrogels with good self-healing ability and printability were prepared. The host-guest interaction endowed the hydrogel with a large degree of design flexibility for developing a neural structure (grid, cube, and ring structure) through bioprinting. The neural cells maintained high viability, proliferation, and electrical activity in the printed structures. In addition, host-guest interactions provided a dynamic ECM environment that regulated cell behaviour (morphology, spreading, and migration) and the function of the neural system (electroactivity and signal transmission), forming a united neural network. These bioprinted neural mimics could be efficient models with great potential in neuroscience research for assessing neural functionality *in vitro*, thus helping improve disease study models.

4.2 Methodology

4.2.1 Preparation of host-guest hydrogel

4.2.1.1 Preparation of host hydrogel

Synthesis of HA modified with β-cyclodextrin (CDHA)

HA (Bloomage Biotech Co., Ltd., China, 290 kDa) modified with CD (Zhiyuan Biotech Co., Ltd., China) was synthesized by side-chain modification via an amide condensation reaction [258]. Briefly**,** 1-(3-Dimethylaminopropyl)-3-ethylcarbodiimide hydrochloride (EDC, Sigma-Aldrich, 383 mg) and N-hydroxysuccinimide (NHS, Sigma-Aldrich, 230 mg) were added into 60 mL PBS containing 290 mg HA, and stirred for 30 min at 25°C. 10 mL PBS containing 120 mg of CD was then added to the above solution, and stirred for 24 h at 25°C. After a 3-day dialysis of deionized (DI) water and a freeze-drying process, CDHA was successfully obtained as a white powder. The degree of substitution of the target CDHA was determined by ^{1}H-NMR (JEOL ECZ500R 500 MHz), according to a previous study [254].

Synthesis of methacrylated HA (MeHA)

MeHA was synthesized using the conventional MA route, as described in a previous study [257]. Briefly, 290 mg of HA was dissolved in 60 mL DI water at 4°C. After adjusting the solution pH to 8.5, 0.32 mL of MA was added. The reaction was allowed to proceed for 8 h, while carefully maintaining the pH at 7.5–8.5 using 1 M NaOH. Then, an additional 0.16 mL of MA was added, while meticulously maintaining the pH

within the range of 7.5–8.5 for another 4 h. Subsequently, the solution was adjusted to pH 7.0 and subjected to dialysis against an abundant volume of water for 3 days. After that, the solution was filtered and subjected to freeze-drying at -80°C, resulting in the obtainment of dry MeHA. The DS was determined using ^{1}H-NMR.

Synthesis of CDMeHA

HA modified with methacrylate and β-cyclodextrin moieties (CDMeHA) was prepared using a procedure similar to that described above. MeHA was used as the base material instead of HA. CDMeHA was synthesised using sequential combinations of these processes.

4.2.1.2 Preparation of guest hydrogel

Synthesis of Amantadine-modified gelatin (Ad-gelatin)

Amantadine modified gelatin was obtained by the reaction of carboxylic groups on gelatin with amine groups [259, 260]. In brief, EDC (335.4 mg) and N-NHS (201.4 mg) were added to a solution of gelatin (300 mg) in 60 mL PBS (pH=6), and the solution was agitated for 30 min at 50°C. Subsequently, 60 mg of Ad (Sigma-Aldrich) was added to the combination described above. At 50°C, the solution was agitated for 12 h. Then, the solution was filtered and dialyzed for three days against an excess of DI water. After lyophilization, the functionalized Ad-gelatin was successfully obtained. The increasing C/N molar ratio determined the DS through elemental analysis (Vario EL III) [261].

Synthesis of Amantadine-modified GelMA (Ad-GelMA)

Ad-GelMA was synthesized according to our previously method [262]. Briefly, 300 mg Ad-gelatin was fully dissolved in 60 mL PBS at 50°C for 30 min. Then 0.03 mL of MA was dropped into the above Ad-gelatin solution. The solution was agitated for 12 h at 50°C, dialyzed against water for three days, and freeze-dried to yield functionalized Ad-GelMA [164, 170, 261].

4.2.1.3 Host-guest hydrogel formation

Host-guest hydrogels were fabricated through the process of host-guest self-assembly. The host hydrogel solution (CDMeHA) and guest hydrogel solution (Ad-GelMA) were combined and subjected to heterogeneous mixing through stirring. Subsequently, any remaining air was eliminated via centrifugal separation. Host-guest hydrogels with varying concentrations were prepared to enable subsequent characterization and analysis.

4.2.2 Physicochemical characterization of host-guest hydrogels

4.2.2.1 Mechanical tests

The mechanical tests of the hydrogels were conducted on a dynamic universal mechanical system. Dumbbell-shaped hydrogel samples were prepared for the tensile test, while cylindrical samples were prepared for the compression test [211].

4.2.2.2 Swelling experiment

To ascertain the effect of crosslinking on the hydrogels, cylindrical samples (d=10 mm, h=3 mm) were subjected to swelling test at room temperature [170]. The ability of the hydrogels to swell was assessed by determining the weight change of samples submerged in PBS at various periods through **Eq. 2.1**.

4.2.2.3 Viscosity test

Hydrogels of varying compositions were placed through their paces in a rheometer (MCR 702) with temperature control features and a parallel plate measuring 25 mm in diameter. The viscosity of hydrogel solutions was assessed using a shear rate range of 0.1 s^{-1} to 1000 s^{-1} at 37°C.

4.2.3 Rheological and printability characterisation

4.2.3.1 Rheological characterisation

Rheological characterisation was performed using a rheometer (MCR 702) fitted with a cone and plate geometry facility with a diameter of 50 mm, 0.995° cone angle, and 27-µm gap. The rheological performance was measured under 37°C with different oscillatory frequencies (0.01 to 100 Hz with 1% strain), oscillatory time, and oscillatory strain (0.01 to 300% strain at 30 Hz). The shear force test was measured at 300% strain with recovery at 1% strain at 30 Hz, and a continuous flow test was performed under a linear shear rate from 0 to 10 s^{-1}.

4.2.3.2 Bioprinting process

A commercial extrusion 3D printer (ALPHA-CPD1, SUNP) was employed for 3D bioprinting. The design of the printed CAD models was accomplished using standard software, and during the printing process, a G-code was generated based on the STL files to facilitate hardware control. Notably, the G-code allowed for the convenient adjustment of parameters such as extrusion flux, printing speed, as well as distance and thickness between layers. Subsequent to the printing procedure, the printed structure was subjected to UV light to ensure the stabilization of the entire construct.

4.2.3.3 Injectability

To investigate the injectability of the host-guest hydrogel, it was injected into a PolyU mould overlapped by glass sides. After photo-crosslinking with UV, a PolyU logo-shaped hydrogel was obtained.

4.2.4 Characterisation of self-healing ability

Color-alternating hydrogel columns and rings served as a visual representation of the host-guest hydrogel's self-healing capabilities. First, the host and guest hydrogels were dissolved in DI water. The host and guest hydrogels were then mixed to prepare the host–guest hydrogel and stained in two different colors. Next, the crosslinked host–guest hydrogel was cut into several parts using a scalpel. Two supramolecular hydrogels were connected along the incision. After a few minutes, the self-healing hydrogels were

torn apart using tweezers to examine their self-healing status. The hydrogels were monitored as they healed over a range of time. Hydrogels of various hues were prepared using rod-shaped vials, according to the procedures described above. Identical chunks of the hydrogel were sliced off and reassembled individually until they formed a single column. Hydrogels made in the shape of a column were manipulated into semicircles or circles.

Experiments on host hydrogel shear recovery were performed at 37 °C on a rheometer with 12-mm diameter parallel plates. Shear-thinning was achieved at 10 Hz, 250% strain and recovery at 0.5% strain. The continuous step strain was changed every 50 s throughout each strain period.

4.2.5 Cell culture and characterization

4.2.5.1 Cell culture

PC12 (High differentiation, ATCC, USA), a cell line obtained from a pheochromocytoma of rats, was used in this project instead of N2a [21]. The highly differentiated PC12 cells exhibit high electroactivity, increasing the likelihood of generating functional networks while the differentiation of N2a cells within the host-guest hydrogel is expected to be limited to the formation of interconnected functional neural networks. PC12 cells were cultivated using a full growth media (RPMI-1640 + 10% FBS). The medium was refreshed every 2 days during cultivation [263].

4.2.5.2 Live/dead staining

Using the manufacturer's guidelines, a live/dead test was used to determine the viability of PC12 cells. Each sample was incubated at 37°C for 15 min after treatment with a live/dead solution containing 4 mmol/L ethidium homodimer-1 and 2 mmol/L calcein AM in PBS.

4.2.5.3 Phalloidin/DAPI staining

Hydrogels samples encapsulated with PC12 cells were fixed with 4% paraformaldehyde, permeabilised with 1% Triton for 20 min. The samples were then incubated in the dark with phalloidin solution for 45 min, followed by DAPI solution for 5 min. After rinsing thrice in PBS, the samples were placed under a fluorescence microscope for analysis.

4.2.6 Analysis of neuronal migration in the hydrogels

The migration of neuronal cells plays a crucial role in neural tissue regeneration. To evaluate neuronal cell migration in host-guest hydrogels and neural tissue regeneration *in vitro*, a neuronal migration model was constructed, as shown in **Figure 4.1**. Four different hydrogels (GelMA, host hydrogel, guest hydrogel, and host-guest hydrogel) were selected for the migration test. First, four hydrogel PC12 cell suspensions (5×10^6 cells/mL) were prepared. Subsequently, 90 μL of PC12 cell-loaded hydrogel was added

to the left of the mould (blue area h=1 mm) and exposed to UV for 10 s for crosslinking. Then 90 µL of corresponding cell-free hydrogel (the same type of hydrogel as the cell-loaded hydrogel) was added into the red area of the mould. Subsequently, the whole mould (blue and red areas) was exposed to UV (365 nm, 4 mW/cm^2) for another 60 s to be crosslinked into one. Finally, the migration of cells from the different hydrogels was observed under a microscope.

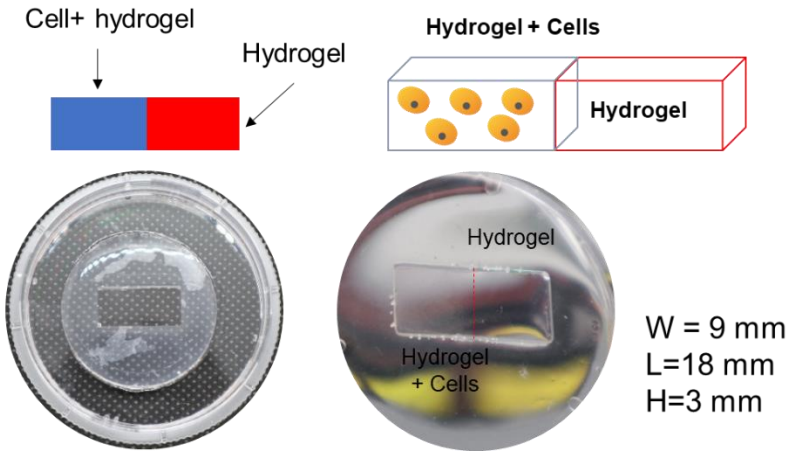

Figure 4.1 Neuronal migration mould for cell migration experiments. The migration of PC12 cells in different hydrogels was evaluated using a ZEISS confocal microscope. Using confocal microscopy, 400-µm thick Z-stack projections of each interface were acquired.

4.2.7 Gene expression

According to the literature, RT-qPCR was used for quantitative gene expression [178]. Collagenase type II was used to break down and liberate the 3D cells encapsulated in hydrogels. Using a Total RNA Kit total RNA was isolated from PC12 cells. A Prime Script RT Master Mix Kit was used to reverse-transcribe the extraction into cDNA. As

an internal control, GAPDH was employed to standardize the findings. **Table 4.1** lists the sense and antisense primer sequences used for a group of related genes. The $2^{-\Delta\Delta Ct}$ technique was used to determine gene expression.

Table 4.1 Primer sequences used for RT-qPCR

Genes	Sequences
F-actin	F: 5'-CGGCAGGCGGGTACAAG-3'
	R: 5'-TCTCTGCCTTCTGTGACACG-3'
Myosin	F: 5'-ACTATGCAGGCAAGGTGGAC-3'
	R: 5'-CTGAGGACTGGTGAAGCAGG-3'
FAK	F: 5'-GCTTAATCTGGCCAGGACGG-3'
	R: 5'-TGAAGCACGGTTTGAGAGGT-3'
Vinculin	F: 5'-TCACCTCCTGGGATGAGGA-3'
	R: 5'-TGGCCTGGTTCAGTTTCGAG-3'
Integrin	F: 5'-AATGCCCTGAAGCCAAGTGT-3'
	R: 5'-GGCTGGTATTCCTGCTGC-3'
GAPDH	F: 5'-GGCTGCCTTCTCTTGTGACAA-3'
	R: 5'-TGCCGTGGGTAGAGTCATACTG-3'

4.2.8 Bioprinting of cell-laden host–guest hydrogels

The host–guest hydrogels were dissolved in a 0.5 wt% LAP solution in the culture medium. To ensure sterility, the resulting solution underwent filtration. Then, PC12 cells (1×10^6 cells/mL) were thoroughly mixed with the aforementioned hydrogel solution, resulting in the formation of cell-laden hydrogel constructs. The mixture was then injected and printed using a printing needle (25G). After printing, the printed structure was crosslinked under UV light (365 nm, 4 mW/cm^2), washed with PBS, and cultured in a complete growth medium. After culturing for 1 and 5 days, the cells in the 3D hydrogel were stained for observation.

4.2.9 Electrophysiology evaluation of neural regeneration model *in vitro*

Fluo-4 (F14201, InvitrogenTM) was used to capture the spontaneous neuronal activity. In short, Hanks' Balanced Salt solution (HBSS, Sigma-Aldrich) was mixed with 0.1% Pluronic® F-127 and 3mM fluo-4 AM (reconstituted in dimethyl sulfoxide (DMSO)). There was a 6 min incubation period at 37°C during which the cells were loaded with Fluo-4 AM. Following incubation, the PC12 cells were rinsed with HBSS and kept in the dark until data were captured. Visual examination and fluorescence imaging were performed using a fluorescence microscope (Nikon, Japan). As previously reported, potassium chloride (KCl, Sigma-Aldrich) was used to stimulate certain samples after baseline recording was made [115]. ImageJ was used to extract the areas of interest and monitor the changes in fluorescence intensity over time from the generated recordings. The ImageJ Image Stabilizer was used to fix the drift [264], and the changes in intensity (dF/F) were determined using previously outlined methods [265, 266].

4.3 Results and discussion

4.3.1 Preparation and chemical characterisation of host-guest supramolecular hydrogels

4.3.1.1 CDHA

The structure of CDHA was confirmed by ^{1}H-NMR. As can be seen from the ^{1}H NMR spectra of the CDHAs in **Figure 4.2**, CD had a characteristic peak at approximately 5.1 ppm. The DS was calculated by comparing the integrated peak area of CD (H1 proton δ=5.1) with the integrated peak area of HA (methyl singlet δ=2.1). Upon calculation, the degree of substitution for CDHA was found to be approximately 20%.

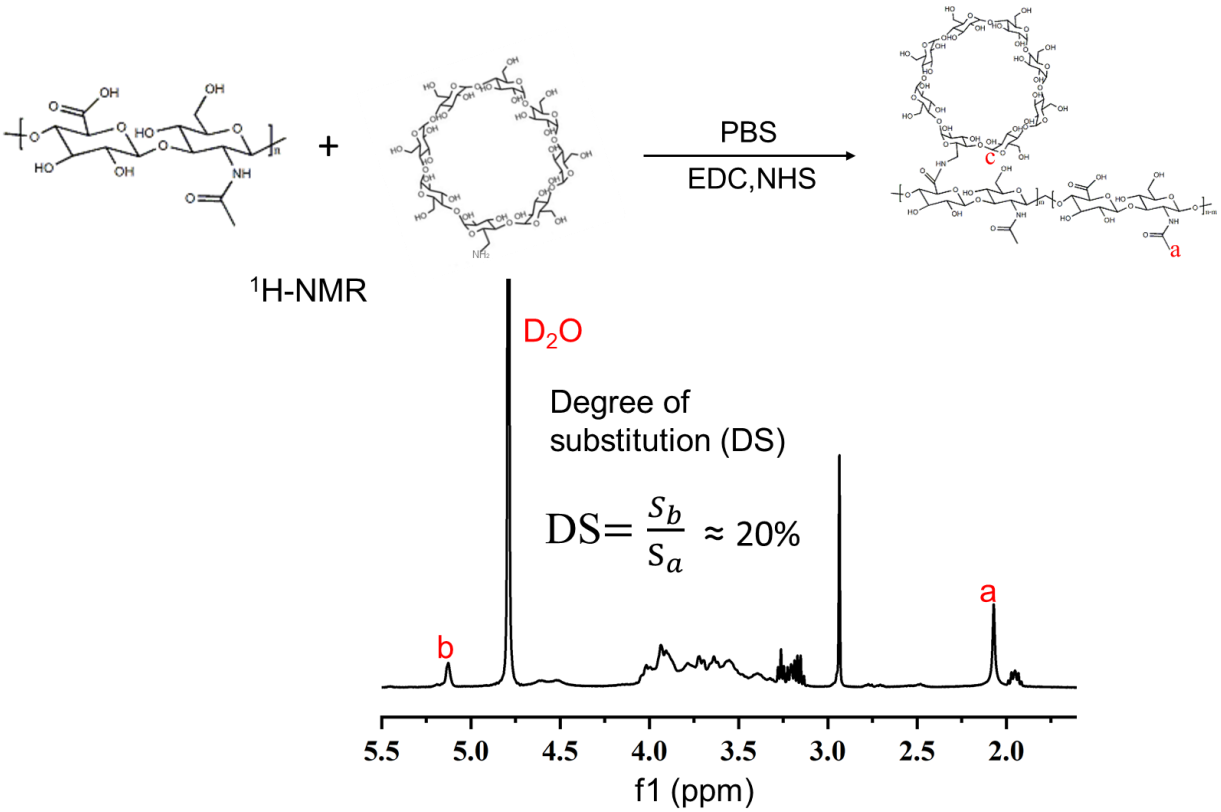

Figure 4.2 The chemical structure and ^{1}H-NMR spectra of synthesised CDHA.

4.3.1.2 MeHA

The structure of MeHA was also confirmed using ^{1}H NMR spectroscopy. As can be seen in **Figure 4.3**, the characteristic peaks of the vinyl group at approximately 5.7 and 6.2 appeared. The DS of MeHA was further determined by comparing the integrated peak area of the two vinyl protons with the integrated peak area of HA. A substitution degree of 3% was obtained.

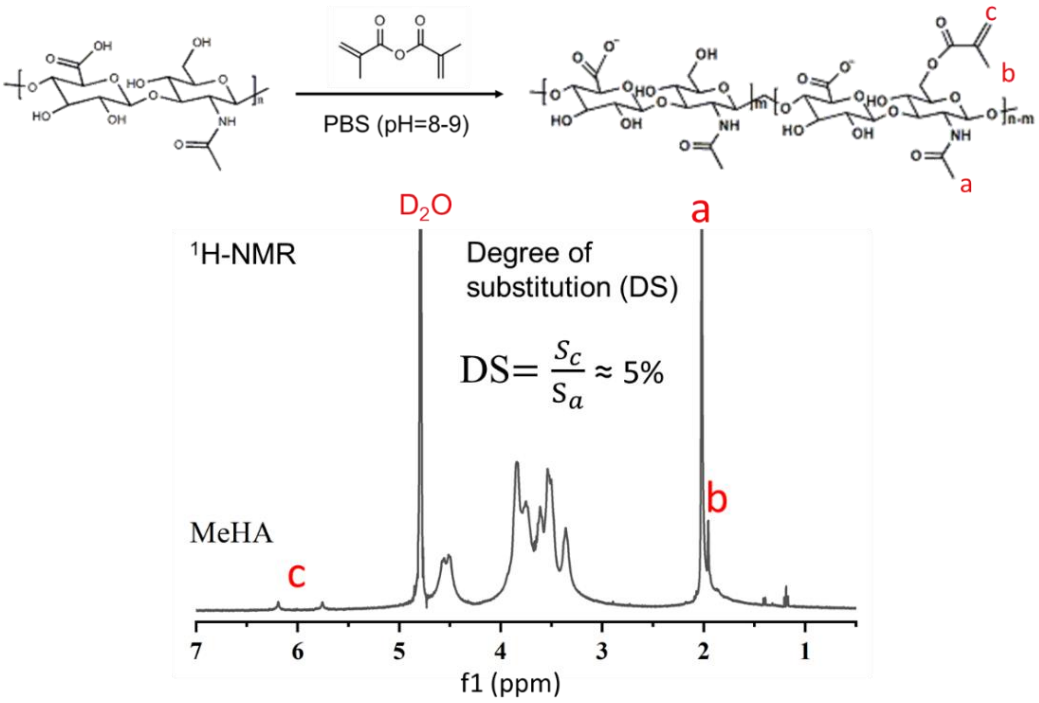

Figure 4.3 The chemical structure and ^{1}H-NMR spectra of synthesised MeHA.

4.3.1.3 CDMeHA

In the ^{1}H-NMR spectrum of CDMeHA (**Figure 4.4**), the characteristic peaks of both CD and vinyl groups appeared on the HA backbone, suggesting the successful synthesis of CDMeHA.

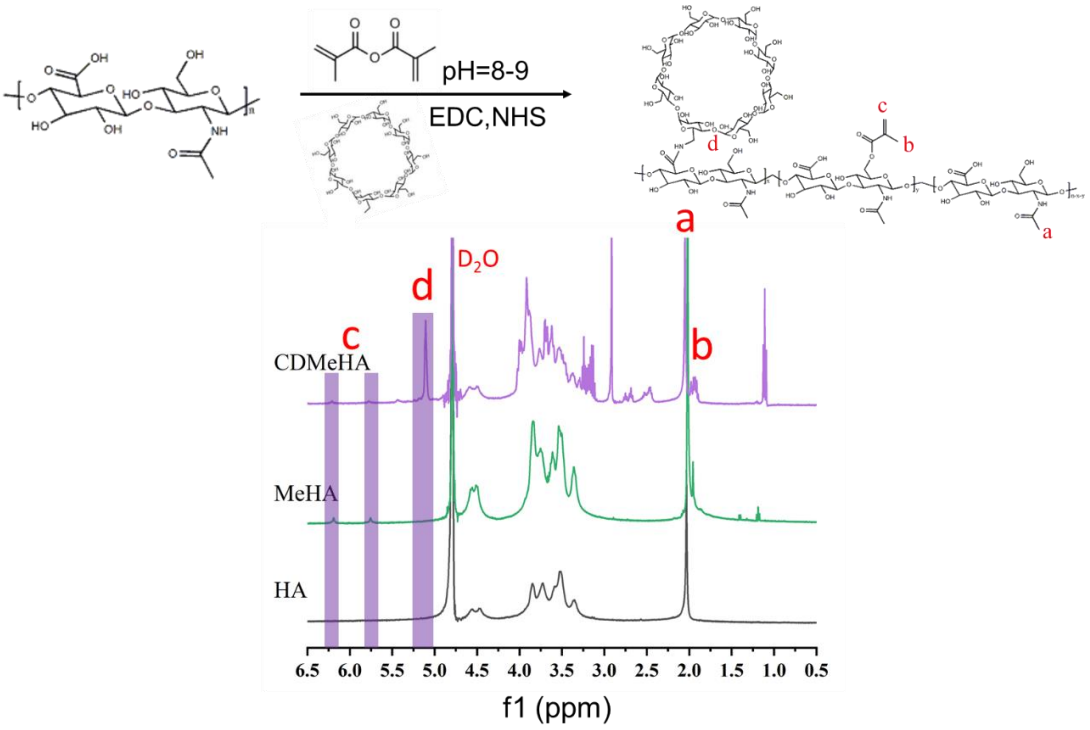

Figure 4.4 The chemical structure and ^{1}H-NMR spectra of synthesised CDMeHA.

4.3.1.4 Ad-gelatin

In the ^{1}H-NMR spectra of Ad-gelatin (**Figure 4.5**), a new peak was observed at 3.4 ppm, probably caused by a chemical shift due to the amide reaction between amide on amantadine and carboxyl on gelatin. The synthesis was further confirmed by elemental analysis (Vario EL III). As can be seen in **Table 4.2**, the C/N ratio increased from 3.20 (gelatin) to 3.33 (Ad-gelatin) owing to a higher C/N mole ratio of Ad (C/N=10). The degree of substitution could also be roughly calculated by elemental analysis to be approximately 20%.

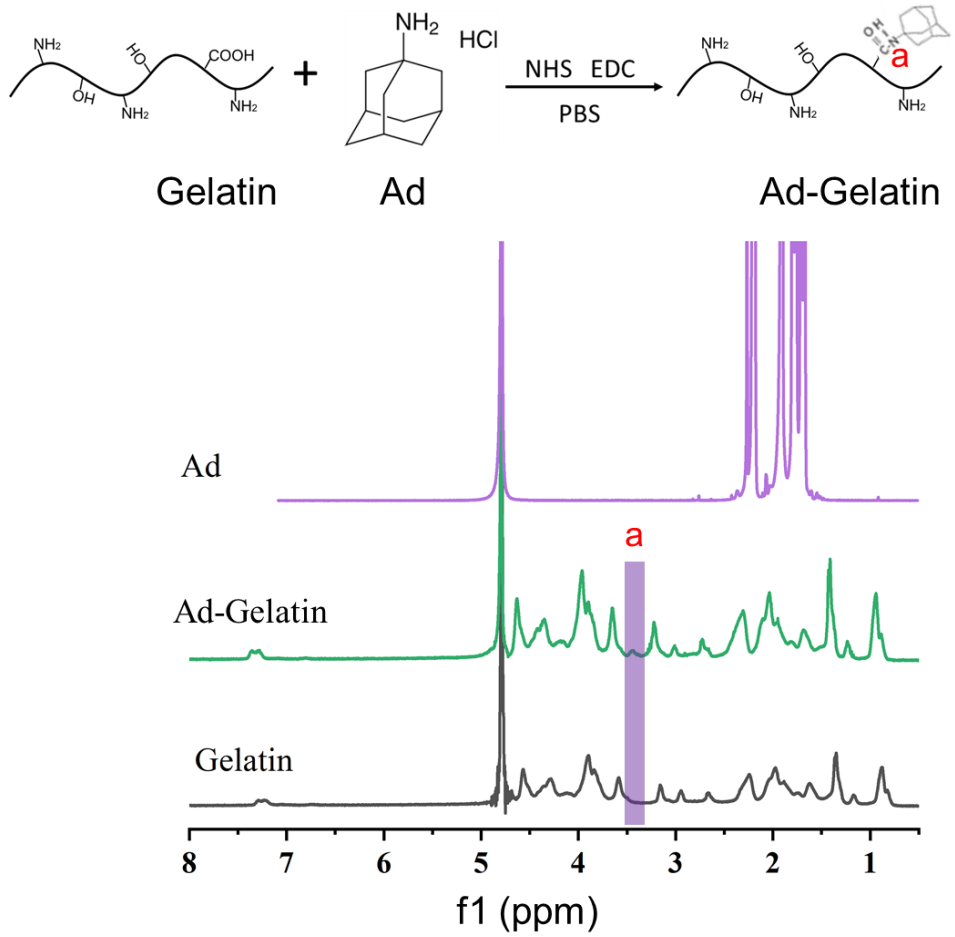

Figure 4.5 The chemical structure and ^{1}H-NMR spectra of gelatin, Ad-gelatin, and Ad.

Table 4.2 The element analysis results of gelatin and Ad-gelatin

Sample	C content (%)	N content (%)	H content (%)	C/N ratio	C/N mole ratio
gelatin	44.17	16.11	6.23	2.74	3.20
Ad-gelatin	47.21	16.52	6.56	2.86	3.33

4.3.1.5 Ad-GelMA

The ^{1}H NMR spectra of Ad-GelMA are shown in **Figure 4.6**. The characteristic peaks of both amantadine (3.4 ppm) and MA (5.36 and 5.64 ppm) were observed.

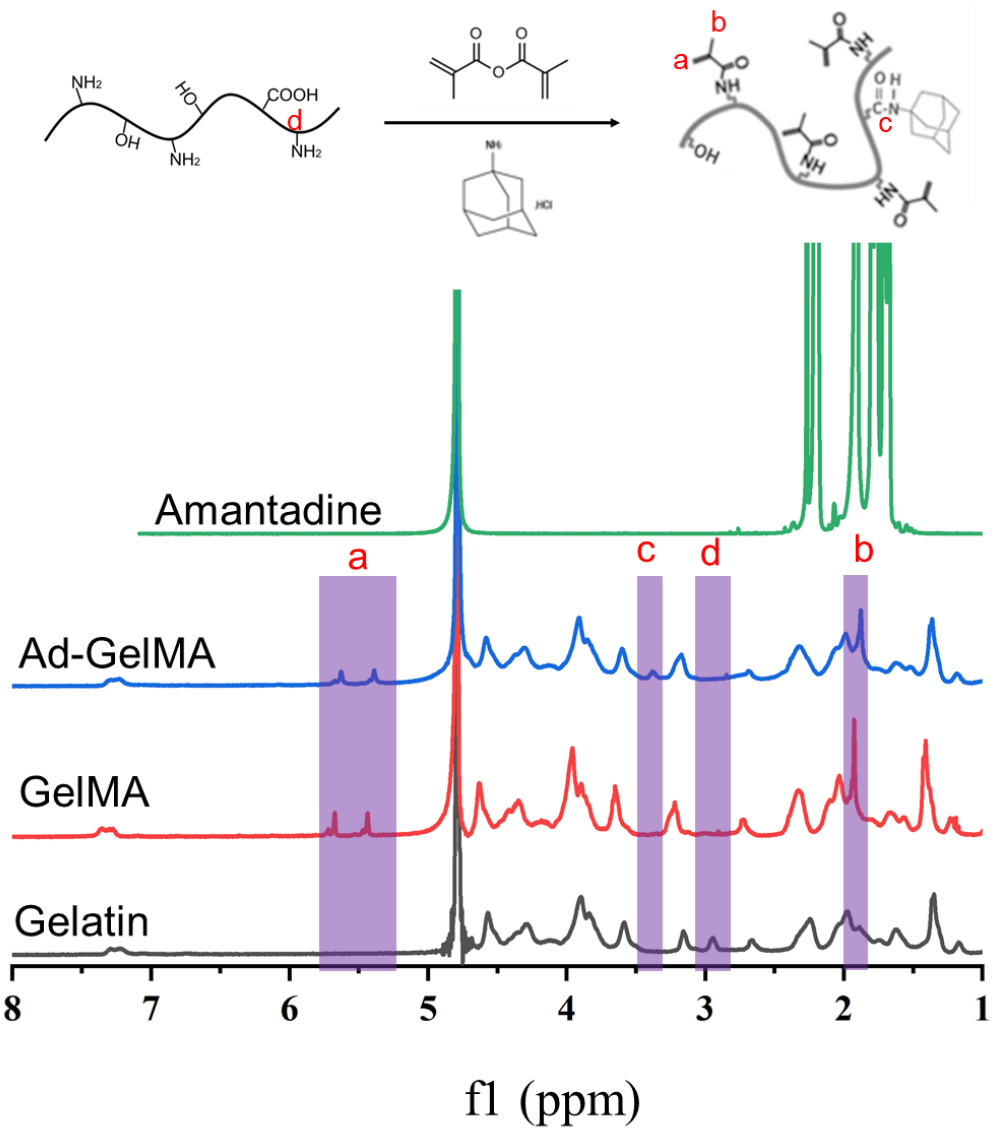

Figure 4.6 The chemical structure and ^{1}H-NMR spectra of gelatin, GelMA, Ad, and Ad-GelMA.

4.3.2 Host-guest interaction and self-healing ability

4.3.2.1 Host-guest interaction

When host and guest hydrogel solutions were mixed, a pseudoplastic hydrogel was immediately formed through the self-assembly of reversible host and guest moieties.

The formation and mechanisms of host-guest interaction are shown in **Figure 4.7A**. Compared with the flowable liquid in the individual host or guest solutions, the fabricated hydrogel was more stable in the qualitative inversion test (**Figure 4.7B**). Furthermore, according to the oscillatory rheology results (**Figure 4.7C**), the moduli increased significantly after mixing the host-guest hydrogel.

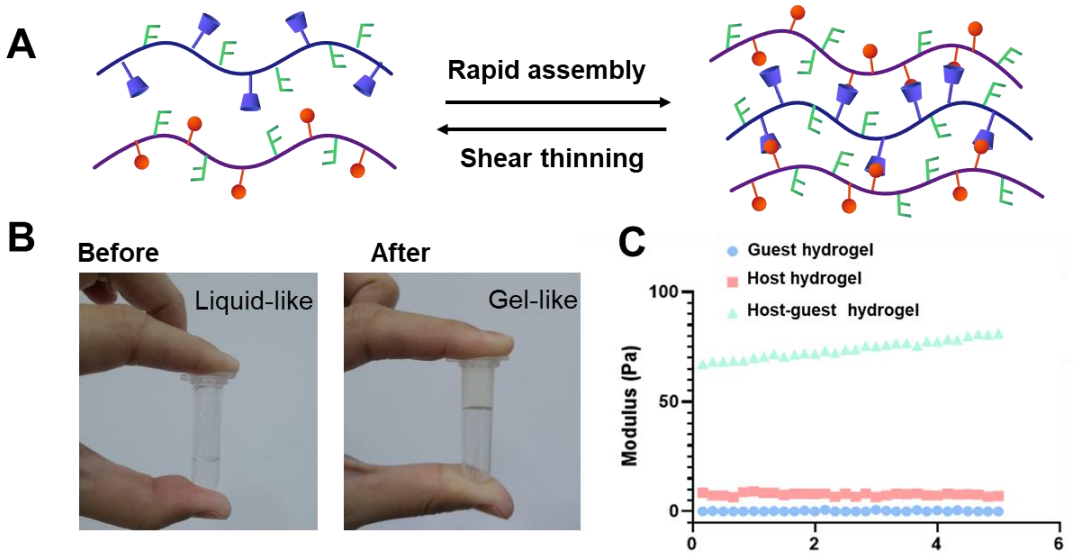

Figure 4.7 (A) Schematic of the dynamic formation procedure and host–guest interaction mechanisms. **(B)** Images of host-guest interaction (liquid-like before mixing and gel-like after) and **(C)** Modulus changes before and after mixing host-guest hydrogel.

4.3.2.2 Recovery and self-healing

Because the host-guest interactions were reversible, the host-guest hydrogels possessed rapid self-healing ability. In this part of the study, the recovery ability of the obtained hydrogels was tested under cyclic large and low-amplitude oscillatory strains. The yield stress of the hydrogel was examined using the strain sweep test from 0.5% strain to 300%

strain to determine the recovery ability, presented in **Figure 4.8Ai**. The storage modulus G′ and loss modulus G″ exhibited similar values (~200Pa) at low strain, and G′ decreased dramatically (~100Pa) at a large strain of 100%, suggesting the host-guest interaction had completely collapsed. Meanwhile, the self-healing ability of the host-guest hydrogels was evaluated by the alternate step strain test (low stain=1% strain; high stain=300%), as illustrated in **Figure 4.8Aii**. The hydrogel displayed a significant downward tendency in moduli under cyclic deformation, and a concurrent gel-sol transition was observed at high strain (300% strain). Meanwhile, fast recovery was observed when the strain conditions were converted from high to low within seconds. Similar results were also obtained regardless of how many cycles are run, indicating that the hydrogels could recover almost immediately after shear thinning.

To further observe the self-repairing ability of host-guest hydrogels from a macro perspective, the photo-crosslinked hydrogels were dyed in different colours and cut into halves (**Figure 4.8B**). The evolution process of diffusion is shown in **Figure 4.8Bi**. The diffusion efficiency of the host-guest hydrogel was higher than that of GelMA hydrogels. Fast and efficient permeability is an important factor in using hydrogels for tissue engineering, demonstrating that the created self-healing hydrogels may be used in biomedicine [267, 268]. Meanwhile, these cut pieces of host-guest hydrogel could easily interconnect and form an integrated hydrogel after close contact compared with that of GelMA in microscopy images (**Figure 4.8Bii**). To confirm the self-healing ability of the host-guest hydrogel, we used a tweezer to lift the self-healed hydrogel

from one side without breaking the healed incision. In addition to self-healing properties, the hydrogels exhibited excellent flexibility in connecting blocks alternately into columns and rings (**Figure 4.8C**).

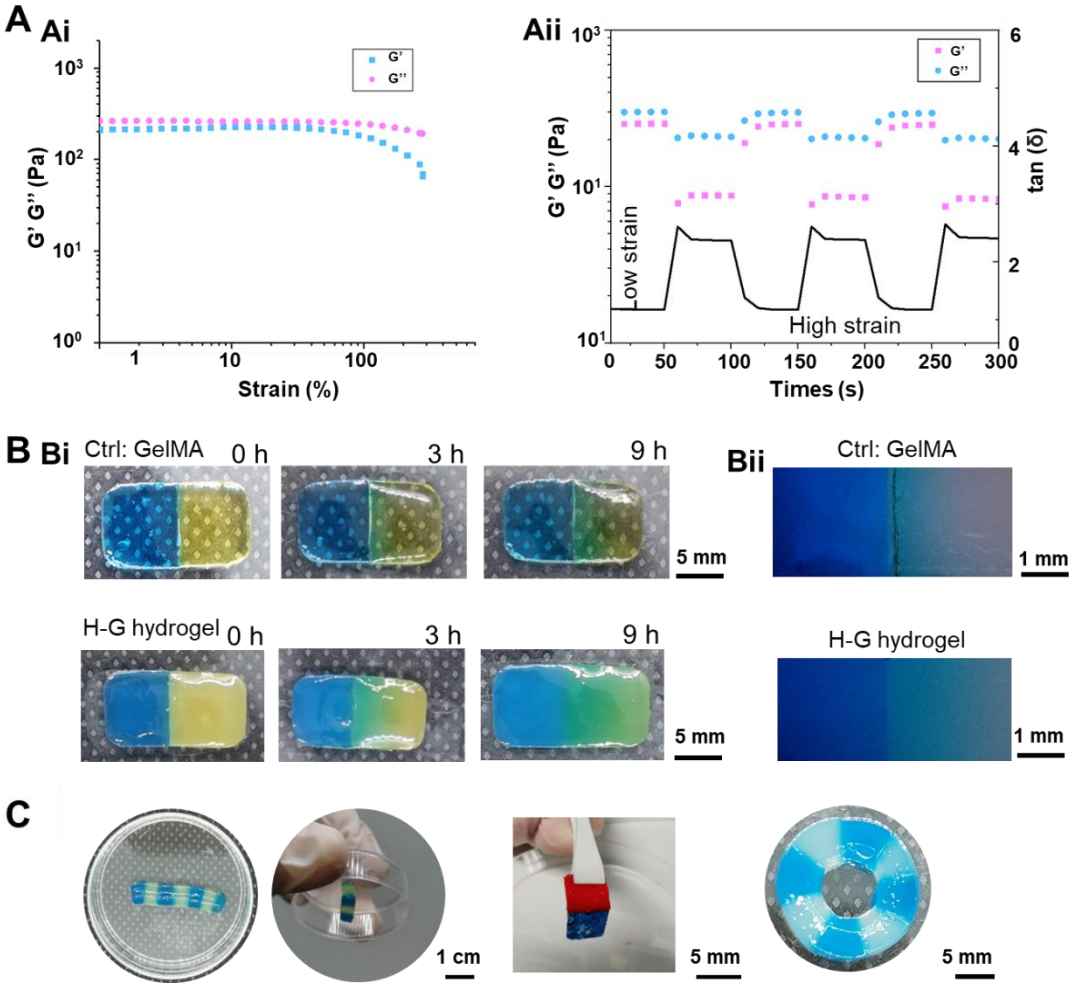

Figure 4.8 (Ai) The strain sweep cures for the host-guest hydrogel. **(Aii)** Cyclic recovery cures for host-guest hydrogel (low strain=1% strain; high strain=300% strain). **(Bi)** Comparison of colourant diffusion efficiency in different hydrogels. **(Bii)** Microscopy images of hydrogel healing sections. **I** The macro perspective for host-guest hydrogel self-healing.

The modulus changes during the degradation of the host, guest, and host-guest

hydrogels were also evaluated in **Figure 4.9**. Initially, the swelling ratio of the hydrogels increased significantly on the first day and remained stable for the remaining 6 days in the culture medium (**Figure 4.9A**). The host hydrogel exhibited the highest swelling ratio (20%) due to its high-water absorption capacity attributed to hyaluronic acid, followed by the host-guest hydrogel (18%) and the guest hydrogel (10%). Similarly, all hydrogels demonstrated a decrease in modulus on the first day due to hydrogel swelling, followed by a stable modulus over the subsequent 6 days in the culture medium. The modulus remained at around 3 kPa, which aligns with the requirements for establishing a natural neural microenvironment suitable for neuronal differentiation (**Figure 4.9B**). During collagenase degradation shown in **Figure 4.9C-D**, the modulus of the host hydrogels remained stable for 2 days due to the limited degradation of hyaluronic acid by collagenase [269]. In contrast, the compression modulus of the guest hydrogels experienced a reduction from 3 kPa to 1 kPa within 2 days. As for the host-guest hydrogels, the compression modulus was intermediate between that of the host hydrogels and the guest hydrogels, decreased from approximately 3.5 kPa to about 2 kPa [270].

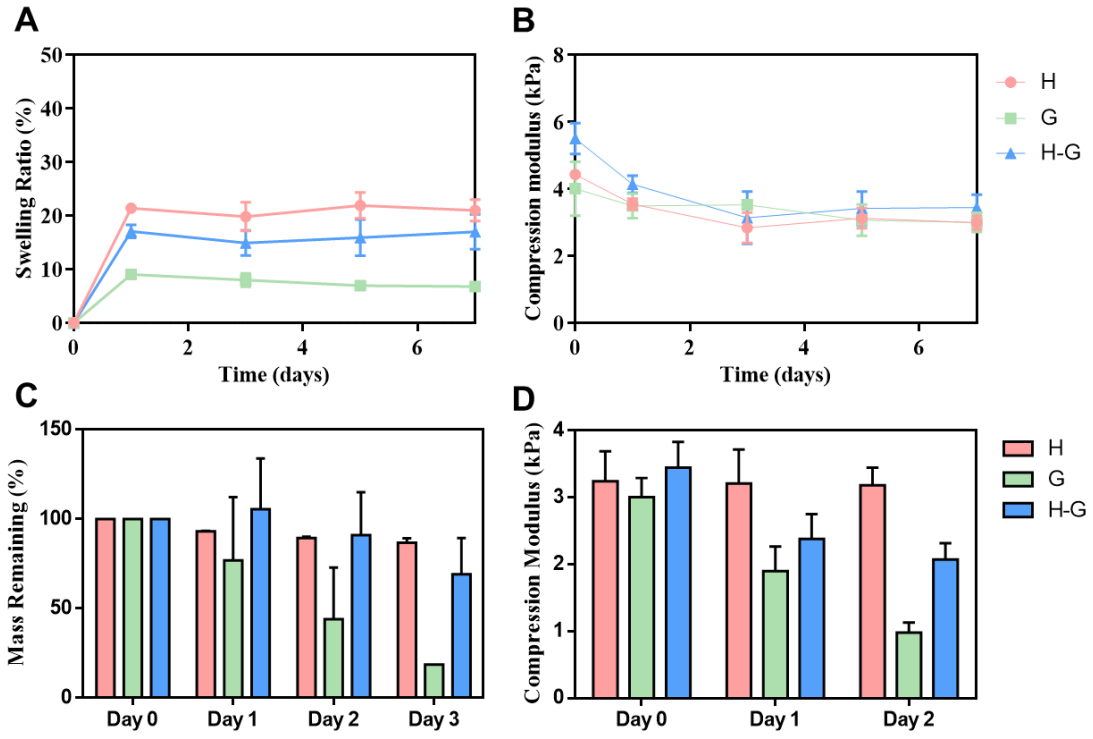

Figure 4.9 (A) Swelling properties of the host, guest, and host-guest hydrogels in RPMI culture medium. **(B)** Compression modulus of the host, guest, and host-guest hydrogels incubated in RPMI solution within 7 days. **(C)** Degradation properties of the host, guest, and host-guest hydrogels in 0.2 U/mL collagenase type II. **(D)** Compression modulus of the host, guest, and host-guest hydrogels incubated in collagenase solution in 2 days.

4.3.3 Rheological and physicochemical properties of host-guest hydrogels

The crosslinking density and structure of the hydrogel are sensitive to the concentrations of the individual macromers and the guest-to-host components, including the weak physical interactions between host and guest complexes and the

multi-fold junctions of polymer chains. To optimise the properties of host-guest hydrogels, the relationship between crosslinking density, junction point architecture, and hydrogels from different concentrations was investigated, with compositions listed in **Table 4.3**.

Table 4.3 The composition of three different host–guest hydrogels for rheological and physicochemical characterization

Sample	Host	Guest
Low	1 wt% CDMeHA	2.5 wt % Ad-GelMA
Med	2 wt% CDMeHA	5 wt% Ad-GelMA
High	4 wt% CDMeHA	10 wt% Ad-GelMA

4.3.3.1 Rheological characterisation of host-guest hydrogels

Rheological properties are crucial for the injectability and printability of host-guest hydrogels. When host-guest hydrogels are extruded from a standard syringe, they undergo shear-thinning (deformation) and fast self-healing (recovery deformation). **Figure 4.9A** shows representative oscillatory frequency sweeps of hydrogels. The modulus of the hydrogels increased with increasing frequency. At low frequencies, the hydrogel exhibited liquid-like properties with a G″ higher than G′. With the frequency increasing to 30 Hz, the storage modulus became closer to the loss modulus, and the hydrogel assumed a gel state. Meanwhile, a rise in concentration resulted in a rise in moduli, as expected. For example, the moduli of the Low, Med, and High concentration

hydrogels at 10 Hz were about 10Pa, 30Pa, and 200Pa, respectively.

4.3.3.2 Viscosity and resultant shear stress

The host-guest interaction was attributed to reversible dynamic bonds, so the formed hydrogels possessed shear-thinning properties. In order to elucidate the intended shear-thinning characteristic of the hydrogels, shear and viscosity tests were conducted, where the shear rate was linearly increased from 0 to 10 S^{-1}. **Figures 4.10B-C** show viscosity variations and shear force under defined simulation conditions. As shown, the host-guest hydrogels had the desired shear-thinning property such that the viscosity exhibited an inverse tendency with the shear rate. Similarly, the shear stress and terminal viscosity also increased with increasing host-guest concentration. This shear-thinning property may have many advantages for biomedical applications because it increases the flowability and reduces the necessary shear force upon injection.

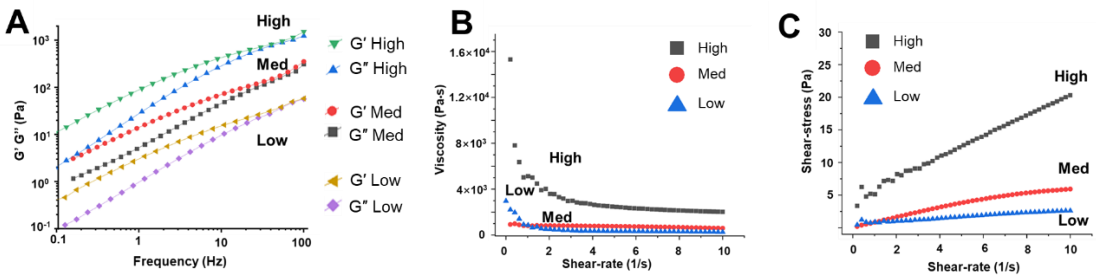

Figure 4.10 (A) Frequency dependence curves of three different host-guest hydrogels (G′=storage modulus; G″=loss modulus). **(B-C)** Shear stress and viscosity curves of three different host-guest hydrogels.

4.3.3.3 SEM and swelling

The crosslinking structure of the hydrogel was characterised by microporous density and size, as shown in **Figure 4.11A**. As expected, the pore size decreased from about 40μm to 10μm with the increase of hydrogel concentration from Low to High. These results confirmed that the crosslinking ability was sensitive to the hydrogel content. The swelling ratio results are shown in **Figure 4.11B**, which also reflects the crosslinking density of the hydrogel. As the hydrogel concentration increased, the swelling ratio decreased from 250% to 60%, indicating an increased crosslinking density.

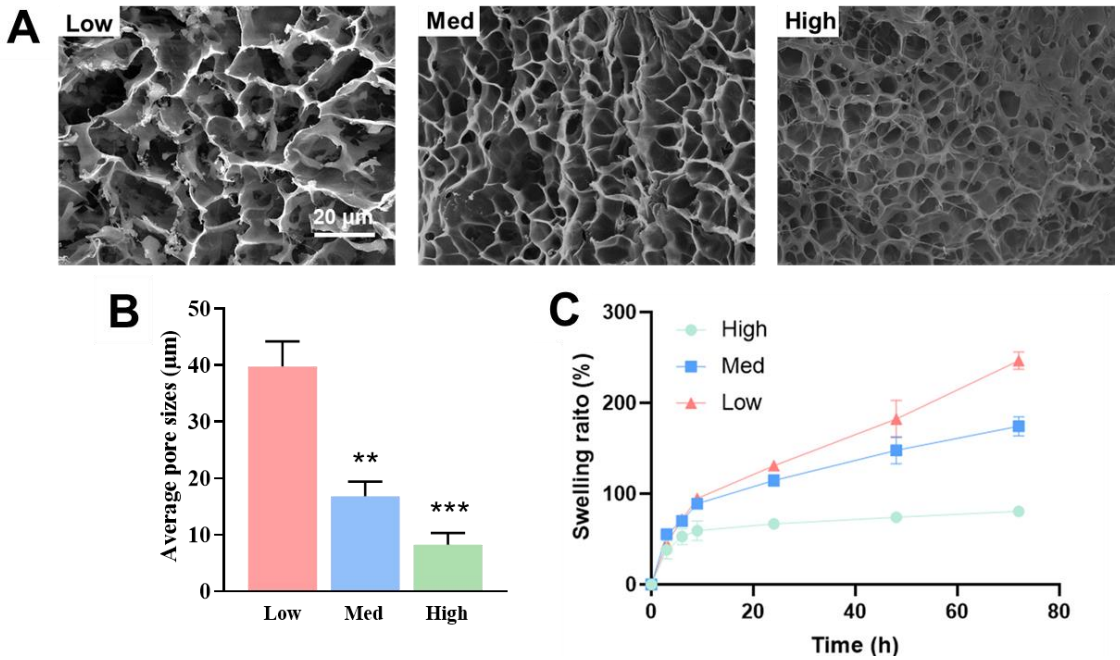

Figure 4.11 SEM images **(A)** average pore size **(B)** and swelling ratios **(C)** of various concentrations of host-guest hydrogels after crosslinking.

4.3.4 Cell encapsulation in host-guest hydrogels

To determine the optimal concentration for cell encapsulation, we encapsulated 3T3 cells in three different hydrogel concentrations (**Table 4.4**). First, from the live/dead

results on the first day, most of the cells (over 96%) were alive, which confirmed that the host-guest hydrogel had excellent cytocompatibility. From the F-actin staining on day 5, although the cells were in good condition, they were in 2D instead of 3D (**Figure 4.12B**). This was because at low hydrogel concentration (I), the host-guest force was too weak to maintain the 3D network structure for a long time [270]. On the contrary, a high concentration of hydrogel (III) limited cell growth, migration, and proliferation in 3D networks because of the high modulus and denser crosslinked network (**Figure 4.12B**). As the middle ground (II), the sample group exhibited a moderate modulus and density, and the cells formed a good 3D network structure in the hydrogel (**Figure 4.12D**). Compared with other hydrogels, such as GelMA, the host-guest hydrogel (II) had a deeper 3D network because the host-guest dynamic force facilitated a better 3D distribution of cells. Therefore, we chose the II concentration for subsequent experiments.

Table 4.4 The composition of host–guest hydrogels for cell encapsulation

Sample	Host	Guest
I	0.5 wt% CDMeHA	1.25 wt% Ad-GelMA
II	1 wt% CDMeHA	2.5 wt% Ad-GelMA
III	2 wt% CDMeHA	5 wt% Ad-GelMA

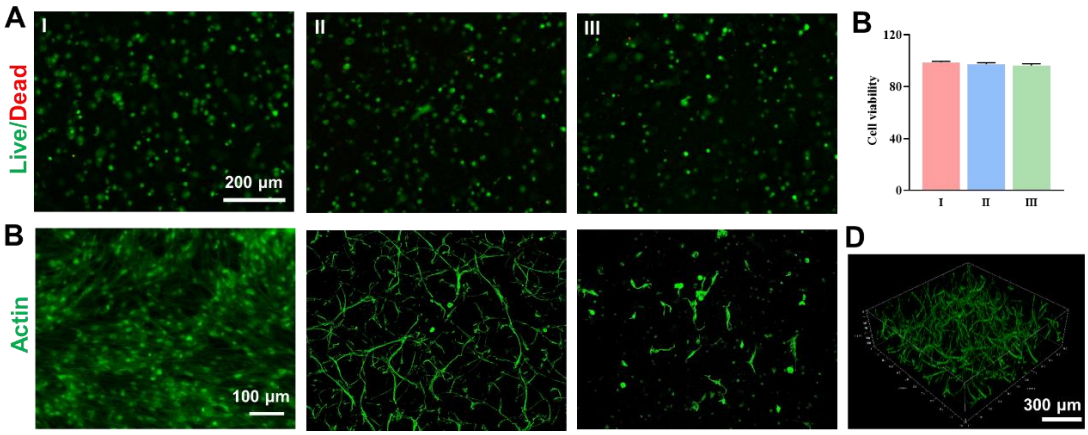

Figure 4.12 Encapsulation of cells in 3D with different concentrations of hydrogels. **(A)** Live/dead staining on day 1. **(B)** Quantitative cell viability on day 1 **(C)** Cell morphology on day 5. **(D)** 3D cell network in host-guest hydrogel (II). I represent 0.5 wt% CDMeHA +1.25 wt% Ad-GelMA; II represents 1 wt% CDMeHA +2.5 wt% Ad-GelMA; III represents 2 wt% CDMeHA +5wt% Ad-GelMA

4.3.5 PC12 cells behaviour and function in different hydrogels

We next investigated the behaviors of PC12 cells encapsulated in different hydrogels. We would like to explore whether the host-guest interaction would interfere or enhance neuronal spreading, migration, and function in the 3D matrix. To evaluate neuronal cell migration and neural tissue regeneration *in vitro*, a simple model, shown in **Figure 4.1,** was constructed for validation. Four different hydrogels (GelMA, host hydrogel, guest hydrogel, and host-guest hydrogel) were selected for migration testing. To control the single variable, hydrogels were prepared with a similar modulus (~1.66 kPa). The corresponding compression moduli of the different hydrogels are shown in **Figure 4.13**.

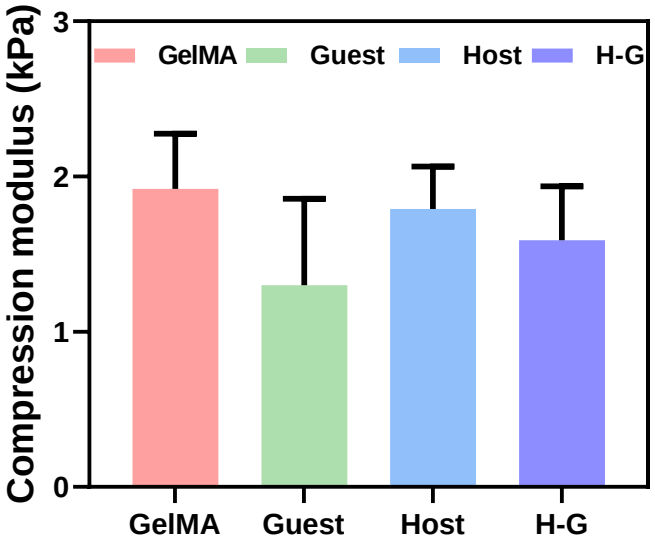

Figure 4.13 The compression moduli of four different hydrogels.

Neuronal extension, morphology, and distribution in the different hydrogels were assessed using BF imaging, confocal imaging, and RT-qPCR. As shown in **Figures 4.14A-B**, clear boundaries between the cell-loaded and cell-free hydrogels were observed, and the PC12 cells maintained high viability in all hydrogels. No neuronal migration was observed in any of the hydrogels on day 1. After 7 days of cultivation, cell migration in different hydrogels was further observed using BF and confocal imaging. As shown in **Figures 4.14C-D**, no significant cell migration or extension was observed in the GelMA and guest (Ad-GelMA) groups. However, the axons of neurons encapsulated in the host (CDMeHA) hydrogel penetrated the cell-free host hydrogels, and more cell migration was observed in the host-guest hydrogel. The cell morphology among different hydrogels was also different. Dynamic host–guest networks had a faster spreading rate than static networks. Unlike the round and non-spreading cells in the static hydrogel, PC12 cells in the host-guest hydrogel started spreading radially on

day 1 (**Figure 4.15A**). Similarly, substantial cell spreading and cytoskeletal proteins were observed in host-guest hydrogels compared with those in static hydrogels on day 7 (**Figure 4.15B**). Ultra-rapid radial cell spreading in the host-guest hydrogel is highly dynamic, permitting cells to pass through and facilitate axon extension [239]. In addition, compared with the GelMA-based (guest) hydrogel, the HA-based (host) hydrogel showed better cell spreading ability individually because HA can also regulate cell migration by organising the ECM into a hydrated open lattice for axonal migration [249, 250]. Relative gene expression was further used to evaluate cell migration in different hydrogels, and five key genes (F-actin, Myosin, FAK, Vinculin, Integrin) were related to cell-ECM interactions and cell migration. As shown in **Figure 4.15C**, the gene expressions of F-actin and FAK in the host-guest hydrogel were almost 2 times higher than those in the static hydrogel. Together, these findings suggested that host-guest interactions mimic the dynamic ECM environment to regulate neuronal cell morphology, spreading, and migration, forming a united neural network. Numerous studies have shown that the migration of nerve cells is an important factor in nerve regeneration, and the migration of cells in host-guest hydrogels provides a good basis for future nerve regeneration *in vivo* [271, 272].

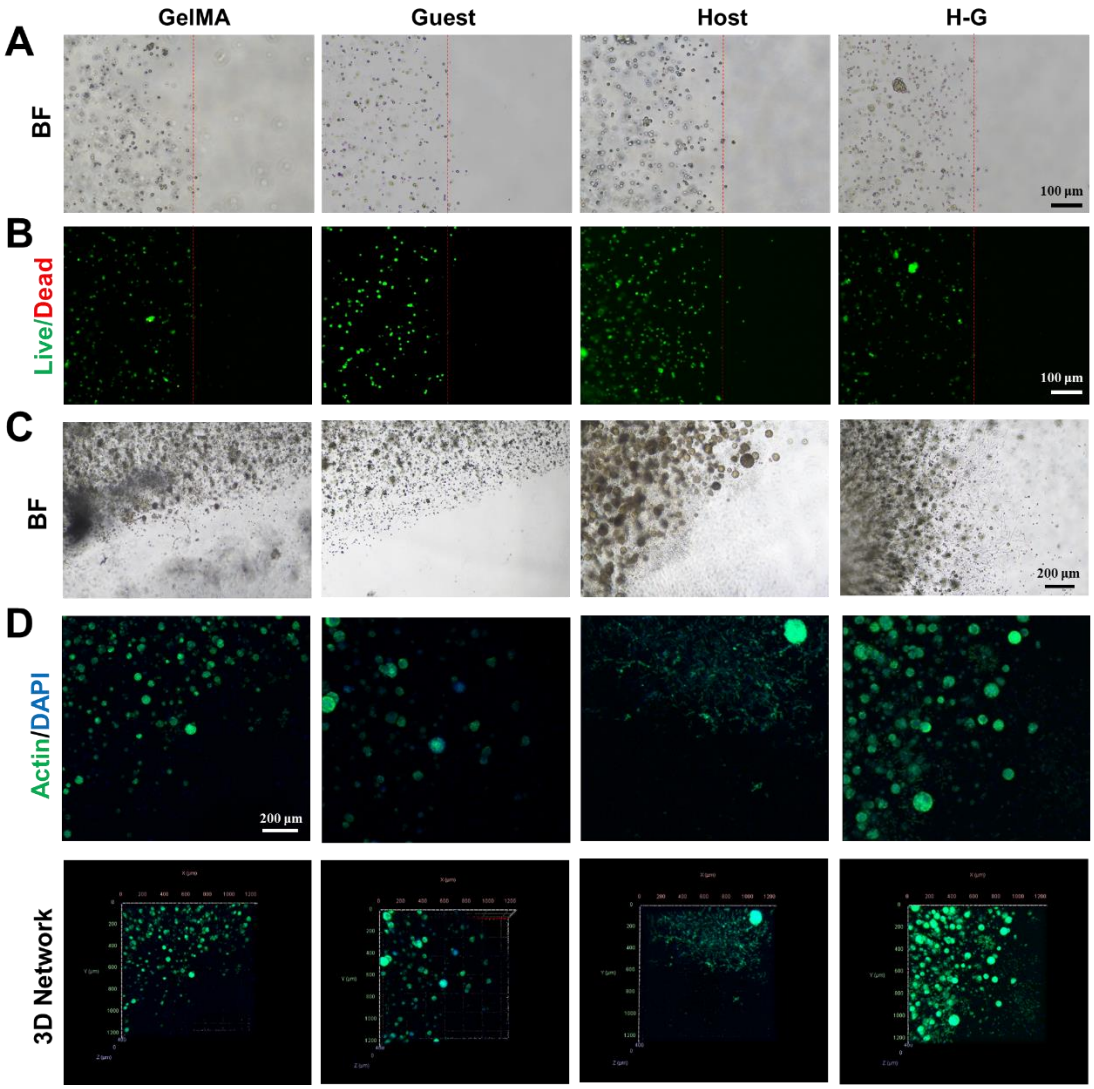

Figure 4.14 Cell migration morphology in different hydrogels on day 7. **(A)** BF images of cells encapsulated in different hydrogels on day 1. **(B)** Live/Dead staining of cells encapsulated in different hydrogels on day 1. **(C)** Cell migration observation through BF images. **(D)** Cell migration and 3D network in different hydrogels through phalloidin/DAPI staining (Z stacks = 400 μm).

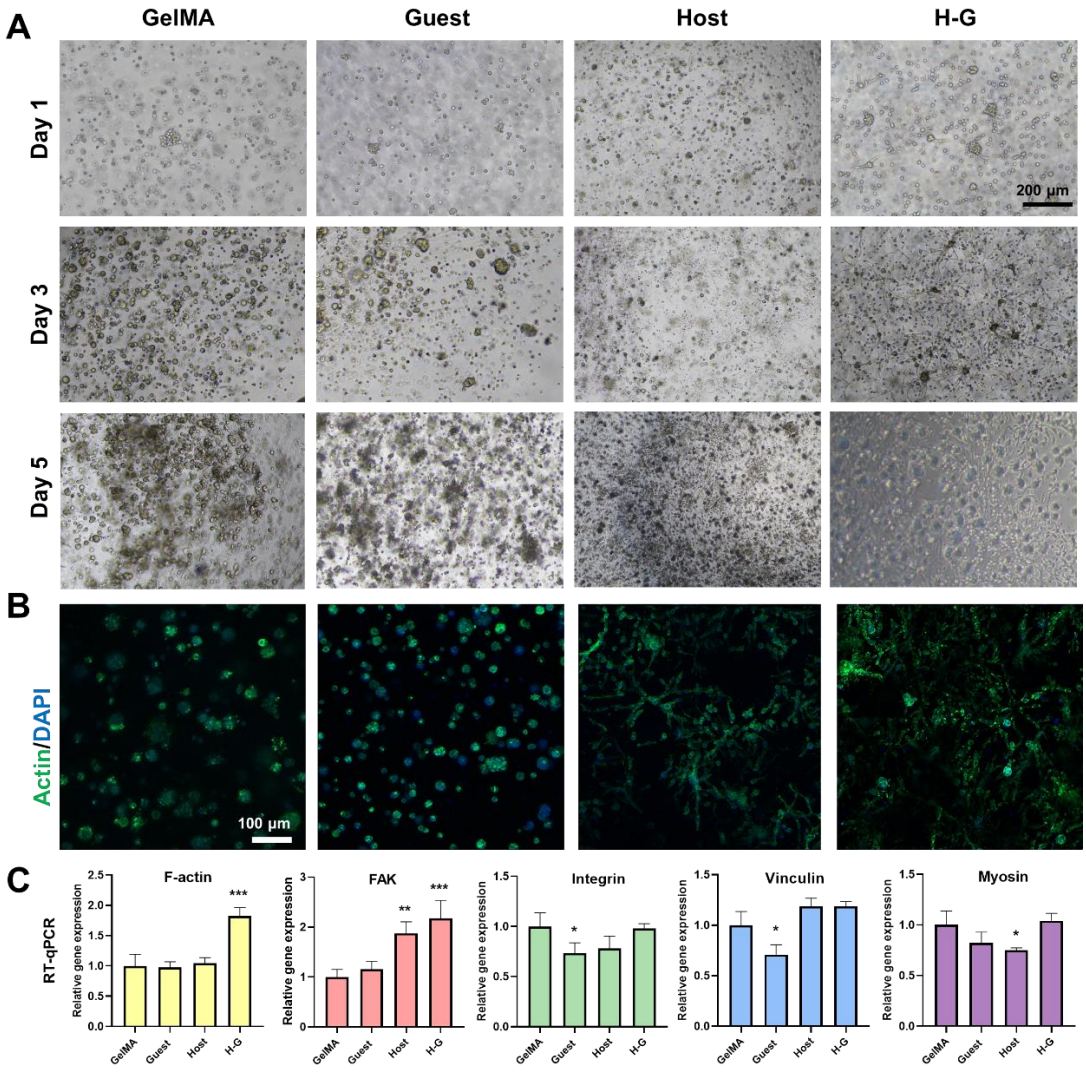

Figure 4.15 Cell morphology in different hydrogels. **(A)** BF observation of cell morphology at different time points. **(B)** Phalloidin/DAPI staining in different hydrogels (Z stacks = 200 μm) on day 7. **(C)** The quantitative RT-qPCR evaluation of cell migration-related gene expressions (F-actin, Myosin, FAK, Vinculin, Integrin) in different hydrogels on day 7.

Important cellular activities in all neuron types are regulated by intracellular calcium signalling. To evaluate the functionality of 3D hydrogels, calcium imaging using Fluo-4 was employed to detect the electrophysiological activity of encapsulated neurons. A

microscope was used for visual inspection and fluorescent imaging (488-nm excitation wavelength), shown in **Figure 4.16A**. The Pseudo-colour of spontaneous electrophysiological activity was analysed using Fiji software, shown in **Figure 4.16B** (The level of intracellular Ca^{2+} concentration correlates with the warmth of the hues.). For quantitative assessment, six representative active neurons in each hydrogel were selected, and the fluorescent signal was plotted over time in **Figure 4.16C**.

As can be seen in **Figure 4.16**, few PC12 cells were detected to have spontaneous electrophysiological activity in GelMA and guest hydrogel groups. However, more PC12 cells and high spontaneous electrical activity ($dF/F>0.5$) were observed in host and host-guest hydrogels. Meanwhile, calcium transients between adjacent cells showed the spontaneous electrophysiological activity of the whole networks in host and host-guest hydrogel. We supposed the increased electrophysiological activity was attributed to the interconnected 3D neural networks, which allowed neural communication and signal transformation (consistent with the results of **Figure 4.15**).

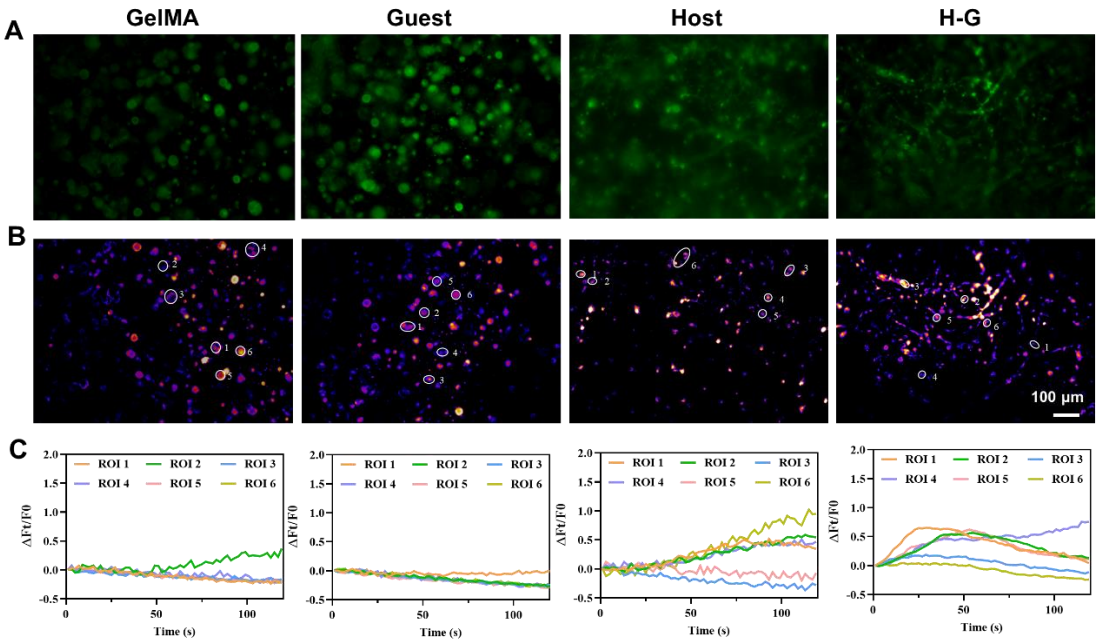

Figure 4.16 Functional assessment of neuronal activity in 3D hydrogels. **(A)** Spontaneous electrophysiological activity in 3D hydrogels via calcium imaging. **(B)** Pseudo-colour of spontaneous electrophysiological activity. **(C)** Representative fluorescent signals change over time.

4.3.6 Injectability and printability

The foundation of 3D printing is the production and management of gel filaments. The extrusion behaviour of different hydrogel bio-inks was evaluated by extension of the filament through a 25-G needle. Rheological characterisation showed that materials with low-viscosity formulations, such as host or guest hydrogel alone, came out of the needle one drop at a time **(Figures 4.17A-B)**. When the host and guest hydrogels were combined, a gel filament that could be used to hang from the end of the needle was formed (**Figure 4.17C**). This was because hydrogels have excellent printing

capabilities owing to their shear-thinning and self-healing properties, as described by Ouyang *et al* [273].

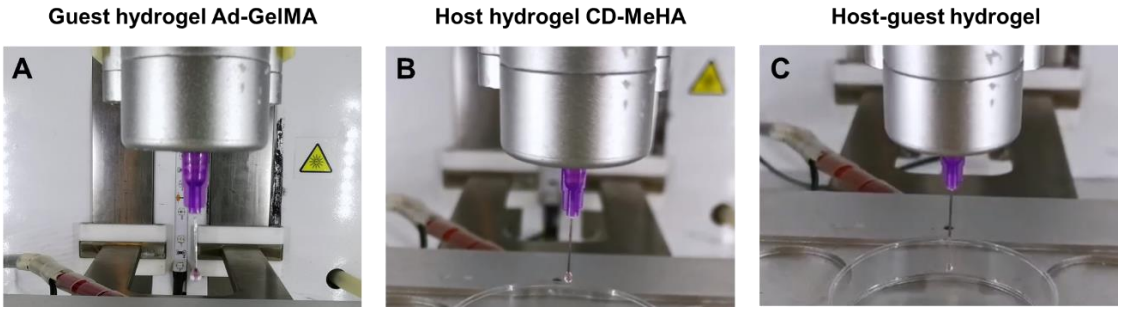

Figure 4.17 Extrusion status of a guest hydrogel **(A)**, host hydrogel **(B),** and host-guest hydrogel **(C)** using a 25-G needle.

Multifarious shapes could be easily achieved by the injectability of the host-guest hydrogel, which was beneficial for matching the tissue environment and minimising mechanical stimulation from the surrounding tissues. As can be seen in **Figure 4.18**, the host-guest hydrogel could be easily extruded from syringes through needles into the PolyU mould owing to the shear-thinning property. After UV crosslinking, a PolyU-shaped hydrogel was obtained.

Figure 4.18 The injectability of host-guest hydrogel.

The dynamic crosslinking in the host-guest hydrogel also improved bioprinting ability.

On the one hand, the hydrogel could be easily extruded from a bioprinting needle with relatively low force owing to the shear-thinning property, which protected the cells in the hydrogel from shear forces to a large extent. On the other hand, the fast self-healing ability of the hydrogel after injection could help maintain the formation of printed filamentous structures. **Figure 4.19** shows the bioprinting process and the 3D-printed structures. After UV crosslinking, the bioprinted structures were stable, with no significant changes in gross appearance. The combination of a double network (host-guest interaction plus covalent cross-linking) played an important role in designing 3D, layer-by-layer printed NTMs.

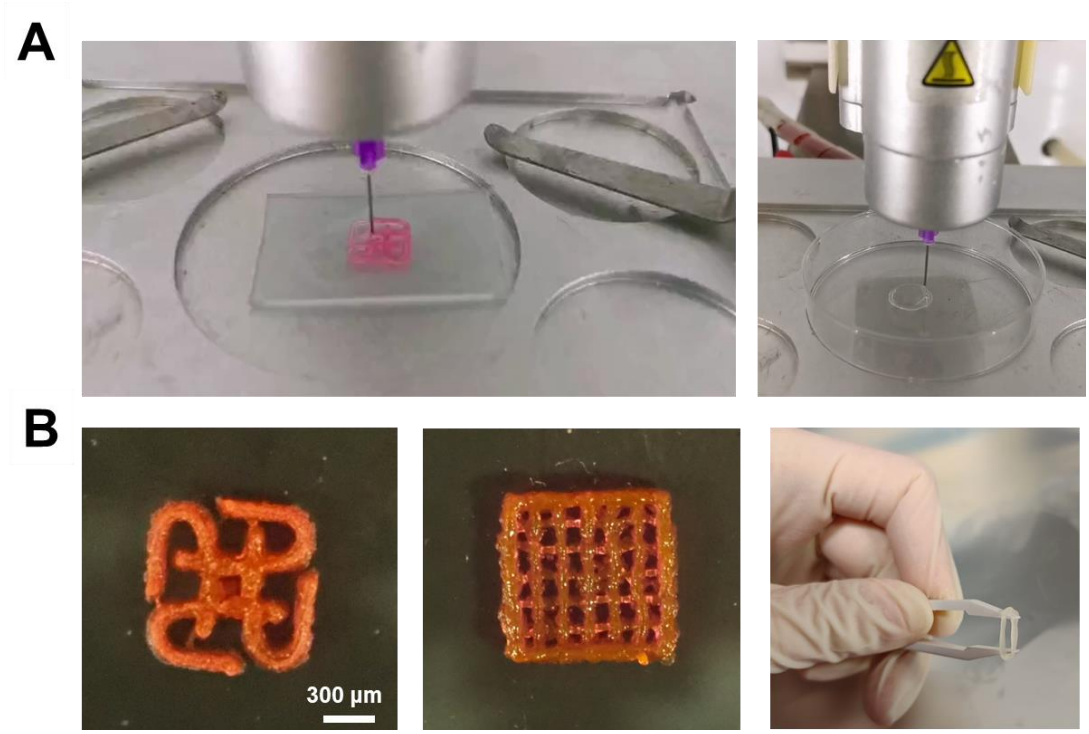

Figure 4.19 The printability of host-guest hydrogel. **(A)** Bioprinting process. **(B)** 3D-printed structure.

4.3.7 Cell viability and differentiation in 3D bioprinted host-guest hydrogels

Neuronal cells are highly sensitive to printing procedures. To assess the cytocompatibility of the bioprinting process, PC12 cells were encapsulated in a host-guest hydrogel for bioprinting. Cell viability and proliferation after printing was characterised by live/dead staining and CCK-8 (**Figures 4.20A-B)**. PC12 cells showed high viability, with over 90% remaining viable after printing (**Figure 4.20Bi**) and printed cells also had significant proliferation (**Figure 4.20Bii**). Meanwhile, the 3D-printed scaffolds supported cell adhesion, growth, and spread in filaments after cultivation (**Figure 4.20C-D**). We supposed that the high cell viability was attributed to the low viscosity and shear-thinning property of the host-guest interaction, which protected the cells from high shear stress during extrusion.

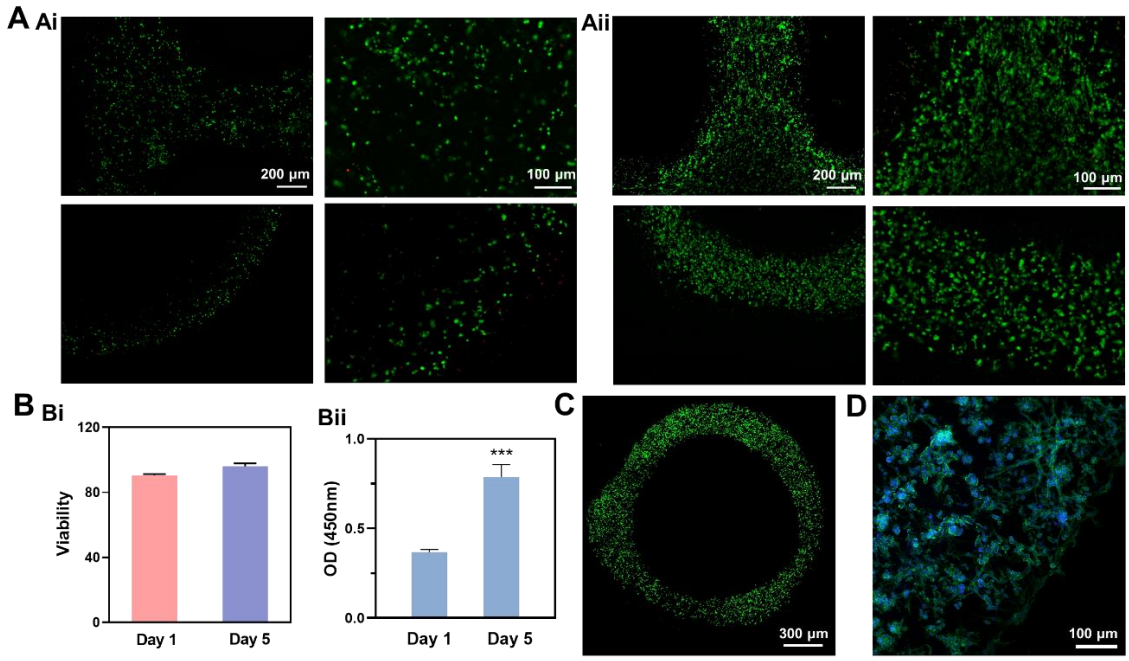

Figure 4.20 Cell viability and proliferation after printing. **(Ai-ii)** Live/dead staining of

printed PC12 cells on days 1 and 5. **(Bi-ii)** Cell viability and proliferation at different times. **(C)** Large image of printed 3D neural ring mimics (stained by live/dead kit 3 days after printing). **(D)** Cell morphology in 3D bioprinted neural ring mimics through phalloidin/DAPI staining (day 5).

4.3.8 Evaluation of electrophysiology in 3D-printed NTMs

To test whether the 3D-printed neurons functioned inside the host-guest hydrogel, we used Fluo-4 AM, a calcium-sensitive fluorescent dye. High-speed imaging then tracked the calcium influxes in the cells over time.

The spontaneous electrophysiological activity was first studied to investigate the neuronal activity of single neurons and the entire network. Confocal microscopy of 3D bioprinted neural rings showed that multiple neurons measured at baseline levels spontaneously increased in fluorescence intensity, marking intracellular calcium influxes (**Figure 4.21**). Six representatives active PC12 cells were selected, and the fluorescent signal was plotted over time for quantitative assessment (**Figures 4.21A-B**). From the representative image sequence (**Figure 4.21C**), calcium transients were also observed between adjacent PC12 cells at different time points, indicating the spontaneous electrophysiological activity of the whole network.

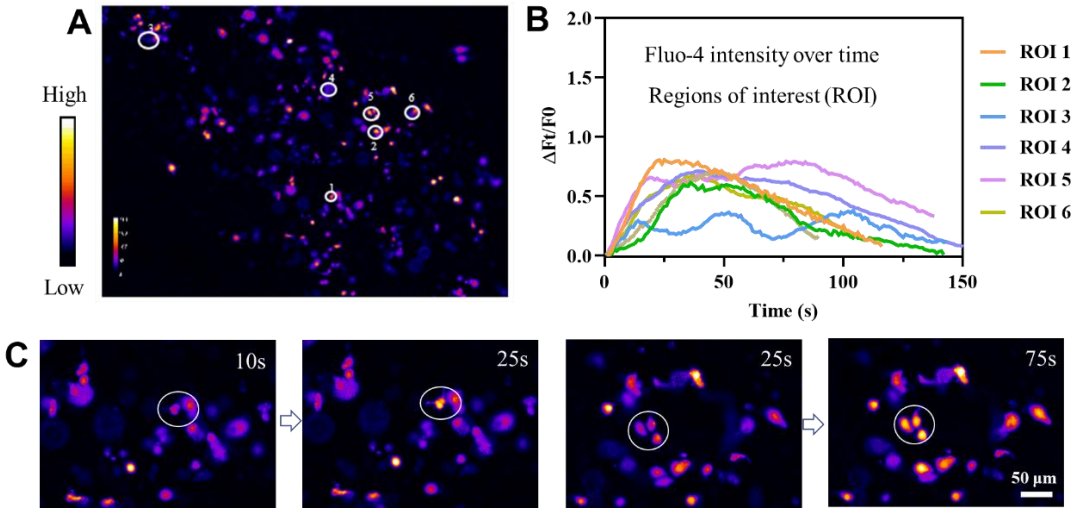

Figure 4.21 Electrophysiological activity of 3D bioprinted neural ring mimics. **(A)** Spontaneous electrophysiological activity of 3D bioprinted neural ring mimics via calcium imaging. **(B)** Representative fluorescent signal changes over time. **(C)** The representative image sequence shows adjacent cells with calcium transients.

KCl, a signalling chemical, was used to further define the enhanced electrophysiological activity of the printed PC12 cells. Increased intracellular calcium ions are caused by the high extracellular potassium chloride concentration, which raises the membrane potential of the cell and opens the voltage-dependent calcium ion channel. Adding KCl resulted in a significant increase in fluorescence intensity, as illustrated in **Figure 4.22**. Typical cells were measured throughout the experiment, and all responded to high potassium levels by increasing their fluorescence intensity by a factor of two. There was conclusive evidence of the 3D-printed neural circle owing to the presence of electrically activated neurons.

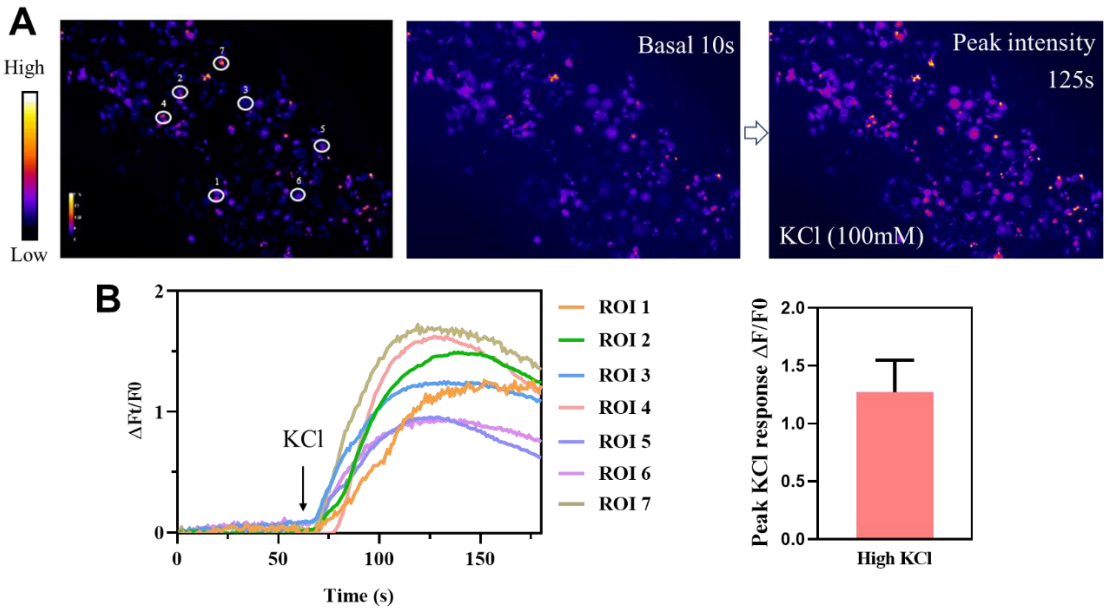

Figure 4.22 Stimulated electrophysiological activity of 3D bioprinted neural ring mimics. **(A)** Potassium chloride (KCl) stimulated the electrophysiological activity of 3D bioprinted neural rings. **(B)** Representative fluorescent signal changes over time.

4.4 Summary

In conclusion, host-guest hydrogels with notable shear-thinning and rapid self-healing properties were successfully fabricated. The rheological properties indicated that the host-guest hydrogel had excellent injectability for the printing process and outstanding self-healing ability for repeated damage due to host-guest interactions. The host-guest hydrogel could be printed and maintained in various shapes, with excellent biocompatibility to support cell growth and proliferation in 3D structures.

Typically, neural cells are highly sensitive to the printing procedure and have low viability after printing. However, neural cells (PC12) exhibited high viability during printing because host-guest interactions protected cells from high shear stress. After 7 days of cultivation, the PC12 cells proliferated well and maintained a printed structure.

Calcium imaging showed that the printed neuronal mimics displayed high levels of electrical activity, as indicated by a spontaneous increase in fluorescence intensity. Meanwhile, the host-guest interaction promoted cell migration and spreading to form interconnected 3D networks. Based on these findings, bioprinted neural mimics appeared to be promising drug-testing models that could advance methods for assessing neural functionality *in vitro* and support the development of better models for disease studies in the neuroscience research community and the pharmaceutical industry.

Chapter 5 Conclusions and recommendations for future work

5.1 Major findings and conclusion

Researchers have investigated *in vitro* modelling of NTMs, but these studies have focused mostly on 2D substrates and did not simulate the 3D microstructure of neural tissues. Numerous species-specific characteristics of the nervous system cannot be investigated using animal models, even though they provide a powerful option for studying neural development, neurological disease, and regeneration processes. In addition, understanding how neural circuits arise and develop is essential to understanding how the brain works. Therefore, it is necessary to construct 3D neural mimics. In this study, a variety of biomimetic and functional hydrogels were created to investigate neural development, neurogenesis, and electrophysiology in a 3D environment.

Chapter 2 describes the production of soft and flexible GelMA-PEGDA hydrogels with a favourable microenvironment for neuronal cell development. By adding PEGDA and adjusting its concentration to GelMA, the matrix stiffness of the hydrogels was altered, and their overall tensile properties were enhanced. GelMA-PEGDA had excellent biocompatibility for 3D neural cell growth, although the inclusion of PEGDA had little effect on cell survival and proliferation, owing to the absence of the RGD group. Stem cells were more conducive to glial cell differentiation in GelMA hydrogel with high

GFAP protein expression and neuronal cell development in GelMA-PEGDA hydrogel with high Tuj-1 protein expression. Matrix stiffness was the primary factor influencing neuronal cell differentiation and development. Mechanical stretching may further improve 3D neuronal differentiation in axon elongation and neurite orientation.

Furthermore, conductive hydrogels were developed following the preceding chapter, and the electrical conductivity and mechanical properties were examined in Chapter 3. Compared with conventional hydrogels, the conductive hydrogel alone could promote the differentiation of NSC. The conductive hydrogel combined with ES may further drive neuronal differentiation. Simultaneously, the influence of various electric field intensities on neuronal differentiation was studied to maximise the effects of ES. Stretching and electrical co-stimulation were explored further. Consistent with prior studies, stretching was shown to trigger neuronal differentiation and promote neurite outgrowth and the directional alignment of nerve extensions. Stretching and electrical co-stimulation affected neurite outgrowth, neurite branching, and filopodia density. In addition to changes in cell morphology, simultaneous co-stimulation may affect neural gene expression. Co-stimulation boosted the expression of neuron-specific markers (MAP2, Tuj-1, and GFAP), which play crucial roles in neuronal development and function, as shown by RT-qPCR.

Finally, host-guest hydrogels with excellent shear strength and rapid self-healing properties are described in Chapter 4. The rheological features of the host-guest

hydrogel showed great injectability for the printing process and remarkable self-healing capabilities for recurrent injury. Host-guest hydrogels could be produced and stored in a variety of forms. Moreover, the host-guest hydrogel had outstanding biocompatibility for promoting cell growth, proliferation, and migration, forming a 3D interconnected network. Although neuronal cells are highly susceptible to the printing method, resulting in reduced cell viability, PC12 cells displayed high viability when printed because the host-guest interaction shielded them from excessive shear stress. Calcium imaging also revealed that the printed neuronal mimics exhibited significant levels of spontaneous electrical activity, as indicated by an increased fluorescence intensity.

Overall, a range of biomimetic and functional hydrogels have been produced for neural development, neurogenesis, and electrophysiology in 3D environments. Results demonstrated that GelMA-PEGDA hydrogel encapsulation and stretching are potential strategies for improving the efficacy and viability of NSC therapies for neural regeneration. Meanwhile, the co-stimulation of stretching and ES exhibited synergetic effects on neuronal development and neurogenesis. These studies not only enrich the research on the directed differentiation of NSC in a 3D microenvironment induced by physical stimuli but also offer a foundation for the efficacy and practicability of NSC treatment. In addition, 3D bioprinted neural mimics with good viability and electroactivity appear to be promising advance models for assessing neural functionality *in vitro* and support the development of better NTMs for disease studies in both the neuroscience research community and the pharmaceutical industry.

5.2 Recommendations for future work

In this thesis, functional and biomimetic hydrogels were developed for 3D neural investigation, and cell behaviour and development within 3D hydrogels were studied by microenvironment effects (stiffness, mechanical stretching, ES, and host-guest interaction). While significant progress has been made in understanding these effects, there remain several avenues for future research and exploration in this topic.

5.2.1 Effect of stretching strategies on neuronal differentiation

Stretching has a positive effect on promoting neural cell differentiation and axonal growth. In our previous experiments on stretching, we discovered that neural cells grow along the direction of stretching when subjected to static unidirectional stretching using hydrogels. In addition to static unidirectional stretching, there are various other stretching methods such as dynamic stretching, compression stretching, bidirectional stretching, and cyclic stretching. These different stretching methods have varying effects on promoting neural cell differentiation and axonal growth. However, the specific outcomes may depend on the stretching parameters, such as strain amplitude, frequency, and duration, as well as cell types and experimental conditions. Therefore, in our future work, we aim to investigate the effects and underlying mechanisms of different stretching methods on neural differentiation and optimize the stretching protocols to achieve desired neural differentiation outcomes.

5.2.2 Effect of electrical stimulation strategies on neuronal differentiation

In previous studies, we have explored the effects of different electrical stimulation intensities on neural differentiation. We found that an excessively high electric field, such as 1V/mm, can be detrimental to the cells. Moderate electric field strengths, such as 100mV/mm, were found to be more favourable for neural differentiation. In addition to electric field strength, the mode of electrical stimulation, including direct current (DC) and alternating current (AC), as well as continuous and intermittent stimulation, can influence neural differentiation by altering ion migration, charge accumulation, signal transduction, and ion channel activity. Previous research conducted on 2D substrates has demonstrated the positive effects of both AC and DC stimulation on neural differentiation, promoting the expression of neural markers, neurite outgrowth, and functional maturation [70]. However, they differ in their mechanisms of action, spatial and temporal effects, current direction, and cellular responses. Several studies have also suggested that intermittent stimulation may be more effective than continuous stimulation in promoting the differentiation of NSCs into neurons. Conversely, continuous stimulation may be more effective in promoting the differentiation of NSCs into glial cells. Therefore, future research investigating the effects of different stimulation modalities on 3D neural differentiation is crucial. In our future plans, we would like to explore different stimulation strategies and evaluate their impact on NSC differentiation. By investigating various parameters and protocols, we hope to gain a deeper understanding of the underlying mechanisms and optimize the stimulation

approach to achieve desired outcomes in neural differentiation.

5.2.3 Mechanism of neuronal differentiation induced by different stimuli

To gain a comprehensive understanding of the mechanisms underlying neuronal differentiation induced by different stimuli, it is crucial to conduct further molecular research. This deeper understanding holds significant importance in elucidating the intricate processes involved in neuronal development and can have implications for various applications in neuroscience and regenerative medicine.

Despite previous studies utilizing RT-qPCR to investigate changes in gene expression, further molecular research is necessary to uncover the precise mechanisms governing neuronal differentiation. Specifically, advanced techniques such as Western blotting (WB) and gene sequencing, such as RNA sequencing (RNA-seq), can provide valuable insights into the molecular dynamics of this process.

WB is a widely employed technique in molecular biology that enables the detection and analysis of specific proteins. By utilizing WB, researchers can examine the levels and expression patterns of proteins during neuronal differentiation, allowing for a more detailed understanding of the protein-level changes that occur. Meanwhile Gene sequencing, particularly RNA-seq, offers a comprehensive overview of gene expression patterns and facilitates the identification of differentially expressed genes throughout

neuronal differentiation. By comparing gene expression profiles between stimulated and control conditions, researchers can discern the specific genes and pathways that are activated or suppressed by the stimuli, thereby unraveling the underlying molecular mechanisms involved in neuronal differentiation. Furthermore, gene sequencing can be leveraged to identify signaling pathways and determine the upregulation or downregulation of particular genes, enhancing our understanding of the intricate signaling cascades governing this process.

5.2.4 Construction of neural mimics with different types of neuronal cells

Despite significant breakthroughs in neuroscience, our current understanding of brain dysfunction and CNS regeneration remains limited. Constructing functional neural models *in vitro* offers a promising avenue for studying the mechanisms underlying these diseases and developing effective treatments. In previous research, we utilized highly differentiated PC12 cells to construct a neural circuit using 3D printing, resulting in electrical activity. To further enhance the functionality of these neural mimics, our future objective is to incorporate different types of neuronal cells. By introducing a variety of cell types, we can facilitate cell-cell interactions, thereby improving the connectivity of the neural network. This utilization of diverse neuronal cells confers numerous advantages, including functional diversity, circuit complexity, specialization, adaptability, robustness, and the ability to model diseases.

Furthermore, we can also employ cells derived from individuals with specific diseases to construct disease models. For example, using cells from patients with Alzheimer's disease to create an Alzheimer's model is a common approach. This strategy allows us to gain a better understanding of the disease's mechanisms and enables the exploration of potential treatments. By leveraging these disease models, we can uncover crucial insights into the pathology and pathogenesis of various diseases, paving the way for advancements in clinical research and therapeutic interventions.

5.2.5 Application of neuronal mimics in drug screening

Currently , it is difficult to measure pharmacological effects owing to the large number of potential secondary neuronal and non-neuronal targets [132]. Less than 10% of proposed drugs for neurological diseases are clinically approved. Phase II and III medication development for neuropathy is delayed by years owing to high attrition rates in clinical trials. Numerous clinical impairments appear late in clinical trials, demonstrating a disconnect between preclinical findings and hospitalised patient outcomes. The 3D NTMs could also be a more advanced *in vitro* model for drug toxicity. We can test the 3D capacity of NTMs to identify hazards by exposing them to neuroactive chemicals and neurotoxins.

The detailed plans for drug screening using our 3D printed neural tissue are as follows (Alzheimer's disease as an example):

1) Cell culture and model construction:

Select appropriate cell lines or primary cells that exhibit relevant characteristics of Alzheimer's disease, such as Alzheimer’s disease patient-derived hiPSCs generate neurons and astrocytes. Construction of 3D neural mimics as describe in section 5.2.4.

2) Model validation and evaluation:

Perform comprehensive characterization of the constructed model by assessing key features associated with Alzheimer's disease, such as amyloid-beta deposition, tau hyperphosphorylation, synaptic dysfunction, and neuronal cell death. Utilize techniques such as immunocytochemistry, ELISA, Western blotting, and functional assays to quantify and evaluate the presence and severity of these disease-related features. Compare the results obtained from the constructed model with established benchmarks and reference models to assess the similarity and reliability of the *in vitro* model.

3) Drug screening:

Acquire a diverse library of compounds, including known drugs, investigational compounds, and natural products, with potential therapeutic effects on Alzheimer's disease. Establish appropriate screening assays based on the specific aspects of Alzheimer's pathogenesis targeted by the compounds, such as amyloid-beta aggregation, tau phosphorylation, or neuroinflammation. Screen the compounds using the constructed *in vitro* model and evaluate their effects on disease-related features using

relevant readouts and assays. Prioritize compounds showing promising therapeutic potential for further investigation.

4) Data analysis and interpretation:

Analyze the obtained experimental data using appropriate statistical methods and data visualization techniques. Interpret the results to draw conclusions regarding the success of the constructed model, the efficacy of screened compounds, and the role of signaling pathways in Alzheimer's disease pathogenesis. Share the findings through scientific publications, conferences, and collaborations to contribute to the broader scientific community's understanding of Alzheimer's disease and its potential treatments.

Bibliography

1. Spradling A, Drummond-Barbosa D, Kai T. (2001) Stem cells find their niche. Nature. 414 (6859):98-104.

2. Li L, Xie T. (2005) Stem cell niche: structure and function. Annual review of cell and developmental biology. 21 (1):605-631.

3. Huang G, Li F, Zhao X, Ma Y, Li Y, Lin M, Jin G, Lu TJ, Genin GM, Xu F. (2017) Functional and biomimetic materials for engineering of the three-dimensional cell microenvironment. Chemical reviews. 117 (20):12764-12850.

4. Xin T, Greco V, Myung P. (2016) Hardwiring stem cell communication through tissue structure. Cell. 164 (6):1212-1225.

5. Kimble D. The Nervous System And The Brain. Companion Encyclopedia of Psychology: Routledge; 2019. p. 88-108.

6. Wu Y, Kyungsun K. (2022) Automatic generation of traditional patterns and aesthetic quality evaluation technology. Information Technology and Management.1-19.

7. Jessen KR. (2004) Glial cells. The international journal of biochemistry & cell biology. 36 (10):1861-1867.

8. Greenhalgh AD, David S, Bennett FC. (2020) Immune cell regulation of glia during CNS injury and disease. Nature Reviews Neuroscience. 21 (3):139-152.

9. Maldonado-Soto AR, Oakley DH, Wichterle H, Stein J, Doetsch FK, Henderson CE. (2014) Stem cells in the nervous system. American journal of physical medicine & rehabilitation/Association of Academic Physiatrists. 93 (11 0 3):S132.

10. Lim DA, Alvarez-Buylla A. (2016) The adult ventricular–subventricular zone (V-SVZ) and olfactory bulb (OB) neurogenesis. Cold Spring Harbor perspectives in biology. 8 (5):a018820.

11. Kempermann G, Song H, Gage FH. (2015) Neurogenesis in the adult hippocampus. Cold Spring Harbor perspectives in biology. 7 (9):a018812.

12. Bai X. Stem cell-based disease modeling and cell therapy. MDPI; 2020. p. 2193.

13. Rafalski VA, Brunet A. (2011) Energy metabolism in adult neural stem cell fate. Progress in neurobiology. 93 (2):182-203.

14. Reekmans K, Praet J, Daans J, Reumers V, Pauwels P, Van der Linden A, Berneman ZN, Ponsaerts P. (2012) Current challenges for the advancement of neural stem cell biology and transplantation research. Stem cell reviews and reports. 8:262-278.

15. Humpel C. (2015) Organotypic brain slice cultures: A review. Neuroscience. 305:86-98.

16. Simao D, Silva MM, Terrasso AP, Arez F, Sousa MF, Mehrjardi NZ, Šarić T, Gomes-Alves P, Raimundo N, Alves PM. (2018) Recapitulation of human neural microenvironment signatures in iPSC-derived NPC 3D differentiation. Stem Cell Reports. 11 (2):552-564.

17. Smith RA. (2009) Twenty-first century challenges for in vitro neurotoxicity. Alternatives to Laboratory Animals. 37 (4):367-375.

18. Radio NM, Mundy WR. (2008) Developmental neurotoxicity testing in vitro: models for assessing chemical effects on neurite outgrowth. Neurotoxicology. 29 (3):361-376.

19. Namsi A, Nury T, Hamdouni H, Yammine A, Vejux A, Vervandier-Fasseur D, Latruffe N, Masmoudi-Kouki O, Lizard G. (2018) Induction of neuronal differentiation of murine N2a cells by two polyphenols present in the mediterranean diet mimicking neurotrophins activities: resveratrol and apigenin. Diseases. 6 (3):67.

20. Biedler JL, Helson L, Spengler BA. (1973) Morphology and growth, tumorigenicity, and cytogenetics of human neuroblastoma cells in continuous culture. Cancer research. 33 (11):2643-2652.

21. Greene LA, Tischler AS. (1976) Establishment of a noradrenergic clonal line of rat adrenal pheochromocytoma cells which respond to nerve growth factor. Proceedings of the National Academy of Sciences. 73 (7):2424-2428.

22. Sebök Á, Nusser N, Debreceni B, Guo Z, Santos MF, Szeberenyi J, Tigyi G. (1999) Different roles for RhoA during neurite initiation, elongation, and regeneration in PC12 cells. Journal of neurochemistry. 73 (3):949-960.

23. Özbek S, Balasubramanian PG, Chiquet-Ehrismann R, Tucker RP, Adams JC. (2010) The evolution of extracellular matrix. Molecular biology of the cell. 21 (24):4300-4305.

24. Page-McCaw A, Ewald AJ, Werb Z. (2007) Matrix metalloproteinases and the regulation of tissue remodelling. Nature reviews Molecular cell biology. 8 (3):221-233.

25. Yue B. (2014) Biology of the extracellular matrix: an overview. Journal of glaucoma.S20.

26. Frantz C, Stewart KM, Weaver VM. (2010) The extracellular matrix at a glance. Journal of cell science. 123 (24):4195-4200.

27. Ramos-Cejudo J, Wisniewski T, Marmar C, Zetterberg H, Blennow K, de Leon MJ, Fossati S. (2018) Traumatic brain injury and Alzheimer's disease: the cerebrovascular link. EBioMedicine. 28:21-30.

28. Walma DAC, Yamada KM. (2020) The extracellular matrix in development. Development. 147 (10):dev175596.

29. Gilmore JH, Knickmeyer RC, Gao W. (2018) Imaging structural and functional brain development in early childhood. Nature Reviews Neuroscience. 19 (3):123-137.

30. Gattazzo F, Urciuolo A, Bonaldo P. (2014) Extracellular matrix: a dynamic microenvironment for stem cell niche. Biochimica et Biophysica Acta (BBA)-General Subjects. 1840 (8):2506-2519.

31. Sansom SN, Livesey FJ. (2009) Gradients in the brain: the control of the development of form and function in the cerebral cortex. Cold Spring Harbor perspectives in biology. 1 (2):a002519.

32. Yurchenko I, Farwell M, Brady DD, Staii C. (2021) Neuronal growth and formation of neuron networks on directional surfaces. Biomimetics. 6 (2):41.

33. Martino G, Pluchino S, Bonfanti L, Schwartz M. (2011) Brain regeneration in physiology and pathology: the immune signature driving therapeutic plasticity of neural stem cells. Physiological reviews. 91 (4):1281-1304.

34. Lu P, Takai K, Weaver VM, Werb Z. (2011) Extracellular matrix degradation and remodeling in development and disease. Cold Spring Harbor perspectives in biology. 3

(12):a005058.

35. Jain D, Mattiassi S, Goh EL, Yim EK. (2020) Extracellular matrix and biomimetic engineering microenvironment for neuronal differentiation. Neural regeneration research. 15 (4):573.

36. Tyler WJJNRN. (2012) The mechanobiology of brain function. Nature Reviews Neuroscience. 13 (12):867-878.

37. Guimarães CF, Gasperini L, Marques AP, Reis RLJNRM. (2020) The stiffness of living tissues and its implications for tissue engineering. Nature Reviews Materials. 5 (5):351-370.

38. Fan L, Liu C, Chen X, Zou Y, Zhou Z, Lin C, Tan G, Zhou L, Ning C, Wang QJAam, interfaces. (2018) Directing induced pluripotent stem cell derived neural stem cell fate with a three-dimensional biomimetic hydrogel for spinal cord injury repair. ACS Applied Materials & Interfaces. 10 (21):17742-17755.

39. Gholipourmalekabadi M, Zhao S, Harrison BS, Mozafari M, Seifalian AM. (2016) Oxygen-generating biomaterials: a new, viable paradigm for tissue engineering? Trends in biotechnology. 34 (12):1010-1021.

40. Brizzi MF, Tarone G, Defilippi P. (2012) Extracellular matrix, integrins, and growth factors as tailors of the stem cell niche. Current opinion in cell biology. 24 (5):645-651.

41. Altman GH, Horan RL, Martin I, Farhadi J, Stark PR, Volloch V, Richmond JC, Vunjak-Novakovic G, Kaplan DL. (2002) Cell differentiation by mechanical stress. The FASEB Journal. 16 (2):1-13.

42. Hinkle ER, Blue RE, Tsai Y-H, Combs M, Davi J, Coffey AR, Boriek AM, Taylor JM, Parker JS, Giudice J. (2022) Stretching muscle cells induces transcriptional and splicing transitions and changes in SR proteins. Communications biology. 5 (1):987.

43. Yu H-S, Kim J-J, Kim H-W, Lewis MP, Wall I. (2016) Impact of mechanical stretch on the cell behaviors of bone and surrounding tissues. Journal of Tissue Engineering. 7:2041731415618342.

44. Sprague B, Chesler NC, Magness RR. (2010) Shear stress regulation of nitric oxide

production in uterine and placental artery endothelial cells: experimental studies and hemodynamic models of shear stress forces on endothelial cells. The International journal of developmental biology. 54 (2-3):331.

45. Lane Smith R, Trindade M, Ikenoue T, Mohtai M, Das P, Carter D, Goodman S, Schurman D. (2000) Effects of shear stress on articular chondrocyte metabolism. Biorheology. 37 (1-2):95-107.

46. Waller KA, Zhang LX, Elsaid KA, Fleming BC, Warman ML, Jay GD. (2013) Role of lubricin and boundary lubrication in the prevention of chondrocyte apoptosis. Proceedings of the National Academy of Sciences. 110 (15):5852-5857.

47. Shi Y, Inoue H, Wu JC, Yamanaka S. (2017) Induced pluripotent stem cell technology: a decade of progress. Nature reviews Drug discovery. 16 (2):115-130.

48. Dutta D, Heo I, Clevers H. (2017) Disease modeling in stem cell-derived 3D organoid systems. Trends in molecular medicine. 23 (5):393-410.

49. Li R, Li D-h, Zhang H-y, Wang J, Li X-k, Xiao J. (2020) Growth factors-based therapeutic strategies and their underlying signaling mechanisms for peripheral nerve regeneration. Acta Pharmacologica Sinica. 41 (10):1289-1300.

50. George S, Hamblin MR, Abrahamse H. (2018) Current and future trends in adipose stem cell differentiation into neuroglia. Photomedicine and Laser Surgery. 36 (5):230-240.

51. Woodbury D, Schwarz EJ, Prockop DJ, Black IB. (2000) Adult rat and human bone marrow stromal cells differentiate into neurons. Journal of neuroscience research. 61 (4):364-370.

52. Prabhakaran MP, Venugopal JR, Ramakrishna S. (2009) Mesenchymal stem cell differentiation to neuronal cells on electrospun nanofibrous substrates for nerve tissue engineering. Biomaterials. 30 (28):4996-5003.

53. Huang T, He D, Kleiner G, Kuluz JT. (2007) Neuron-like differentiation of adipose-derived stem cells from infant piglets in vitro. The journal of spinal cord medicine. 30 (sup1):S35-S40.

54. Jaswal R, Kaliannagounder VK, Kumar D, Park CH, Kim CS. (2022) Modulated

plasmonic nanofibrous scaffold reinforced breast cancer photo-ablation and breast neurotization with resensation. Composites Part B: Engineering. 243:110129.

55. Baek J, Lopez PA, Lee S, Kim T-S, Kumar S, Schaffer DV. (2021) 3D Microenvironment-Specific Mechanosensing Regulates Neural Stem Cell Lineage Commitment. bioRxiv.

56. Her GJ, Wu H-C, Chen M-H, Chen M-Y, Chang S-C, Wang T-W. (2013) Control of three-dimensional substrate stiffness to manipulate mesenchymal stem cell fate toward neuronal or glial lineages. Acta Biomaterialia. 9 (2):5170-5180.

57. Mammadov B, Sever M, Guler MO, Tekinay AB. (2013) Neural differentiation on synthetic scaffold materials. Biomaterials science. 1 (11):1119-1137.

58. Teixeira AI, Ilkhanizadeh S, Wigenius JA, Duckworth JK, Inganäs O, Hermanson O. (2009) The promotion of neuronal maturation on soft substrates. Biomaterials. 30 (27):4567-4572.

59. Tortorella I, Argentati C, Emiliani C, Martino S, Morena F. (2021) The role of physical cues in the development of stem cell-derived organoids. European Biophysics Journal.1-13.

60. Cheng H, Huang Y, Chen W, Che J, Liu T, Na J, Wang R, Fan Y. (2021) Cyclic strain and electrical co-stimulation improve neural differentiation of marrow-derived mesenchymal stem cells. Frontiers in cell and developmental biology.903.

61. Rosenbloom AB, Tarczyński M, Lam N, Kane RS, Bugaj LJ, Schaffer DV. (2020) β-Catenin signaling dynamics regulate cell fate in differentiating neural stem cells. Proceedings of the National Academy of Sciences. 117 (46):28828-28837.

62. Higgins S, Lee JS, Ha L, Lim JY. (2013) Inducing neurite outgrowth by mechanical cell stretch. BioResearch Open Access. 2 (3):212-216.

63. De Vincentiis S, Falconieri A, Mainardi M, Cappello V, Scribano V, Bizzarri R, Storti B, Dente L, Costa M, Raffa V. (2020) Extremely low forces induce extreme axon growth. Journal of Neuroscience. 40 (26):4997-5007.

64. Mckee AC, Daneshvar DH. (2015) The neuropathology of traumatic brain injury. Handbook of clinical neurology. 127:45-66.

65. Tong X, Yang F. (2016) Sliding hydrogels with mobile molecular ligands and crosslinks as 3D stem cell niche. Advanced Materials. 28 (33):7257-7263.

66. Edelbrock AN, Clemons TD, Chin SM, Roan JJ, Bruckner EP, Álvarez Z, Edelbrock JF, Wek KS, Stupp SI. (2021) Superstructured Biomaterials Formed by Exchange Dynamics and Host–Guest Interactions in Supramolecular Polymers. Advanced Science. 8 (8):2004042.

67. Peressotti S, Koehl GE, Goding JA, Green RA. (2021) Self-assembling hydrogel structures for neural tissue repair. ACS Biomaterials Science & Engineering. 7 (9):4136-4163.

68. Geddes LA, Baker LE. (1967) The specific resistance of biological material—a compendium of data for the biomedical engineer and physiologist. Medical and biological engineering. 5 (3):271-293.

69. Miklavčič D, Pavšelj N, Hart FX. (2006) Electric properties of tissues. Wiley encyclopedia of biomedical engineering.

70. Cheng H, Huang Y, Yue H, Fan Y. (2021) Electrical stimulation promotes stem cell neural differentiation in tissue engineering. Stem cells international. 2021:1-14.

71. Zhu R, Sun Z, Li C, Ramakrishna S, Chiu K, He L. (2019) Electrical stimulation affects neural stem cell fate and function in vitro. Experimental neurology. 319:112963.

72. Boni R, Ali A, Shavandi A, Clarkson AN. (2018) Current and novel polymeric biomaterials for neural tissue engineering. Journal of biomedical science. 25:1-21.

73. Song S, George PM. (2017) Conductive polymer scaffolds to improve neural recovery. Neural regeneration research. 12 (12):1976.

74. Houreld N, Abrahamse H. (2007) In vitro exposure of wounded diabetic fibroblast cells to a helium-neon laser at 5 and 16 J/cm2. Photomedicine and laser surgery. 25 (2):78-84.

75. Sefton EJB. The Effect of Electrical Stimulation on Endogenous Neural Stem and Progenitor Cell Behavior: University of Toronto (Canada); 2019.

76. Liu G, Li XM, Tian S, Lu RR, Chen Y, Xie HY, Yu KW, Zhang JJ, Wu JF, Zhu YL. (2020) The effect of magnetic stimulation on differentiation of human induced

pluripotent stem cells into neuron. Journal of Cellular Biochemistry. 121 (10):4130-4141.

77. Cui M, Ge H, Zhao H, Zou Y, Chen Y, Feng H. (2017) Electromagnetic fields for the regulation of neural stem cells. Stem cells international. 2017.

78. Sherafat MA, Heibatollahi M, Mongabadi S, Moradi F, Javan M, Ahmadiani A. (2012) Electromagnetic field stimulation potentiates endogenous myelin repair by recruiting subventricular neural stem cells in an experimental model of white matter demyelination. Journal of Molecular Neuroscience. 48 (1):144-153.

79. Cuccurazzu B, Leone L, Podda MV, Piacentini R, Riccardi E, Ripoli C, Azzena GB, Grassi C. (2010) Exposure to extremely low-frequency (50 Hz) electromagnetic fields enhances adult hippocampal neurogenesis in C57BL/6 mice. Experimental neurology. 226 (1):173-182.

80. Arias-Carrion O, Verdugo-Diaz L, Feria-Velasco A, Millán-Aldaco D, Gutierrez A, Hernández-Cruz A, Drucker-Colín R. (2004) Neurogenesis in the subventricular zone following transcranial magnetic field stimulation and nigrostriatal lesions. Journal of neuroscience research. 78 (1):16-28.

81. Chen F-M, Liu X. (2016) Advancing biomaterials of human origin for tissue engineering. Progress in polymer science. 53:86-168.

82. Xing H, Lee H, Luo L, Kyriakides TR. (2020) Extracellular matrix-derived biomaterials in engineering cell function. Biotechnology advances. 42:107421.

83. Doblado LR, Martínez-Ramos C, Pradas MM. (2021) Biomaterials for neural tissue engineering. Frontiers in Nanotechnology. 3:643507.

84. Gregorio I, Braghetta P, Bonaldo P, Cescon M. (2018) Collagen VI in healthy and diseased nervous system. Disease models & mechanisms. 11 (6):dmm032946.

85. Cui Y, Lu C, Meng D, Xiao Z, Hou X, Ding W, Kou D, Yao Y, Chen B, Zhang Z. (2014) Collagen scaffolds modified with CNTF and bFGF promote facial nerve regeneration in minipigs. Biomaterials. 35 (27):7819-7827.

86. Millán D, Jiménez RA, Nieto LE, Poveda IY, Torres MA, Silva AS, Ospina LF, Mano JF, Fontanilla MR. (2021) Adjustable conduits for guided peripheral nerve

regeneration prepared from bi-zonal unidirectional and multidirectional laminar scaffold of type I collagen. Materials Science and Engineering: C. 121:111838.

87. Kim G, Ahn S, Yoon H, Kim Y, Chun W. (2009) A cryogenic direct-plotting system for fabrication of 3D collagen scaffolds for tissue engineering. Journal of Materials Chemistry. 19 (46):8817-8823.

88. Yoo J, Park JH, Kwon YW, Chung JJ, Choi IC, Nam JJ, Lee HS, Jeon EY, Lee K, Kim SH. (2020) Augmented peripheral nerve regeneration through elastic nerve guidance conduits prepared using a porous PLCL membrane with a 3D printed collagen hydrogel. Biomaterials science. 8 (22):6261-6271.

89. Zhang H, Guo J, Wang Y, Shang L, Chai R, Zhao Y. (2022) Natural Polymer-Derived Bioscaffolds for Peripheral Nerve Regeneration. Advanced Functional Materials. 32 (41):2203829.

90. Bupphathong S, Quiroz C, Huang W, Chung P-F, Tao H-Y, Lin C-H. (2022) Gelatin Methacrylate Hydrogel for Tissue Engineering Applications—A Review on Material Modifications. Pharmaceuticals. 15 (2):171.

91. Piao Y, You H, Xu T, Bei H-P, Piwko IZ, Kwan YY, Zhao X. (2021) Biomedical applications of gelatin methacryloyl hydrogels. Engineered Regeneration. 2:47-56.

92. Zhang H, Xu J. (2021) The effects of GelMA hydrogel on nerve repair and regeneration in mice with spinal cord injury. Annals of Translational Medicine. 9 (14).

93. Zhou P, Xu P, Guan J, Zhang C, Chang J, Yang F, Xiao H, Sun H, Zhang Z, Wang M. (2020) Promoting 3D neuronal differentiation in hydrogel for spinal cord regeneration. Colloids and Surfaces B: Biointerfaces. 194:111214.

94. Chen C, Tang J, Gu Y, Liu L, Liu X, Deng L, Martins C, Sarmento B, Cui W, Chen L. (2019) Bioinspired hydrogel electrospun fibers for spinal cord regeneration. Advanced Functional Materials. 29 (4):1806899.

95. Zhou X, Cui H, Nowicki M, Miao S, Lee S-J, Masood F, Harris BT, Zhang LG. (2018) Three-dimensional-bioprinted dopamine-based matrix for promoting neural regeneration. ACS applied materials & interfaces. 10 (10):8993-9001.

96. Dicker KT, Gurski LA, Pradhan-Bhatt S, Witt RL, Farach-Carson MC, Jia X. (2014)

Hyaluronan: a simple polysaccharide with diverse biological functions. Acta biomaterialia. 10 (4):1558-1570.

97. Cui F, Tian W, Hou S, Xu Q, Lee I-S. (2006) Hyaluronic acid hydrogel immobilized with RGD peptides for brain tissue engineering. Journal of Materials Science: Materials in Medicine. 17 (12):1393-1401.

98. Borzacchiello A, Mayol L, Ramires PA, Pastorello A, Di Bartolo C, Ambrosio L, Milella E. (2007) Structural and rheological characterization of hyaluronic acid-based scaffolds for adipose tissue engineering. Biomaterials. 28 (30):4399-4408.

99. Wood MD. Growth factor delivery from fibrin matrics containing affinity-based delivery systems to treat peripheral nerve injury: Washington University in St. Louis; 2009.

100. Rajaram A. 3D bioprinted hydrogel scaffolds laden with Schwann cells for use as nerve repair conduits: University of Saskatchewan; 2015.

101. Vedaraman S, Bernhagen D, Haraszti T, Licht C, Nava AC, Anarkoli AO, Timmerman P, De Laporte L. (2021) Bicyclic RGD peptides enhance nerve growth in synthetic PEG-based Anisogels. Biomaterials Science. 9 (12):4329-4342.

102. Brus J, Urbanova M, Czernek J, Pavelkova M, Kubova K, Vyslouzil J, Abbrent S, Konefal R, Horský J, Vetchy D. (2017) Structure and dynamics of alginate gels cross-linked by polyvalent ions probed via solid state NMR spectroscopy. Biomacromolecules. 18 (8):2478-2488.

103. Song R, Murphy M, Li C, Ting K, Soo C, Zheng Z. (2018) Current development of biodegradable polymeric materials for biomedical applications. Drug design, development and therapy. 12:3117.

104. Madduma-Bandarage US, Madihally SV. (2021) Synthetic hydrogels: Synthesis, novel trends, and applications. Journal of Applied Polymer Science. 138 (19):50376.

105. Dalton PD, Flynn L, Shoichet MS. (2002) Manufacture of poly (2-hydroxyethyl methacrylate-co-methyl methacrylate) hydrogel tubes for use as nerve guidance channels. Biomaterials. 23 (18):3843-3851.

106. Vasile C, Pamfil D, Stoleru E, Baican M. (2020) New developments in medical applications of hybrid hydrogels containing natural polymers. Molecules. 25 (7):1539.

107. Madhusudanan P, Raju G, Shankarappa S. (2020) Hydrogel systems and their role in neural tissue engineering. Journal of the Royal Society Interface. 17 (162):20190505.

108. Lampe KJ, Mooney RG, Bjugstad KB, Mahoney MJ. (2010) Effect of macromer weight percent on neural cell growth in 2D and 3D nondegradable PEG hydrogel culture. Journal of Biomedical Materials Research Part A. 94 (4):1162-1171.

109. Tomczykowa M, Plonska-Brzezinska ME. (2019) Conducting polymers, hydrogels and their composites: Preparation, properties and bioapplications. Polymers. 11 (2):350.

110. Min JH, Patel M, Koh W-G. (2018) Incorporation of conductive materials into hydrogels for tissue engineering applications. Polymers. 10 (10):1078.

111. Wu Y, Chen YX, Yan J, Quinn D, Dong P, Sawyer SW, Soman P. (2016) Fabrication of conductive gelatin methacrylate–polyaniline hydrogels. Acta biomaterialia. 33:122-130.

112. Sun K, Zhang S, Li P, Xia Y, Zhang X, Du D, Isikgor FH, Ouyang J. (2015) Review on application of PEDOTs and PEDOT: PSS in energy conversion and storage devices. Journal of Materials Science: Materials in Electronics. 26 (7):4438-4462.

113. Murjani BO, Kadu PS, Bansod M, Vaidya SS, Yadav MD. (2022) Carbon nanotubes in biomedical applications: current status, promises, and challenges. Carbon Letters.1-20.

114. Accardi MV, Pugsley MK, Forster R, Troncy E, Huang H, Authier S. (2016) The emerging role of in vitro electrophysiological methods in CNS safety pharmacology. Journal of pharmacological and toxicological methods. 81:47-59.

115. Cantley WL, Du C, Lomoio S, DePalma T, Peirent E, Kleinknecht D, Hunter M, Tang-Schomer MD, Tesco G, Kaplan DL. (2018) Functional and sustainable 3D human neural network models from pluripotent stem cells. ACS biomaterials science & engineering. 4 (12):4278-4288.

116.Lee S, Trinh TH, Yoo M, Shin J, Lee H, Kim J, Hwang E, Lim Y-b, Ryou C. (2019) Self-assembling peptides and their application in the treatment of diseases. International journal of molecular sciences. 20 (23):5850.

117.Hong YJ, Do JT. (2019) Neural lineage differentiation from pluripotent stem cells to mimic human brain tissues. Frontiers in Bioengineering and Biotechnology. 7:400.

118.Tong X, Ga L, Zhao R, Ai J. (2021) Research progress on the applications of paper chips. RSC advances. 11 (15):8793-8820.

119.Haring AP, Sontheimer H, Johnson BN. (2017) Microphysiological human brain and neural systems-on-a-chip: potential alternatives to small animal models and emerging platforms for drug discovery and personalized medicine. Stem cell reviews and reports. 13 (3):381-406.

120. Jiang K, Dong C, Xu Y, Wang L. (2016) Microfluidic-based biomimetic models for life science research. RSC advances. 6 (32):26863-26873.

121. Sun H, Jia Y, Dong H, Dong D, Zheng J. (2020) Combining additive manufacturing with microfluidics: an emerging method for developing novel organs-on-chips. Current Opinion in Chemical Engineering. 28:1-9.

122. Staicu CE, Jipa F, Axente E, Radu M, Radu BM, Sima F. (2021) Lab-on-a-Chip Platforms as Tools for Drug Screening in Neuropathologies Associated with Blood–Brain Barrier Alterations. Biomolecules. 11 (6):916.

123. Yin B-S, Li M, Liu B-M, Wang S-Y, Zhang W-G. (2015) An integrated microfluidic device for screening the effective concentration of locally applied tacrolimus for peripheral nerve regeneration. Experimental and therapeutic medicine. 9 (1):154-158.

124. Qiu B, Bessler N, Figler K, Buchholz MB, Rios AC, Malda J, Levato R, Caiazzo M. (2020) Bioprinting neural systems to model central nervous system diseases. Advanced Functional Materials. 30 (44):1910250.

125. Struzyna LA, Katiyar K, Cullen DK. (2014) Living scaffolds for neuroregeneration. Current Opinion in Solid State and Materials Science. 18 (6):308-318.

126. Joung D, Truong V, Neitzke CC, Guo SZ, Walsh PJ, Monat JR, Meng F, Park SH, Dutton JR, Parr AM. (2018) 3D printed stem-cell derived neural progenitors generate spinal cord scaffolds. Advanced Functional Materials. 28 (39):1801850.

127. Ji S, Almeida E, Guvendiren M. (2019) 3D bioprinting of complex channels within cell-laden hydrogels. Acta biomaterialia. 95:214-224.

128. Pagan-Diaz GJ, Ramos-Cruz KP, Sam R, Kandel ME, Aydin O, Saif MTA, Popescu G, Bashir R. (2019) Engineering geometrical 3-dimensional untethered in vitro neural tissue mimic. Proceedings of the National Academy of Sciences. 116 (51):25932-25940.

129. Gu Q, Tomaskovic-Crook E, Lozano R, Chen Y, Kapsa RM, Zhou Q, Wallace GG, Crook JM. (2016) Functional 3D Neural Mini-Tissues From Printed Gel-Based Bioink And Human. Details Gu, Q, Tomaskovic-Crook, E, Lozano, R, Chen, Y, Kapsa, RMI, Zhou, Q, Wallace, GG & Crook, JM (2016) Functional 3D neural mini-tissues from printed gel-based bioink and human neural stem cells Advanced Healthcare Materials, 5 (12), 1429-1438.

130. M Metcalfe S, Bickerton S, Fahmy T. (2017) Neurodegenerative disease: a perspective on cell-based therapy in the new era of cell-free nano-therapy. Current pharmaceutical design. 23 (5):776-783.

131. Du X, Wang X, Geng M. (2018) Alzheimer's disease hypothesis and related therapies. Translational neurodegeneration. 7 (1):1-7.

132. Porsolt RD, Lemaire M, Dürmüller N, Roux S. (2002) New perspectives in CNS safety pharmacology. Fundamental & clinical pharmacology. 16 (3):197-207.

133. Authier S, Paquette D, Gauvin D, Sammut V, Fournier S, Chaurand F, Troncy E. (2009) Video-electroencephalography in conscious non human primate using radiotelemetry and computerized analysis: refinement of a safety pharmacology model. Journal of pharmacological and toxicological methods. 60 (1):88-93.

134. Sirenko O, Parham F, Dea S, Sodhi N, Biesmans S, Mora-Castilla S, Ryan K, Behl M, Chandy G, Crittenden C. (2019) Functional and mechanistic neurotoxicity profiling using human iPSC-derived neural 3D cultures. Toxicological Sciences. 167

(1):58-76.

135. Schmidt CE, Leach JBJArobe. (2003) Neural tissue engineering: strategies for repair and regeneration. 5 (1):293-347.

136. Subramanian A, Krishnan UM, Sethuraman SJJobs. (2009) Development of biomaterial scaffold for nerve tissue engineering: Biomaterial mediated neural regeneration. 16 (1):1-11.

137. Johnson EO, Zoubos AB, Soucacos PNJI. (2005) Regeneration and repair of peripheral nerves. 36 (4):S24-S29.

138. Toyama BH, Savas JN, Park SK, Harris MS, Ingolia NT, Yates III JR, Hetzer MW. (2013) Identification of long-lived proteins reveals exceptional stability of essential cellular structures. Cell. 154 (5):971-982.

139. Keung AJ, Asuri P, Kumar S, Schaffer DV. (2012) Soft microenvironments promote the early neurogenic differentiation but not self-renewal of human pluripotent stem cells. Integrative Biology. 4 (9):1049-1058.

140. Van Essen DC. (1997) A tension-based theory of morphogenesis and compact wiring in the central nervous system. Nature. 385 (6614):313-318.

141. Mothe AJ, Tator CH. (2013) Review of transplantation of neural stem/progenitor cells for spinal cord injury. International Journal of Developmental Neuroscience. 31 (7):701-713.

142. Kojima K, Miyoshi H, Nagoshi N, Kohyama J, Itakura G, Kawabata S, Ozaki M, Iida T, Sugai K, Ito S. (2019) Selective ablation of tumorigenic cells following human induced pluripotent stem cell-derived neural stem/progenitor cell transplantation in spinal cord injury. Stem Cells Translational Medicine. 8 (3):260-270.

143. Thakor J, Ahadian S, Niakan A, Banton E, Nasrollahi F, Hasani-Sadrabadi MM, Khademhosseini A. (2020) Engineered hydrogels for brain tumor culture and therapy. Bio-Design and Manufacturing.1-24.

144. Béduer A, Vieu C, Arnauduc F, Sol J-C, Loubinoux I, Vaysse L. (2012) Engineering of adult human neural stem cells differentiation through surface micropatterning. Biomaterials. 33 (2):504-514.

145. Zhang D, Suo H, Qian J, Yin J, Fu J, Huang Y. (2020) Physical understanding of axonal growth patterns on grooved substrates: groove ridge crossing versus longitudinal alignment. Bio-Design and Manufacturing. 3 (4):348-360.

146. Chen JWE, Pedron S, Harley BA. (2017) The Combined Influence of Hydrogel Stiffness and Matrix-Bound Hyaluronic Acid Content on Glioblastoma Invasion. Macromolecular bioscience. 17 (8):1700018.

147. Heffernan JM, Overstreet DJ, Le LD, Vernon BL, Sirianni RW. (2015) Bioengineered scaffolds for 3D analysis of glioblastoma proliferation and invasion. Annals of Biomedical Engineering. 43 (8):1965-1977.

148. Riehl BD, Park J-H, Kwon IK, Lim JY. (2012) Mechanical stretching for tissue engineering: two-dimensional and three-dimensional constructs. Tissue Engineering Part B: Reviews. 18 (4):288-300.

149. McGlynn E, Nabaei V, Ren E, Galeote-Checa G, Das R, Curia G, Heidari HJAS. (2021) The future of neuroscience: flexible and wireless implantable neural electronics. Advanced Science. 8 (10):2002693.

150. Holtzmann K, Gautier HO, Christ AF, Guck J, Káradóttir RT, Franze KJJoNM. (2016) Brain tissue stiffness is a sensitive marker for acidosis. Journal of Neuroscience Methods. 271:50-54.

151. Jorba I, Menal MJ, Torres M, Gozal D, Piñol-Ripoll G, Colell A, Montserrat JM, Navajas D, Farré R, Almendros IJJotMBoBM. (2017) Ageing and chronic intermittent hypoxia mimicking sleep apnea do not modify local brain tissue stiffness in healthy mice. Journal of the Mechanical Behavior of Biomedical Materials. 71:106-113.

152. Murphy MC, Jones DT, Jack Jr CR, Glaser KJ, Senjem ML, Manduca A, Felmlee JP, Carter RE, Ehman RL, Huston III JJNC. (2016) Regional brain stiffness changes across the Alzheimer's disease spectrum. NeuroImage: Clinical. 10:283-290.

153. Kolipaka A, Wassenaar PA, Cha S, Marashdeh WM, Mo X, Kalra P, Gans B, Raterman B, Bourekas EJCi. (2018) Magnetic resonance elastography to estimate brain stiffness: Measurement reproducibility and its estimate in pseudotumor cerebri patients.

Clinical Imaging. 51:114-122.

154. Arani A, Murphy MC, Glaser KJ, Manduca A, Lake DS, Kruse SA, Jack Jr CR, Ehman RL, Huston 3rd JJN. (2015) Measuring the effects of aging and sex on regional brain stiffness with MR elastography in healthy older adults. Neuroimage. 111:59-64.

155. Handorf AM, Zhou Y, Halanski MA, Li W-J. (2015) Tissue stiffness dictates development, homeostasis, and disease progression. Organogenesis. 11 (1):1-15.

156. Saxena T, Gilbert J, Stelzner D, Hasenwinkel JJJon. (2012) Mechanical characterization of the injured spinal cord after lateral spinal hemisection injury in the rat. Journal of Neurotrauma. 29 (9):1747-1757.

157. Tarun Saxena JLG, Julie M. Hasenwinke. (2009) A versatile mesoindentation system to evaluate the micromechanical properties of soft, hydrated substrates on a cellular scale. Journal of Biomedical Materials Research Part A. 90 (4):1206-1217.

158. Ozawa H, Matsumoto T, Ohashi T, Sato M, Kokubun SJJoNS. (2001) Comparison of spinal cord gray matter and white matter softness: measurement by pipette aspiration method. Journal of Neurosurgery: Spine. 95 (2):221-224.

159. Nachlas AL, Li S, Jha R, Singh M, Xu C, Davis MEJAb. (2018) Human iPSC-derived mesenchymal stem cells encapsulated in PEGDA hydrogels mature into valve interstitial-like cells. Acta Biomaterialia. 71:235-246.

160. Weber LM, He J, Bradley B, Haskins K, Anseth KSJAb. (2006) PEG-based hydrogels as an in vitro encapsulation platform for testing controlled β-cell microenvironments. Acta Biomaterialia. 2 (1):1-8.

161. Han WT, Jang T, Chen S, Chong LSH, Jung H-D, Song J. (2020) Improved cell viability for large-scale biofabrication with photo-crosslinkable hydrogel systems through a dual-photoinitiator approach. Biomaterials science. 8 (1):450-461. 10.1039/C9BM01347D

162. Ying J, Han Z, Zeng Y, Du Y, Pei S, Su L, Ruan D, Chen CJAjotr. (2019) Evaluation of intervertebral disc regeneration with injection of mesenchymal stem cells encapsulated in PEGDA-microcryogel delivery system using quantitative T2 mapping: a study in canines. American Journal of Translational Research. 11 (4):2028.

163. Xiao S, Zhao T, Wang J, Wang C, Du J, Ying L, Lin J, Zhang C, Hu W, Wang LJScr, reports. (2019) Gelatin methacrylate (GelMA)-based hydrogels for cell transplantation: an effective strategy for tissue engineering. Stem Cell Reviews and Reports. 15 (5):664-679.

164. Zhao X, Liu S, Yildirimer L, Zhao H, Ding R, Wang H, Cui W, Weitz D. (2016) Injectable stem cell-laden photocrosslinkable microspheres fabricated using microfluidics for rapid generation of osteogenic tissue constructs. Advanced Functional Materials. 26 (17):2809-2819.

165. Koffler J, Zhu W, Qu X, Platoshyn O, Dulin JN, Brock J, Graham L, Lu P, Sakamoto J, Marsala MJNm. (2019) Biomimetic 3D-printed scaffolds for spinal cord injury repair. Nature Medicine. 25 (2):263-269.

166. Zhang X, Xu B, Puperi DS, Yonezawa AL, Wu Y, Tseng H, Cuchiara ML, West JL, Grande-Allen KJJAb. (2015) Integrating valve-inspired design features into poly (ethylene glycol) hydrogel scaffolds for heart valve tissue engineering. Acta Biomaterialia. 14:11-21.

167. Wang Y, Cao X, Ma M, Lu W, Zhang B, Guo YJM. (2020) A GelMA-PEGDA-nHA composite hydrogel for bone tissue engineering. Materials. 13 (17):3735.

168. Skaalure SC, Chu S, Bryant SJJAhm. (2015) An enzyme-sensitive PEG hydrogel based on aggrecan catabolism for cartilage tissue engineering. Advanced Healthcare Materials. 4 (3):420-431.

169. Sun M, Sun X, Wang Z, Guo S, Yu G, Yang H. (2018) Synthesis and properties of gelatin methacryloyl (GelMA) hydrogels and their recent applications in load-bearing tissue. Polymers. 10 (11):1290.

170. Zhao X, Lang Q, Yildirimer L, Lin ZY, Cui W, Annabi N, Ng KW, Dokmeci MR, Ghaemmaghami AM, Khademhosseini A. (2016) Photocrosslinkable gelatin hydrogel for epidermal tissue engineering. Advanced Healthcare Materials. 5 (1):108-118.

171. Son KH, Lee JWJM. (2016) Synthesis and characterization of poly (ethylene glycol) based thermo-responsive hydrogels for cell sheet engineering. Materials. 9

(10):854.

172. Zhang L, Zhao J, Zhu J, He C, Wang H. (2012) Anisotropic tough poly (vinyl alcohol) hydrogels. Soft Matter. 8 (40):10439-10447. 10.1039/C2SM26102B

173. Gan D, Huang Z, Wang X, Jiang L, Wang C, Zhu M, Ren F, Fang L, Wang K, Xie C. (2020) Graphene oxide-templated conductive and redox-active nanosheets incorporated hydrogels for adhesive bioelectronics. Advanced Functional Materials. 30 (5):1907678.

174. Zhu M, Wang Y, Ferracci G, Zheng J, Cho N-J, Lee BH. (2019) Gelatin methacryloyl and its hydrogels with an exceptional degree of controllability and batch-to-batch consistency. Scientific reports. 9 (1):1-13.

175. Park J, Jeon J, Kim B, Lee MS, Park S, Lim J, Yi J, Lee H, Yang HS, Lee JY. (2020) Electrically conductive hydrogel nerve guidance conduits for peripheral nerve regeneration. Advanced Functional Materials. 30 (39):2003759.

176. Tremblay RG, Sikorska M, Sandhu JK, Lanthier P, Ribecco-Lutkiewicz M, Bani-Yaghoub M. (2010) Differentiation of mouse Neuro 2A cells into dopamine neurons. Journal of Neuroscience Methods. 186 (1):60-67.

177. Pemberton K, Mersman B, Xu F. (2018) Using ImageJ to assess neurite outgrowth in mammalian cell cultures: research data quantification exercises in undergraduate neuroscience lab. Journal of Undergraduate Neuroscience Education. 16 (2):A186.

178. Yang Y, Xu T, Zhang Q, Piao Y, Bei HP, Zhao X. (2021) Biomimetic, Stiff, and Adhesive Periosteum with Osteogenic–Angiogenic Coupling Effect for Bone Regeneration. Small. 17 (14):2006598.

179. Li W, Fan X, Wang Y, Wang J, Li M, Li X, Tang K, Wan G. (2020) A glycidyl methacrylate modified collagen/polyethylene glycol diacrylate hydrogel: a mechanically strong hydrogel for loading levofloxacin. New Journal of Chemistry. 44 (39):17027-17032.

180. Imani M, Sharifi S, Mirzadeh H, Ziaei F. (2007) Monitoring of polyethylene glycoldiacrylate-based hydrogel formation by real time NMR spectroscopy. Iranian

Polymer Journal. 16 (1):14-20.

181. Della Sala F, Biondi M, Guarnieri D, Borzacchiello A, Ambrosio L, Mayol L. (2020) Mechanical behavior of bioactive poly (ethylene glycol) diacrylate matrices for biomedical application. Journal of the Mechanical Behavior of Biomedical Materials. 110:103885.

182. Temenoff JS, Athanasiou KA, Lebaron RG, Mikos AG. (2002) Effect of poly (ethylene glycol) molecular weight on tensile and swelling properties of oligo (poly (ethylene glycol) fumarate) hydrogels for cartilage tissue engineering. Journal of Biomedical Materials Research. 59 (3):429-437.

183. Sun H, Haque FM, Zhang Y, Commisso A, Mohamed MA, Tsianou M, Cui H, Grayson SM, Cheng C. (2019) Linear-Dendritic Alternating Copolymers. Angewandte Chemie. 131 (31):10682-10686.

184. Abramowitch S, Easley D. Introduction to classical mechanics. Biomechanics of the female pelvic floor: Elsevier; 2016. p. 89-107.

185. Cantini M, Donnelly H, Dalby MJ, Salmeron-Sanchez M. (2020) The plot thickens: the emerging role of matrix viscosity in cell mechanotransduction. Advanced Healthcare Materials. 9 (8):1901259.

186. Murrell M, Kamm R, Matsudaira P. (2011) Substrate viscosity enhances correlation in epithelial sheet movement. Biophysical journal. 101 (2):297-306. 10.1016/j.bpj.2011.05.048

187. Fernández-Pérez J, Ahearne M. (2019) The impact of decellularization methods on extracellular matrix derived hydrogels. Scientific reports. 9 (1):1-12. 10.1016/j.actbio.2018.02.025

188. Stillman Z, Jarai BM, Raman N, Patel P, Fromen CA. (2020) Degradation profiles of poly (ethylene glycol) diacrylate (PEGDA)-based hydrogel nanoparticles. Polymer Chemistry. 11 (2):568-580. 10.1039/C9PY01206K

189. Browning M, Cereceres S, Luong P, Cosgriff-Hernandez E. (2014) Determination of the in vivo degradation mechanism of PEGDA hydrogels. Journal of Biomedical Materials Research Part A. 102 (12):4244-4251. 10.1002/jbm.a.35096

190. Jia J, Coyle RC, Richards DJ, Berry CL, Barrs RW, Biggs J, Chou CJ, Trusk TC, Mei YJAb. (2016) Development of peptide-functionalized synthetic hydrogel microarrays for stem cell and tissue engineering applications. Acta Biomaterialia. 45:110-120.

191. Oyarce K, Silva-Alvarez C, Ferrada L, Martínez F, Salazar K, Nualart F. (2018) SVCT2 is expressed by cerebellar precursor cells, which differentiate into neurons in response to ascorbic acid. Molecular Neurobiology. 55 (2):1136-1149.

192. Jin J, Tilve S, Huang Z, Zhou L, Geller HM, Yu P. (2018) Effect of chondroitin sulfate proteoglycans on neuronal cell adhesion, spreading and neurite growth in culture. Neural regeneration research. 13 (2):289.

193. Hsieh F-Y, Tseng T-C, Hsu S-hJNrr. (2015) Self-healing hydrogel for tissue repair in the central nervous system. Neural Regeneration Research. 10 (12):1922. DOI: 10.4103/1673-5374.169624

194. Banerjee A, Arha M, Choudhary S, Ashton RS, Bhatia SR, Schaffer DV, Kane RSJB. (2009) The influence of hydrogel modulus on the proliferation and differentiation of encapsulated neural stem cells. Biomaterials. 30 (27):4695-4699.

195. Zhu Y, Li X, Janairo RRR, Kwong G, Tsou AD, Chu JS, Wang A, Yu J, Wang D, Li S. (2019) Matrix stiffness modulates the differentiation of neural crest stem cells in vivo. Journal of Cellular Physiology. 234 (5):7569-7578.

196. Tseng TC, Tao L, Hsieh FY, Wei Y, Chiu IM, Hsu Sh. (2015) An injectable, self-healing hydrogel to repair the central nervous system. Advanced Materials. 27 (23):3518-3524.

197. Stukel JM, Willits RK. (2018) The interplay of peptide affinity and scaffold stiffness on neuronal differentiation of neural stem cells. Biomedical Materials. 13 (2):024102. 10.1088/1748-605X/aa9a4b

198. Wu S, Xu R, Duan B, Jiang P. (2017) Three-dimensional hyaluronic acid hydrogel-based models for in vitro human iPSC-derived NPC culture and differentiation. Journal of Materials Chemistry B. 5 (21):3870-3878.

199. Park SY, Park J, Sim SH, Sung MG, Kim KS, Hong BH, Hong S. (2011)

Enhanced differentiation of human neural stem cells into neurons on graphene. Advanced materials. 23 (36):H263-H267.

200. Pires F, Ferreira Q, Rodrigues CA, Morgado J, Ferreira FC. (2015) Neural stem cell differentiation by electrical stimulation using a cross-linked PEDOT substrate: Expanding the use of biocompatible conjugated conductive polymers for neural tissue engineering. Biochimica et Biophysica Acta (BBA)-General Subjects. 1850 (6):1158-1168.

201. Schmidt CE, Shastri VR, Vacanti JP, Langer R. (1997) Stimulation of neurite outgrowth using an electrically conducting polymer. Proceedings of the National Academy of Sciences. 94 (17):8948-8953.

202. Tian L, Prabhakaran MP, Ramakrishna S. (2015) Strategies for regeneration of components of nervous system: scaffolds, cells and biomolecules. Regenerative biomaterials. 2 (1):31-45.

203. Xu X, Wang L, Jing J, Zhan J, Xu C, Xie W, Ye S, Zhao Y, Zhang C, Huang F. (2022) Conductive Collagen-Based Hydrogel Combined With Electrical Stimulation to Promote Neural Stem Cell Proliferation and Differentiation. Frontiers in bioengineering and biotechnology. 10.

204. Distler T, Boccaccini AR. (2020) 3D printing of electrically conductive hydrogels for tissue engineering and biosensors–A review. Acta biomaterialia. 101:1-13.

205. Jakus AE, Secor EB, Rutz AL, Jordan SW, Hersam MC, Shah RN. (2015) Three-dimensional printing of high-content graphene scaffolds for electronic and biomedical applications. ACS nano. 9 (4):4636-4648.

206. Balint R, Cassidy NJ, Cartmell SH. (2014) Conductive polymers: Towards a smart biomaterial for tissue engineering. Acta biomaterialia. 10 (6):2341-2353.

207. Heo DN, Acquah N, Kim J, Lee S-J, Castro NJ, Zhang LG. (2018) Directly induced neural differentiation of human adipose-derived stem cells using three-dimensional culture system of conductive microwell with electrical stimulation. Tissue Engineering Part A. 24 (7-8):537-545.

208. Kayser LV, Lipomi DJ. (2019) Stretchable conductive polymers and composites based on PEDOT and PEDOT: PSS. Advanced Materials. 31 (10):1806133.

209. Heo DN, Lee S-J, Timsina R, Qiu X, Castro NJ, Zhang LG. (2019) Development of 3D printable conductive hydrogel with crystallized PEDOT: PSS for neural tissue engineering. Materials Science and Engineering: C. 99:582-590.

210. Israel MA, Yuan SH, Bardy C, Reyna SM, Mu Y, Herrera C, Hefferan MP, Van Gorp S, Nazor KL, Boscolo FS. (2012) Probing sporadic and familial Alzheimer's disease using induced pluripotent stem cells. Nature. 482 (7384):216-220.

211. Wang Z, An G, Zhu Y, Liu X, Chen Y, Wu H, Wang Y, Shi X, Mao CJMh. (2019) 3D-printable self-healing and mechanically reinforced hydrogels with host–guest non-covalent interactions integrated into covalently linked networks. 6 (4):733-742.

212. Liu X, Miller II AL, Park S, Waletzki BE, Terzic A, Yaszemski MJ, Lu L. (2016) Covalent crosslinking of graphene oxide and carbon nanotube into hydrogels enhances nerve cell responses. Journal of Materials Chemistry B. 4 (43):6930-6941.

213. Babaie A, Bakhshandeh B, Abedi A, Mohammadnejad J, Shabani I, Ardeshirylajimi A, Moosavi SR, Amini J, Tayebi L. (2020) Synergistic effects of conductive PVA/PEDOT electrospun scaffolds and electrical stimulation for more effective neural tissue engineering. European Polymer Journal. 140:110051.

214. Lee JM, Moon JY, Kim TH, Lee SW, Ahrberg CD, Chung BG. (2018) Conductive hydrogel/nanowire micropattern-based sensor for neural stem cell differentiation. Sensors and Actuators B: Chemical. 258:1042-1050.

215. Lee J, Jr., Ng HY, Lin Y-H, Liu E-W, Lin T-J, Chiu H-T, Ho X-R, Yang H-A, Shie M-Y. (2022) The 3D printed conductive grooved topography hydrogel combined with electrical stimulation for synergistically enhancing wound healing of dermal fibroblast cells. Biomaterials Advances. 142:213132.

216. Bansal M, Vyas Y, Aqrawe Z, Raos B, Cheah E, Montgomery J, Wu Z, Svirskis D. (2022) Patternable Gelatin Methacrylate/PEDOT/Polystyrene Sulfonate Microelectrode Coatings for Neuronal Recording. ACS Biomaterials Science & Engineering. 8 (9):3933-3943. 10.1021/acsbiomaterials.2c00231

217. Alemu D, Wei H-Y, Ho K-C, Chu C-W. (2012) Highly conductive PEDOT:PSS electrode by simple film treatment with methanol for ITO-free polymer solar cells. Energy & Environmental Science. 5 (11). 10.1039/c2ee22595f

218. Wang Y, Pang F-F, Liu D-D, Han G-Z. (2017) In situ synthesis of PEDOT:PSS@AgNPs nanocomposites. Synthetic Metals. 230:1-6. 10.1016/j.synthmet.2017.05.011

219. Abedi A, Hasanzadeh M, Tayebi L. (2019) Conductive nanofibrous Chitosan/PEDOT: PSS tissue engineering scaffolds. Materials Chemistry and Physics. 237:121882.

220. Wang S, Guan S, Xu J, Li W, Ge D, Sun C, Liu T, Ma X. (2017) Neural stem cell proliferation and differentiation in the conductive PEDOT-HA/Cs/Gel scaffold for neural tissue engineering. Biomaterials science. 5 (10):2024-2034.

221. Kim N, Kee S, Lee SH, Lee BH, Kahng YH, Jo YR, Kim BJ, Lee K. (2014) Highly conductive PEDOT: PSS nanofibrils induced by solution-processed crystallization. Advanced materials. 26 (14):2268-2272.

222. West CL, Doughty AC, Liu K, Chen WR. (2019) Monitoring tissue temperature during photothermal therapy for cancer. Journal of bio-X research. 2 (04):159-168.

223. Thrivikraman G, Madras G, Basu B. (2016) Electrically driven intracellular and extracellular nanomanipulators evoke neurogenic/cardiomyogenic differentiation in human mesenchymal stem cells. Biomaterials. 77:26-43.

224. Kotwal A, Schmidt CE. (2001) Electrical stimulation alters protein adsorption and nerve cell interactions with electrically conducting biomaterials. Biomaterials. 22 (10):1055-1064.

225. Patel N, Poo M-M. (1982) Orientation of neurite growth by extracellular electric fields. Journal of Neuroscience. 2 (4):483-496.

226. Yamada M, Tanemura K, Okada S, Iwanami A, Nakamura M, Mizuno H, Ozawa M, Ohyama-Goto R, Kitamura N, Kawano M. (2007) Electrical stimulation modulates fate determination of differentiating embryonic stem cells. Stem cells. 25

(3):562-570.

227. Li X, Kolega J. (2002) Effects of direct current electric fields on cell migration and actin filament distribution in bovine vascular endothelial cells. Journal of vascular research. 39 (5):391-404.

228. Bertrand SJ, Aksenova MV, Aksenov MY, Mactutus CF, Booze RM. (2011) Endogenous amyloidogenesis in long-term rat hippocampal cell cultures. BMC neuroscience. 12 (1):1-11.

229. Feng ZQ, Franz EW, Leach MK, Winterroth F, White CM, Rastogi A, Gu ZZ, Corey JM. (2016) Mechanical tension applied to substrate films specifies location of neuritogenesis and promotes major neurite growth at the expense of minor neurite development. Journal of Biomedical Materials Research Part A. 104 (4):966-974.

230. Tai Y, Ico G, Low K, Liu J, Jariwala T, Garcia-Viramontes D, Lee KH, Myung NV, Park BH, Nam J. (2021) Formation of 3D Self-Organized Neuron-Glial Interface Derived from Neural Stem Cells via Mechano-Electrical Stimulation. Advanced Healthcare Materials. 10 (19):2100806.

231. Song Y, Su X, Firouzian KF, Fang Y, Zhang T, Sun W. (2020) Engineering of brain-like tissue constructs via 3D Cell-printing technology. Biofabrication. 12 (3):035016.

232. Antic SD, Zhou WL, Moore AR, Short SM, Ikonomu KD. (2010) The decade of the dendritic NMDA spike. Journal of neuroscience research. 88 (14):2991-3001.

233. Sukiban J, Voges N, Dembek TA, Pauli R, Visser-Vandewalle V, Denker M, Weber I, Timmermann L, Grün S. (2019) Evaluation of spike sorting algorithms: Application to human subthalamic nucleus recordings and simulations. Neuroscience. 414:168-185.

234. Chuang J-H, Tung L-C, Lin Y. (2015) Neural differentiation from embryonic stem cells in vitro: An overview of the signaling pathways. World Journal of Stem Cells. 7 (2):437.

235. Kampanis V, Tolou-Dabbaghian B, Zhou L, Roth W, Puttagunta R. (2020) Cyclic stretch of either PNS or CNS located nerves can stimulate neurite outgrowth.

Cells. 10 (1):32.

236. Kaunas R, Nguyen P, Usami S, Chien S. (2005) Cooperative effects of Rho and mechanical stretch on stress fiber organization. Proceedings of the National Academy of Sciences. 102 (44):15895-15900.

237. Collaborators GBDN. (2019) Global, regional, and national burden of neurological disorders, 1990-2016: a systematic analysis for the Global Burden of Disease Study 2016. Lancet Neurol. 18 (5):459-480. 10.1016/S1474-4422(18)30499-X

238. McGonigle P, Ruggeri B. (2014) Animal models of human disease: challenges in enabling translation. Biochem Pharmacol. 87 (1):162-171. 10.1016/j.bcp.2013.08.006

239. Yang B, Wei K, Loebel C, Zhang K, Feng Q, Li R, Wong SHD, Xu X, Lau C, Chen X. (2021) Enhanced mechanosensing of cells in synthetic 3D matrix with controlled biophysical dynamics. Nature Communications. 12 (1):1-13.

240. Feng Q, Ma X, Deng Y, Zhang K, Ooi HS, Yang B, Zhang Z-Y, Feng B, Bian L. (2022) Dynamic gelatin-based hydrogels promote the proliferation and self-renewal of embryonic stem cells in long-term 3D culture. Biomaterials. 289:121802.

241. Rodeberg NT, Sandberg SG, Johnson JA, Phillips PE, Wightman RM. (2017) Hitchhiker's guide to voltammetry: acute and chronic electrodes for in vivo fast-scan cyclic voltammetry. ACS chemical neuroscience. 8 (2):221-234.

242. Jain P, Kathuria H, Dubey N. (2022) Advances in 3D bioprinting of tissues/organs for regenerative medicine and in-vitro models. Biomaterials. 287:121639.

243. Malda J, Visser J, Melchels FP, Jüngst T, Hennink WE, Dhert WJ, Groll J, Hutmacher DW. (2013) 25th anniversary article: engineering hydrogels for biofabrication. Advanced materials. 25 (36):5011-5028.

244. Mao H, Yang L, Zhu H, Wu L, Ji P, Yang J, Gu Z. (2020) Recent advances and challenges in materials for 3D bioprinting. Progress in Natural Science: Materials International. 30 (5):618-634.

245. Cadena M, Ning L, King A, Hwang B, Jin L, Serpooshan V, Sloan SA. (2021)

3D bioprinting of neural tissues. Advanced healthcare materials. 10 (15):2001600.

246. Shim J-H, Kim JY, Park M, Park J, Cho D-W. (2011) Development of a hybrid scaffold with synthetic biomaterials and hydrogel using solid freeform fabrication technology. Biofabrication. 3 (3):034102.

247. Fedorovich NE, Alblas J, de Wijn JR, Hennink WE, Verbout AJ, Dhert WJ. (2007) Hydrogels as extracellular matrices for skeletal tissue engineering: state-of-the-art and novel application in organ printing. Tissue engineering. 13 (8):1905-1925.

248. Collins MN, Birkinshaw CJCp. (2013) Hyaluronic acid based scaffolds for tissue engineering—A review. 92 (2):1262-1279.

249. Sherman L, Sleeman J, Herrlich P, Ponta HJCoicb. (1994) Hyaluronate receptors: key players in growth, differentiation, migration and tumor progression. 6 (5):726-733.

250. Wang KK, Nemeth IR, Seckel BR, Chakalis-Haley DP, Swann DA, Kuo JW, Bryan DJ, Cetrulo Jr CLJM. (1998) Hyaluronic acid enhances peripheral nerve regeneration in vivo. 18 (4):270-275.

251. Lai J-Y, Li Y-TJB. (2010) Functional assessment of cross-linked porous gelatin hydrogels for bioengineered cell sheet carriers. 11 (5):1387-1397.

252. Liu Y, Chan-Park MBJB. (2010) A biomimetic hydrogel based on methacrylated dextran-graft-lysine and gelatin for 3D smooth muscle cell culture. 31 (6):1158-1170.

253. Kesti M, Müller M, Becher J, Schnabelrauch M, D'Este M, Eglin D, Zenobi-Wong M. (2015) A versatile bioink for three-dimensional printing of cellular scaffolds based on thermally and photo-triggered tandem gelation. Acta biomaterialia. 11:162-172.

254. Highley CB, Rodell CB, Burdick JA. (2015) Direct 3D printing of shear-thinning hydrogels into self-healing hydrogels. Advanced Materials. 27 (34):5075-5079.

255. Rekharsky MV, Inoue Y. (1998) Complexation thermodynamics of cyclodextrins. Chemical reviews. 98 (5):1875-1918.

256. Lu HD, Soranno DE, Rodell CB, Kim IL, Burdick JA. (2013) Secondary

photocrosslinking of injectable shear-thinning dock-and-lock hydrogels. Advanced healthcare materials. 2 (7):1028-1036.

257. Rodell CB, MacArthur JW, Dorsey SM, Wade RJ, Wang LL, Woo YJ, Burdick JA. (2015) Shear-Thinning Supramolecular Hydrogels with Secondary Autonomous Covalent Crosslinking to Modulate Viscoelastic Properties In Vivo. Adv Funct Mater. 25 (4):636-644. 10.1002/adfm.201403550

258. Yang Y, Zhang YM, Chen Y, Chen JT, Liu Y. (2013) Targeted polysaccharide nanoparticle for adamplatin prodrug delivery. J Med Chem. 56 (23):9725-9736. 10.1021/jm4014168

259. Lee JB, Kim JE, Balikov DA, Bae MS, Heo DN, Lee D, Rim HJ, Lee DW, Sung HJ, Kwon IK. (2016) Poly(l-Lactic Acid)/Gelatin Fibrous Scaffold Loaded with Simvastatin/Beta-Cyclodextrin-Modified Hydroxyapatite Inclusion Complex for Bone Tissue Regeneration. Macromol Biosci. 16 (7):1027-1038. 10.1002/mabi.201500450

260. Nguyen Thi TT, Tran TV, Tran NQ, Nguyen CK, Nguyen DH. (2017) Hierarchical self-assembly of heparin-PEG end-capped porous silica as a redox sensitive nanocarrier for doxorubicin delivery. Mater Sci Eng C Mater Biol Appl. 70 (Pt 2):947-954. 10.1016/j.msec.2016.04.085

261. Hu X, Zhou J, Zhang N, Tan H, Gao C. Preparation and properties of an injectable scaffold of poly(lactic-co-glycolic acid) microparticles/chitosan hydrogel. 1 (4):352-359.

262. Mei Q, Yuen H-Y, Zhao X. (2022) Mechanical stretching of 3D hydrogels for neural stem cell differentiation. Bio-Design and Manufacturing. 5 (4):714-728.

263. Teng KK, Angelastro JM, Cunningham ME, Greene LA. Cultured PC12 cells: a model for neuronal function, differentiation, and survival. Cell biology: Elsevier; 2006. p. 171-176.

264. Li K, Kang S. The image stabilizer plugin for ImageJ. 2008.

265. Koldenkova VP, Nagai T. (2013) Genetically encoded Ca2+ indicators: Properties and evaluation. Biochimica et Biophysica Acta (BBA)-Molecular Cell Research. 1833 (7):1787-1797.

266. Ouzounov DG, Wang T, Wang M, Feng DD, Horton NG, Cruz-Hernández JC, Cheng Y-T, Reimer J, Tolias AS, Nishimura N. (2017) In vivo three-photon imaging of activity of GCaMP6-labeled neurons deep in intact mouse brain. Nature methods. 14 (4):388-390.

267. Fang Y, Wang C-F, Zhang Z-H, Shao H, Chen S. (2013) Robust self-healing hydrogels assisted by cross-linked nanofiber networks. Scientific reports. 3 (1):1-7.

268. Li G, Wu J, Wang B, Yan S, Zhang K, Ding J, Yin J. (2015) Self-healing supramolecular self-assembled hydrogels based on poly (L-glutamic acid). Biomacromolecules. 16 (11):3508-3518.

269. Burdick JA, Chung C, Jia X, Randolph MA, Langer R. (2005) Controlled degradation and mechanical behavior of photopolymerized hyaluronic acid networks. Biomacromolecules. 6 (1):386-391.

270. Camci-Unal G, Cuttica D, Annabi N, Demarchi D, Khademhosseini A. (2013) Synthesis and characterization of hybrid hyaluronic acid-gelatin hydrogels. Biomacromolecules. 14 (4):1085-1092.

271. Lozano R, Stevens L, Thompson BC, Gilmore KJ, Gorkin III R, Stewart EM, in het Panhuis M, Romero-Ortega M, Wallace GG. (2015) 3D printing of layered brain-like structures using peptide modified gellan gum substrates. Biomaterials. 67:264-273.

272. Kong Y, Xu J, Guan W, Sun S, Yang Y, Li G. (2022) Tailoring the elasticity of nerve implants for regulating peripheral nerve regeneration. Smart Materials in Medicine.

273. Ouyang L. Study on microextrusion-based 3D bioprinting and bioink crosslinking mechanisms: Springer; 2019.